University of Dundee

DOCTOR OF PHILOSOPHY

Micro-motion detection by optical coherence tomography (OCT) and its clinical applications

Guan, Guangying

Award date:
2015

Link to publication

General rights
Copyright and moral rights for the publications made accessible in the public portal are retained by the authors and/or other copyright owners and it is a condition of accessing publications that users recognise and abide by the legal requirements associated with these rights.

- Users may download and print one copy of any publication from the public portal for the purpose of private study or research.
- You may not further distribute the material or use it for any profit-making activity or commercial gain
- You may freely distribute the URL identifying the publication in the public portal

Take down policy
If you believe that this document breaches copyright please contact us providing details, and we will remove access to the work immediately and investigate your claim.

Download date: 22. Jan. 2021

Micro-motion detection by optical coherence tomography (OCT) and its clinical applications

Mr Guangying Guan

BSc (Hons) MSc

School of Engineering, Physics and Mathematics

College of Art, Science and Engineering

University of Dundee,

Dundee,

Scotland.

Abstract

Ddetection of micro-motion on biological tissues has various applications such as ultrasound elastography and magnetic resonance elastography (MRE). Ultrasound transducers, the most commonly used tool to detect endogenous and exogenous micro-motions, have a number of drawbacks: including the requirements of the physical contact with the sample and limited spatial resolution (millimetre scale). The aim of this thesis is to develop a non-contact phase-sensitive imaging technique which is suitable for functional imaging in the micron range which also has the potential for quantitative analysis of relative properties resulting from an appropriate image processing.

Concerning imaging techniques, this thesis focused on optical coherence tomography (OCT) and in particular on phase-sensitive optical coherence tomography (PhS-OCT). In this thesis, a PhS-OCT system is developed for micro-motion detection and a dual camera PhS-OCT system is developed to double the imaging acquiring speed and improve the sensitivity to small phase change. Two applications of PhS-OCT combining micro-motions detection are preformed: 1) Photo-thermal OCT (PT-OCT) system is developed to detect the photo-thermal phenomenon of nanoparticles. A mathematic model is proposed to analyse and reconstruct the distribution of nanoparticles in biological tissues. 2) A quantitative 3D optical coherence elastography (OCE) system and algorithm are developed to analysis the mechanical property of tissue. A feasibility study is carried for the diagnosis of prostate cancer (PCa) using this technique.

Results show that PhS-OCT is a powerful tool for the detection of micro-motions (micron range). Functional OCT based on it such as PT-OCT and OCE offers potential in diagnostic and therapeutic in clinical applications, e.g. PT-OCT can be used to detect and map the distribution and concentration of dye and drug in tissues or organs. 3D OCE can provide useful information for early localization and diagnosis of cancer.

Declaration

I hereby declare that this thesis is my own work and effort and that it has not been submitted anywhere for any award. Where other sources of information have been used, they have been acknowledged.

…………………………..

Guangying Guan

Certificate

This is to certify that Guangying Guan has done this research under my supervision and that he has fulfilled the conditions of Ordinance 39 of the University of Dundee, so that he is qualified to submit for the Degree of Doctor of Philosophy.

…………..……………

Dr. Zhihong Huang

Copyright

Attention is drawn to the fact that copyright of this thesis rests with its author. This copy of the thesis has been supplied on the condition that anyone who consults it is understood to recognise that its copyright rests with the author and that no quotation from this thesis and no information derived from it may be published, without prior writhe consent of the author.

This thesis may not be consulted, photocopies or lent by any library without permission of the author for a period of three years from the date of acceptance of the thesis.

Acknowledgements

This is a great opportunity to express my respect to everybody who contributed to this dissertation. I would like to show my special appreciation and thanks to my advisor, Dr Zhihong Huang, for giving me the opportunity to involve into such an exciting project and the chance to work in the laboratory with leading facilities. I would like to thank you for encouraging my research and for allowing me to grow as a research scientist. Your advice on both research as well as on my career have been priceless. I would also like to thank Prof. Ruikang K. Wang, Dr Robert Keatch, for your support, guidance, and mentoring through every step of this work. All of my advisers lighted up the way of conducting research for me, especially from their expertise in both engineering and medicine.

I am pleased to thank the workmates in both of the laboratories in University of Dundee and University of Washington. Prof. Yi Wang, Dr Yumin Liu, Dr Jia Qin, Dr Lin An, Dr Zhongwei Zhi, Dr Guozhong Liu, Dr Xusheng Zhang, Dr Yeongri Jung, Dr Suzan Dziennis and Dr Roberto Reif from University of Washington Bio-photonics and Imaging Laboratory as a great collaborators, who went through many studies with me and shared their wealth of knowledge. I also thank Mr Shaozhen Song and Mrs Yuting Ling in Optical lab in University of Dundee. They have been great team members and friends

Last and most, a special thanks to my family. Words cannot express how grateful I am to my mother-in law, father-in-law, my mother, and father for all of the sacrifices that you've made on my behalf. Your prayer for me was what sustained me thus far. I would also like to thank all of my friends who supported me in writing, and incented me to strive towards my goal. At the end I would like express appreciation to my cute son Chikun Shangguan and my beloved wife Dr Chunhui Li, who spent sleepless nights with and was always my support in the moments when there was no one to answer my queries.

Table of Contents

Abstract I

Declaration II

Certificate III

Copyright IV

Acknowledgements V

Last and most V

Table of Contents VI

List of Figures X

List of Tables XVI

List of Abbreviations and Symbols XVII

Chapter 1 Introduction 1

1.1 Motivation and research objectives 2

1.2 Outline of Thesis 3

1.3 List of publications 5

Chapter 2 Optical coherence tomography: an overview 8

2.1 Introduction 9

2.2 Techniques used for tissue imaging and motion detection 9

2.2.1Ultrasound imaging and elastography 9

2.2.2 Magnetic resonance imaging (MRI) 12

2.3 Basic Theory of Optical Coherence Tomography in biomedicine 14

2.3.1 Time-domain OCT 15

2.3.2 Fourier-domain OCT 19

2.3.3 Applications of OCT 22

2.4 Important parameters of OCT imaging 24

2.4.1 Resolutions 24
2.4.2 Imaging depth 25
2.4.3 Imaging speed 26
2.4.4 Sensitivity 26
2.4.5 Artefacts and noises 28
2.5 Functional OCT imaging systems and applications 29
2.5.1 Polarization sensitive OCT (PS-OCT) 30
2.5.2 Spectroscopic OCT 31
2.5.3 Doppler OCT 33
2.6 Conclusion 34
Chapter 3 Phase sensitive OCT (PhS-OCT) and dual camera system: principles and development 36
3.1 Introduction 37
3.2 The development of Doppler optical coherence tomography (DOCT) 37
3.2.1 Traditional Doppler OCT 37
3.2.2 Phase-Resolved Doppler OCT (PRDOCT) 40
3.2.3 Phase sensitive OCT (PhS-OCT) 42
3.2.4 Comparison between the DOCT technologies 44
3.3 Development of Single camera PhS-OCT system 45
3.3.1 Background 45
3.3.2 Light source 46
3.3.3 High-speed spectrometer 48
3.3.4 System design 52
3.4 Dual camera PhS-OCT system development 53
3.4.1 System evaluation 55
3.5 Conclusion 62
Chapter 4 Photothermal OCT 63

4.1 Introduction 64

4.2 Background of photothermal (PT) phenomena 64

4.3 Materials and methods 67

4.3.1 Photothermal optical coherence tomography system 67

4.3.2 Phantom preparation 68

4.3.3 Data acquisition and processing 70

4.3.4 Theoretical model 71

4.4. Results 73

4.4.1 Photothermal signal as a function of the absorber concentration 73

4.4.2 Photothermal signal as a function of the laser power 74

4.4.3 Photothermal signal as a function of the distance from the zero-delay line 75

4.4.4 Reconstruction of single and double layer phantoms 76

4.5 Discussion 79

4.6 Conclusions 82

Chapter 5 PT-OCT for detection of Nanoparticles 84

5.1 Introduction 85

5.2 Material and methods 88

5.2.1 System configuration 88

5.2.2 Sample preparation 89

5.3 Data Acquisition and Processing 91

5.4. Results and discussion 92

5.5 Conclusions 98

Chapter 6 Quantitative Optical Coherence Elastography (OCE) 99

6.1 Introduction 100

6.2 Mechanical properties of soft tissue 101

6.3 Current mechanical properties characterization method 104

6.4. Material and method 107

6.4.1 System configuration 107

6.4.2 Sample preparation 108

6.5 Data Acquisition and Processing 109

6.6. Results and discussion 112

6.7 Conclusions.. 119

Chapter 7 Application of Quantitative OCE in urology 121

7.1 Introduction.. 122

7.2 Background knowledge of prostate.. 123

7.2.1 Structure and function.. 123

7.2.2 Prostate diseases diagnoses.. 124

7.2.3 Prostate biopsy 128

7.3 Material and methods.. 128

7.3.1 Patient population and sample preparation 128

7.3.2 Imaging protocol.. 129

7.3.3 Static analysis 130

7.4 Results.. 130

7.4.1 2D and 3D elastography of prostate biopsies.. 130

7.4.2 Diagnostic accuracy of OCE.. 134

7.5 Discussion.. 138

7.6 Conclusions.. 141

Chapter 8 Conclusions and Further Work...142

8.1 Summary 143

8.2 Conclusions.. 144

8.3 Future work.. 145

References:...147

List of Figures

Figure 2.1 Ultrasound and elastography images of an invasive breast cancer. Ultrasound image showing a normal area with greyscale features but suspicious peri-tumoural stiffness on the elastography image (arrow). [46] 12

Figure 2.2 Incidental liver tumor (white arrow) is hyperintense on the T2-weighted image (a) and seen to intensely enhance in arterial phase of gadolinium enhanced T1-weighted image (b). Axial MRE wave image (c) showing good illumination of the tumor (ROI). Note that the waves in the tumor have slightly longer wavelength as compared to those in surrounding normal liver parenchyma. Elastogram (d) with ROI corresponding to the tumor. The shear stiffness value of the tumor was 3.1kPa and the surrounding liver, 2.4 kPa[16] 13

Figure 2.3 Michelson interferometer. Light from a low-coherence source is split into a reference and sample arm using a beam splitter. Reflections off the sample layers and reference mirror is recombined and the resulting interferometric signal measured using a photodiode detector. 15

Figure 2.4 (left) Interference pattern observed for a high coherent light source. Interference is observed for longer distance due to long coherence length. (right) Interference pattern observed for a low coherent source. Interference is observed for short distance due to smaller coherence length. Axis z indicates the optical path delay. 17

Figure 2.5 Illustration of the example discrete-reflector sample field reflectivity function and the A-scan resulting from time-domain low-coherence interferometry [48] 19

Figure 2.6 Fourier domain OCT. FDOCT techniques measure the spectral interferogram in two ways: (a) spectral domain OCT, which simultaneously measures the spectral interferogram using a spectrometer in the detection arm of the interferometer; and (b) swept-source OCT, which utilizes a light source that rapidly sweeps a narrow line-width across broad band light... 20

Figure 2.7 Fourier transform relationship. The detected spectral interferogram (d) is the combination of interferograms from reflectors at different depths in the sample (a)-(c). The Fourier transform of (d) produces an A-scan (e) where each peak location corresponds to the depth of the reflector. 21

Figure 2.8 SNR as a function of reference-arm reflectivity. Also shown are the signal-to-thermal - noise ratio (SNRth), the signal-to-shot-noise ratio (SNRsh), and the signal-to-excess-intensity noise ratio (SNRex). 28

Figure 2.9 Image from PS-OCT of in vivo human cornea [73] 30

Figure 2.10 *In vivo* conventional OCT and spectroscopic OCT of an African frog tadpole (Xenopus laevis). Mesanchymal cells of various sizes are clearly visualized. A green hue indicates a short-wavelength shift of the centre of gravity of the spectrum, and a red hue, a long-wavelength shift. Melanocytes (arrows) appear bright red, probably because of enhanced absorption of melanin at shorter wavelengths. Some melanocytes are differentiated by spectroscopic OCT that are difficult to resolve by use of conventional OCT. [31]. 32

Figure 3.1 Schematic of flow direction and probe beam angle.......................................37

Figure 3.2 OCT for blood flow detection relies on the fact that Blood flow is accompanied by both Doppler shifts (A-B) and decorrelation (C-D), leading to both shifting and broadening of the power spectrum. 39

Figure 3.3 Digital processing procedures for PhS-OCT 44

Figure 3.4 A light bulb of a flashlight seen through a transmissive grating, showing three diffracted orders. The order m = 0 corresponds to a direct transmission of light through the grating. In the first positive order (m = +1), colors with increasing wavelengths (from blue to red) are diffracted at increasing angles.[114]..48

Figure 3.5 Transmission grating geometry 49

Figure 3.6 Grating characteristic curve of diffraction efficiency versus wavelength 49

Figure 3.7 Typical schematic of the one camera PhS-OCT system: SLD – super luminescent diode, PC – polarization controller, Laser- pilot laser for beam guiding, CCD – line-scan camera. 52

Figure 3.8 Schematic of the ultrahigh speed SDOCT system. (a); and the trigger signal sequences for dual-camera system. SLD: superluminescent diode; PC: polarization controller; OC: optical circulator. (b) trigger-sequences for two cameras.......................54

Figure 3.9 System performance of the ultrahigh speed SDOCT. (a), light source spectrums captured by the two cameras of the system; (b) the PSF of the two spectrometers before (red and blue) and after (yellow and green) the digital beam shaping. (c) system sensitivity falling off curve of the two spectrometers. (d) measured optical delay line positions of the two spectrometers. (e) system axial resolution. 57

Figure 3.10 Cross-sectional structure and phase-difference images obtained from the flow phantom experiments. (a) and (b) single camera PhS-OCT structural images resulting from the first and second spectrometers, respectively. (c) Structural image from the dual-camera PhS-OCT system. (d), (e) and (f) Corresponding PhS-OCT phase difference maps evaluated from the system employing the first, second, and dual-spectrometers, respectively. (g) Phase-difference plot along the dashed line (see middle images), passing through the center of the flow-tube. The solid curves are the parabolic fitting to the measured data. 60

Figure 4.1 Schematic illustration of photothermal OCT 68

Figure 4.2 (a) M-scan structure image from a phantom that has a 1.5% concentration of India ink. (b) M-scan of the phase difference obtained from the phantom. (c) Phase difference as a function of time at a depth of 530µm below the tissue surface (arrow in (b)). (d) Absolute value of the Fourier transform of the phase difference (c). 70

Figure 4.3 (a) Absorption spectra of black India ink normalized at 808nm. (b) FFT amplitude of the phase at different depths for phantoms with different ink concentrations. (c) Mean and standard deviation of the slope of the curve *a* for different ink concentrations with 1% milk and laser power of 50.8mW. (d) Mean and standard deviation of the slope of the curve *a* for different laser powers with 1.5% ink and 1% milk. 73

Figure 4.4 Percent variation of the slope of the curve for different distances between the surface of the sample and the zero-delay line normalized to the 350µm distance...........75

Figure 4.5 Structure image for a phantom with an ink concentration of (a) 0.1%, (b) 0.5% and (c) 1.5%. Phase image for a phantom with an ink concentration of (d) 0.1%, (e) 0.5% and (f) 1.5%. Reconstructed concentration image for a phantom with an ink concentration of (g) 0.1%, (h) 0.5% and (i) 1.5%.White line of figure (i): 100µm. 77

Figure 4.6 Structure image for a phantom with a top layer ink concentration of (a) 0.1% and (b) 0.5%. Phase image for a phantom with a top layer ink concentration of (a) 0.1% and (b) 0.5%. Reconstructed concentration image for a phantom with a top layer ink concentration of (a) 0.1% and (b) 0.5%. The bottom layer ink concentration for both phantoms was 0.25%. White line of figure (f): 100µm. 78

Figure 4.7 Average A-line from the phase image (Figure 6 (d)) for a phantom with a top and bottom layer ink concentration of 0.5 and 0.25%, respectively. The image includes a line with the 0.25 and 0.5% ink slope obtained from the homogeneous phantoms.........79

Figure 5.1 Schematic illustration of GMSNP synthesis...89

Figure 5.2 Diagram of the data processing method to image the GNRs uptake in the SLN 91

Figure 5.3 (a) Illustration of the multifunctional properties of GMSNP as a contrast agent for optical imaging techniques. Transmission electron microscopy images of (b) MNP, (c) MSNP, (d) MSNP-GNRs (e) GMSNP. (f) The size distribution of each nanoparticle. (g) UV-Vis-NIR extinction of MNP, MSNP and GMSNP. The characteristic absorbance of GMSNP is red-shifted due to the outer gold shell.............92

Figure 5.4 (a) Conventional scattering and (b) photothermal OCT images of control, MSNP, MSNP-GNPs and GMSNP at a concentration of 5.0 nM. (c) depth-dependent OCT intensity decay of control and 5.0 nM GMSNP. (d) At different concentrations of GMSNP, photothermal images show distinguishable contrast, even though the concentration increases over a small range (left: 0.5 nM, middle: 1.5 nM, Right: 2.5 nM). Red spots indicate the central area of phantoms (e) Plot of photothermal signal strength at the center of each phantom in (d)...93

Figure 5.5 (a) Three-dimensional OCT projection image of a dissected SLN at 140 h after GMSNP injection. (b) 3D OCT view of SLN morphology (c) The same as in (b) but was from PT-OCT images to highlight SLN structures. (d) Schematic diagram of a dissected SLN. (Volume size = 2.5 x 2.5 x 2.0 mm) 95

Figure 5.6 Uptake of GMSNP within the SLN at different time points. 96

Figure 5.7 Average concentration of GMSNP throughout the whole SLN as a function of time..97

Fure 6.1 Typical stress-strain relation in soft biological tissues [196] 103

Figure 6.2 Schematic representation of current approaches to elastographic imaging: compression elastography (left), Dynamic elastography (middle) and transient elastography (right). 104

Figure 6.3 the principle of real time tissue elastography, illustrated here by a spring model [203]. 106

Figure 6.4 Chemical damage formed by the collagenase of various concentration of 1 mg/mL (A), 3.3 mg/mL (B), 10 mg/mL (C) by incubating the tendons for 60 minutes. 109

Figure 6.5 (a) M-scan of the phase difference obtained from the tendon-agar sample. (b) Phase difference as a function of time at a depth of ~700μm below the tissue surface {arrow in (a)}. (c) Absolute value of the Fourier transform of the phase difference (c). (d) FFT amplitude of the phase at different depths for sample (linear fit of agar layer-green line and tendon layer-blue line)..111

Figure 6.6 FFT amplitude of the phase changes caused by the shear wave amplitude at different depths and the linear model fit of (a) ~2% agar over ~1% agar and (b) ~3% agar over ~2% agar phantoms..113

Figure 6.7 FFT amplitude of the phase changes caused by the shear wave amplitude at different depths and the linear model fit of ~3% agar over ~1% agar..........................114

Figure 6.8 (a) Typical OCT image of 2% agar-tendon phantom, yellow dash line indicates the position of PhS-OCT detection beam for the phase change. (b) Averaged FFT amplitude of the phase changes caused by vibration at different depths and the linear model fit of (green) ~2% agar (blue) of control tendon......................................115

Figure 6.9 Averaged FFT amplitudes of the phase changes at different depths for the tendons treated with 1 mg/ml, 3.3mg/ml and 10mg/ml collagenase solution with 30 minutes, 60 minutes, and 90 minutes. The green and blue line are the linear model fits of ~2% agar-agar phantom and the tendon with 95% confidence bounds. 116

Figure 6.10 Overall Young’s modulus changes of collagenase treated tendon samples with different time span and different concentrations..117

Figure 6.11 Figures (a),(b),(c) are the structure images of tendon samples treated with 1mg/mL, 3.3mg/mL and 10mg/mL collagenase for 60 minutes respectively; (d), (e), (f) are the calculated Young’s modulus elastography for these three samples and the colour bars show the value in unit of KPa;(g),(h),(i) are overlaid images. (uneven parts of the tendon elastography in figure (f) could be caused by the treatment)............................118

Figure 7.1 The diagram of prostate and the surrounding organs [222].........................123

Figure 7.2 Gleason grading system diagram [228] 127

Figure 7.3 The pictures of prostate biopsy procedure and the areas of biopsy. 128

Figure 7.4 (a) Cross sectional structural image (b) the corresponding calculated Young's modulus elastography and (c) overlaid images of structural and elastograms of 1: benign prostate tissue, 2: atypical small acinar proliferation, 3: prostatic intraepithelial neoplasia (PIN), 4: malignant prostate cancer with Gleason score of 4+3, 5: prostate cancer with Gleason score of 4+4 and 6: prostate cancer with Gleason score of 4+5. The color bars show the Young's modulus value in unit of kPa, the scale is 250µm 132

Figure 7.5 3D visualization of benign and PCa (Gleason score 3+4 with cancer involvement 40%) prostate biopsies. (a, e) OCT structural image, (b, f) OCE, (c, g) overlay from en face view and (d, h) corresponding histology photo. The arrows in (f and h) indicate the beginning and end of malignancy. 134

Figure 7.6 Whisker plot showing relationship of Young's modulus (kPa) with pathological outcomes using (left) threshold method and (right) average method........135

Figure 7.7 ROC curve of PCa vs. benign using three different statistical analysis methods. 136

Figure 7.8 Comparison of cancer involvement predicted by OCE and histology..........137

Figure 7.9 Whisker plot showing relationship of Gleason score with Young's modulus (kPa) value. 138

List of Tables

Table 3.1 Physical dimensions and mechanical specification 47

Table 3.2 Specifications of Grating 50

Table 3.3 Features of SU1024-LDH2 [117] 51

Table 6.1 Young's modulus of various types of human tissue from literature 101

Table 6.2 Summary of collagenase treated tendon Young's modulus (kPa) 117

Table 7.1 Summarised Young's modulus of different category of prostate biopsies 133

Table 7.2 Comparison of AUC between prostate elasticity measurement methods 139

List of Abbreviations and Symbols

A	Area
A_i	Transmitted (incident) wave amplitude
AOI	Angle of incidence
ASAP	Atypical small acinar proliferation
AUC	Area under the curve
c	Acoustic wave velocity
CARS-OCT	Coherent anti-Stokes Raman spectroscopy optical coherence tomography
d	Displacement amplitude
DFT	Discrete Fourier Transform
DOCT	Doppler OCT
DRE	Digital rectal examination
E	Young's Modulus
E_i	Amplitudes of the electric field
F	External force
f_d	Doppler shift
FD-OCT	Frequency domain optical coherence tomography
FFT	Fast Fourier Transform
f_{obj}	Focal length of the objective lens
FWHM	Full width at half maximum
GMSNP	Gold-coated magnetic silica nanoparticle
GNRs	Gold nanorods
H&E	Hematoxylin and eosin
HGPIN	High grade prostatic intraepithelial neoplasia
HTS	High-temperature superconducting
I_0	Irradiation of laser
InGaAs	Indium Gallium Arsenide
IVUS	Intravascular Ultrasound
k	Wave vectors
K	Force constant

l_c	Coherence length
LN	Lymph nodes
mmPA	Magnetomotive photoacoustic
MNP	Magnetic nanoparticles
MRE	Magnetic resonance elastography
MRI	Magnetic Resonance Imaging
MSNP	Magnetic silica nanoparticles
NEB	Noise equivalent bandwidth
NIR	Near infrared region
OCT	Optical Coherence Tomography
OCE	Optical coherence elastography
OMAG	Optical micro-angiography
OPD	Optical path delay
OPL	Optical path length
P	Power
PCa	Prostate cancer
PIN	Prostatic intraepithelial neoplasia
PA	Converts light to sound
PAM	Photoacoustic imaging
PCI	Percutaneous coronary intervention
PDT	Photodynamic therapy
PhS-OCT	Phase sensitive optical coherence tomography
PRDOCT	phase-resolved Doppler optical coherence tomography
PSA	Prostate-specific antigen
PSF	Point spread function
PS-OCT	Polarization sensitive OCT
PT	Converts light into heat
PT-OCT	Photo-thermal optical coherence tomography
ROC	Receiver operating characteristic
ROI	Region of interest
R	Reflectivity

TEOS	Tetraethyl orthosilicate
SHG-OCT	Second harmonic generation optical coherence tomography
SLD	Super Luminescent Diode
SLN	Sentinel lymph nodes
SNR	Signal to noise ratio
SNRth	Signal-to-thermal - noise ratio
SNRsh	Signal-to-shot-noise ratio
SNRex	Signal-to-excess-intensity noise ratio
SOCT	Spectroscopic optical coherence tomography
SO_2	Oxygen saturation
SSOCT	Swept-source OCT
STFT	Short time discrete Fourier transform
T	Time duation
t	Time
TD-OCT	Time domain optical coherence tomography
THPC	Tetrakis(hydroxymethyl) phosphonium chloride
TR	Time of repetition
TRUS	Transrectal ultrasound
v	Velocity vector
z	Depth
z_R	Depth of focus
$\delta_s k$	Spectral sampling interval
δz	Axial resolution
η	Quantum yield of the detector
ε	Strain
λ	Wave length
λmax	Maximum absorbance
v	Poisson’s ratio
ρ	Density
σ	Stress
φ	Phase change

$\varDelta T$	Increase in temperature
Δx	Lateral resolution
$\Delta\lambda$	Optical bandwidth
2D	Two dimensional
3D	Three dimensional

Chapter 1 Introduction

1.1 Motivation and research objectives

Micro-motion induces unique phase modulation or Doppler modulation and offers a new way of characterizing objects. With the development of sensors, micro-motion has various applications in biomedical engineering, e.g. elastography [1-4], photo-acoustic effect [5-7], photo-thermal effect [8-10] and assessment of cochlear micromechanics [11-14], etc. To detect a micro-motion, the most common method is to employ contact ultrasound transducers. However, ultrasound elastography has a number of limitations: The transducer requires physical contact with the sample. Tumour size and cellularity both influence the appearance. Far from being perfect, ultrasound elastography is impeded by operator dependency of manually induced vibration and prob tilting as well as by various manufacturer approaches to elasticity imaging [15]. Furthermore, millimetre scale is not suitable for early-phase tumour detection. On the other hand, MRI has also been used for vibration and motion measurement, e.g., MRI is used for tracking the shear wave propagation in MR elastography (MRE). However, MRI has limited spatial resolution (lower than a few hundred micrometres) [16]. To mitigate these problems, a preferred method is to use a non-contact and non-destructive approach to detect the micro-motion. One of such methods is optical interrogation. Optical interrogation method has been widely used because it is non-contact and remote. Also the sensitivity of optical measuring system is inherently high which allows detection of significantly small displacement with a very high detection bandwidth. As a remote sensing approach, it provides access to the samples in a hostile environment and is generally not sensitive to surface orientation.

Optical coherence tomography (OCT) was first demonstrated for cross sectional retinal imaging in 1991 by a Massachusetts Institute of Technology (MIT) team headed by Fujimoto [17]. It is an interferometric imaging technique that maps reflections and scattering of near-infrared (NIR) light from tissue to form cross sectional images of morphological features at the micrometre scale. OCT instrumentation, buoyed by a stream of technological advancements, has undergone substantial improvement in the past decade. As a result, it is now well positioned for wide adoption in various other clinical and research applications, including the applications in ophthalmology [18, 19], dermatology [20], tissue engineering [21-24], cardiology and urology [25-27].

Many different functional OCT systems have been developed during the past decade. Doppler OCT can obtain high-resolution tomographic images of blood flow and tissue structure simultaneously [28]; optical micro-angiography (OMAG) can provide high-resolution capillary blood vessel networks, which is extremely helpful for the diagnosis of some diseases at the early stage and monitoring the treatment [29]; polarization sensitive OCT (PS-OCT) which utilizes depth-dependent changes in the polarization state of detected light to determine the light polarization changing properties of a sample [30]; spectroscopic optical coherence tomography (SOCT) can differentiate tissue pathologies or functional state by their spectroscopic properties [31, 32].

Optical coherence tomography, especially after the advent of Fourier domain OCT (FDOCT), is a very promising and noninvasive tool capable of providing high-speed and high-sensitivity imaging. By utilizing low-coherence interferometry, OCT performs optical ranging within a sample that enables the visualization of microstructures based on local optical scattering properties. The concept of using the phase information of the OCT signals has been explored previously to detect the sample displacement for cell dynamic change monitoring [33-37] and nanoparticle detection [38]. Recently phase sensitive optical coherence tomography (PhS-OCT) [39] has been developed to detect the micro-motion at a sensitivity of tens of pico-meters, which can be introduced by mechanically disturbing laser illumination or other stimulate methods.

The goal of this dissertation is to design and develop a fast, high sensitivity PhS-OCT system with ultra-high resolution, combine it with different modalities of vibration stimulation, e.g. laser illumination, mechanical shaker and transducer to fulfil different applications in the biomedical field, especially for clinical use. The system also provides depth-resolved microstructure information of the interrogated sample to assist the cross-validation of the functional images.

1.2 Outline of Thesis

Chapter 2 of this thesis presents an overview of the principle and development of OCT. The theory of time and Fourier-domain OCT is fully reviewed. Important parameters of the OCT system are introduced, including resolution, imaging depth, imaging speed and sensitivity. Different functional OCT and their applications are reviewed.

Chapter 3 presents and compares three kinds of Doppler OCT, i.e. traditional Doppler OCT, phase resolved Doppler OCT (PRDOCT) and phase sensitive OCT (PhS-OCT). This thesis develops and builds two kinds of PhS-OCT for further study, i.e. single and dual camera PhS-OCT systems. Detailed system setup and system performance evaluation are demonstrated. Systems that introduced in this chapter will be used for different applications in the following chapters.

Chapter 4 provides an overview of photothermal (PT) OCT as one of the application of PhS-OCT combined micro-motion detection. The background, detailed system set-up, data acquisition and processing algorisms of PT-OCT are fully demonstrated. This study is the first demonstration of using a PT-OCT model to reconstruct optically absorbing compound concentrations as a function of depth.

Chapter 5 demonstrates an application of PT-OCT, for imaging multifunctional nanoparticles as a contrast agent for enhancing the imaging quality of PT-OCT. The phantom experiment was carried out for the validation of the concept and sentinel lymph nodes (SLN) with multifunctional nanoparticles were studied to test the capability of the PT-OCT for detecting the uptake of multifunctional nanoparticles. It is also demonstrated that multifunctional nanoparticles accumulate differently within several lymph node structures, and this uptake is time dependent.

Chapter 6 introduces quantitative optical coherence elastography (OCE) that developed as the second application of PhS-OCT combine micro-motion detection. This chapter presents an overview of mechanical properties of elastic solids. The theory of quantitative OCE is presented in details along with the system setup and processing algorithms. In this chapter fundamental characterization of OCE is carried out on chicken tendon, which forms the basis of chapter 6.

Chapter 7 presents the application of quantitative OCE in clinic. The experiments involve biopsies of men with suspected prostate cancer. Quantitative 3D elastography images of biopsy cores are produced to provide direct visualization of the tissue stiffness for ease of biomedical diagnosis. The elastography images were compared with pathology reports for cross-validation and statistical analysis. It has been proven that this technique has the potential to greatly increase the utility and impact of OCE in a clinical setting, for real-time detection and characterisation of cancers.

Chapter 8 presents the conclusions of this work along with some suggestions for further study.

1.3 List of publications

Peer-reviewed full Journal Articles

Related with this thesis:

1. Chunhui Li, Guangying Guan, Yuting Ling, Ying-Ting Hsu, Shaozhen Song, Jeffrey T.-J. Huang, Stephen Lang, Ruikang K. Wang, Zhihong Huang and Ghulam Nabi, 'Detection and characterisation of biopsy tissue using quantitative optical coherence elastogaphy (OCE) in men with suspected prostate cancer', Cancer Letters, 2014, (accepted in printing).
2. **Guan, Guangying**, Li, Chunhui**,** Ling, Yuting, Yang, Ying, Vorstius, JB, Keatch, RP, Wang, RK & Huang, Z, 'Quantitative evaluation of degenerated tendon model using combined optical coherence elastography and acoustic radiation force method' Journal of Biomedical Optics, vol. 18, no. 11, 111417 (2013).
3. Chunhui Li, **Guangying Guan**, Zhihong Huang, Murry Johnstone, Ruikang K Wang, "Noncontact all-optical measurement of corneal elasticity." Optics Letters. 05/2012; 37(10):1625-7.
4. Yeongri Jung, **Guangying Guan**, Chen-Wei Wei, Roberto Reif, Xiaohu Gao, Matthew O'Donnell, Ruikang K Wang, "Multifunctional nanoprobe to enhance the utility of optical based imaging techniques." Journal of Biomedical Optics. 01/2012; 17(1):016015.
5. Chunhui Li, Sinan Li, **Guangying Guan**, Cheng Wei, Zhihong Huang, Ruikang K Wang, "A comparison of laser ultrasound measurements and finite element simulations for evaluating the elastic properties of tissue mimicking phantoms", Optics & Laser Technology. 01/2012; 44:866 - 871.
6. **Guangying Guan**, Roberto Reif, Zhihong Huang, Ruikang K Wang, "Depth profiling of photothermal compound concentrations using phase sensitive optical coherence tomography." Journal of Biomedical Optics. 12/2011; 16(12):126003.

7. Lin An, **Guangying Guan**, Ruikang K Wang, "High-speed 1310 nm-band spectral domain optical coherence tomography at 184,000 lines per second", Journal of Biomedical Optics. 06/2011; 16(6):060506.

Others:

8. Chunhui Li, **Guangying Guan**, Fan Zhang, Ghulam Nabi, Ruikang K. Wang and Zhihong Hhuang, 'Laser induced surface acoustic wave combined with phase sensitive optical coherence tomography for superficial tissue characterization: a solution for practical application', Biomedical Optics Express, 2014, (accepted in printing).
9. Chunhui Li, Shaozhen Song, **Guangying Guan**, Ruikang K Wang, Zhihong Huang, "Frequency dependence of laser ultrasonic SAW phase velocities measurements.", Ultrasonics. 06/2012; DOI:10.1016/j.ultras.2012.05.009
10. Chunhui Li, **Guangying Guan**, Sinan Li, Zhihong Huang, Ruikang K Wang, "Evaluating elastic properties of heterogeneous soft tissue by surface acoustic waves detected by phase-sensitive optical coherence tomography." Journal of Biomedical Optics. 05/2012; 17(5):057002.
11. Chunhui Li, **Guangying Guan**, Xi Cheng, Zhihong Huang, Ruikang K Wang, "Quantitative elastography provided by surface acoustic waves measured by phase-sensitive optical coherence tomography." Optics Letters. 02/2012; 37(4):722-4.
12. Chunhui Li, **Guangying Guan**, Roberto Reif, Zhihong Huang, Ruikang K Wang, "Determining elastic properties of skin by measuring surface waves from an impulse mechanical stimulus using phase-sensitive optical coherence tomography." Journal of The Royal Society Interface. 11/2011; 9(70):831-41.
13. **Guangying Guan**, Chunhui Li, Hui Shi, "Optical coherence tomography (OCT) in Brain and neural imaging", International Journal of Biomedical Engineering, 2008, vol. 31, issue. 6, pp. 342-347.

Conference Papers:

1. **Guangying Guan**; Roberto Reif; Ruikang K. Wang, "Depth profile absorber concentration reconstruction using photothermal optical coherence tomography"

Proc. SPIE 8213, Optical Coherence Tomography and Coherence Domain Optical Methods in Biomedicine XVI, 82132G (February 9, 2012);

2. Chunhui Li; **Guangying Guan** ; Zhihong Huang ; Ruikang Wang; Quantitative elastography of skin and skin lesion using phase-sensitive OCT (PhS-OCT) and surface wave method. Proc. SPIE 8213, Optical Coherence Tomography and Coherence Domain Optical Methods in Biomedicine XVI, 82132E (February 9, 2012); doi:10.1117/12.910985.3.

Chapter 2 Optical coherence tomography: an overview

2.1 Introduction

This chapter provides an overview of the state-of-art of OCT technology. The basis of an OCT system will be fully introduced. This chapter also provides a brief introduction to different kinds of functional OCT which are currently in development for the *in vivo* characterisation of tissues. The problems of current phase sensitive OCT (PhS-OCT) is summarized and the research aims of this study are proposed.

2.2 Techniques used for tissue imaging and motion detection

Micro-motion measurements for functional imaging of tissues, such as elastography and drug concentration and distribution mapping, have various applications on clinical area which could be helpful for the disease diagnosis and treatment [40-42]. The most commonly used modality for micro-motion measurement is ultrasound transducer. Ultrasound transducer requires physical contact with the sample. This requirement leads to a number of drawbacks: the sensing area is limited by the size of transducer contact area, wave energy leakage occurs at the boundary of contact area [43], and the influence of transducer weight onto the sample. MRI is another well adopted imaging technique to detecting the motions with spatial resolution of few hundred micrometres [16].

2.2.1Ultrasound imaging and elastography

Ultrasonic technique in medicine is a widely accepted tool for tissue imaging. The advantages including being non-invasive, inexpensive and inherently safe. Typical diagnostic sonography operates in the frequency range of 2 to 18 MHz with the choice of frequency chosen as a trade-off between the spatial resolution of the technique and the imaging depth of the technique.

There are four main methods that are used in medicine for the presentation of data in imaging techniques namely the A-scan, B-scan, M-scan and Doppler mode. The A-scan is the simplest form of presentation of data and consists of a display of the amplitude of echoes against distance. The B-scan or brightness scan is made up of a number of A-scans and results in the production of a pictorial display of the area under inspection. It is produced by moving the transducer probe over the body so that the body is viewed from a range of angles resulting in a range of brightness points. These are then automatically correlated with information relating to the position and orientation of the probe building a 2-D picture of the body. The M-scan is repeated A-scans in a time period. Doppler Ultrasound takes advantage of the Doppler Effect the assessment and measurement of flow and relative velocity can be measured.

The physical principle of an ultrasound scanner is the emission of high frequency acoustic waves, generated from electrical signals in a piezo-electric ultrasound transducer. An alternating electric field causes thickness variations in of the piezo-electric material. When ultrasound waves travel through tissues, part of them transmit to deeper structures, part of them reflect back to the transducer as echoes, part of them scatter, or transform to heat. For imaging purposes, the echoes reflected back to the transducer are the most interesting part. A change in the acoustic impedance of the tissue causes some of the sound to be reflected back to the transducer at the interface between different tissues in the skin, whilst the rest of the energy continues to the next interface. The amount of sound being reflected depends on the acoustic impedance differences between the materials. A large difference causes a large reflection. The sound emission is pulsed, indicating that the equipment switches automatically and very rapidly between emission of sound and the registration of sound coming back to the same transducer from the object being studied. The result is a train of pulses returning to the transducer. The time lag between emitted and reflected sound waves is a measure for the thickness of the skin. It depends on the physical distance between the interfaces and the tissue material, and can be converted into a distance once the speed of the sound is known. Estimates of the sound velocity in skin are: stratum corneum 1550 m/s; epidermis 1540 m/s; dermis 1580 m/s and subcutaneous fat 1440 m/s. As an average for normal full-thickness skin, 1577 m/s can be used [44, 45].

If the ultrasound pulse encounters reflectors whose dimensions are smaller than the ultrasound wavelength, or when the pulse encounters a rough, irregular tissue interface, scattering occurs. In this case, echoes reflected through a wide range of angles result in reduction in echo intensity. However, the positive result of scattering is the return of some echo to the transducer regardless of the angle of the incident pulse.

As ultrasound pulses travel through tissue, their intensity is reduced or attenuated. This attenuation is the result of reflection and scattering and also of friction-like losses. Longer path length and higher frequency waves result in greater attenuation. Attenuation also varies among body tissues, with the highest degree in bone, less in muscle and solid organs, and lowest in blood for any given frequency. Fluid-containing structures attenuate sound much less than solid structures so that the strength of the sound pulse is greater after passing through fluid than through an equivalent amount of solid tissue.

The ultrasound frequency decides the resolution and penetration depth of the imaging. Proper selection of transducer frequency is important for providing optimal image resolution in diagnostic ultrasound. High-frequency ultrasound waves with short wavelength generate images of high axial resolution. Increasing the number of waves of compression and rarefaction for a given distance can more accurately discriminate between two separate structures along the axial plane of wave propagation. However, high-frequency waves are more attenuated than lower frequency waves for a given distance; thus, they are suitable for imaging mainly superficial structures. Conversely, low-frequency waves with long wavelength offer images of lower resolution but can penetrate to deeper structures due to a lower attenuation. For this reason, it is best to use high-frequency transducers (up to 10–15 MHz range) to image superficial structures and low-frequency transducers (2–5 MHz) for imaging the deep tissue.

Recently, ultrasound imaging system has been developed to track vibration in the tissue. For examples, vibration or shear wave are tracked and analysed by ultrasound elastography systems to obtain the elasticity information of tissue. Fig 2.1 shows a typical shear wave ultrasound elastography from an invasive cancer.

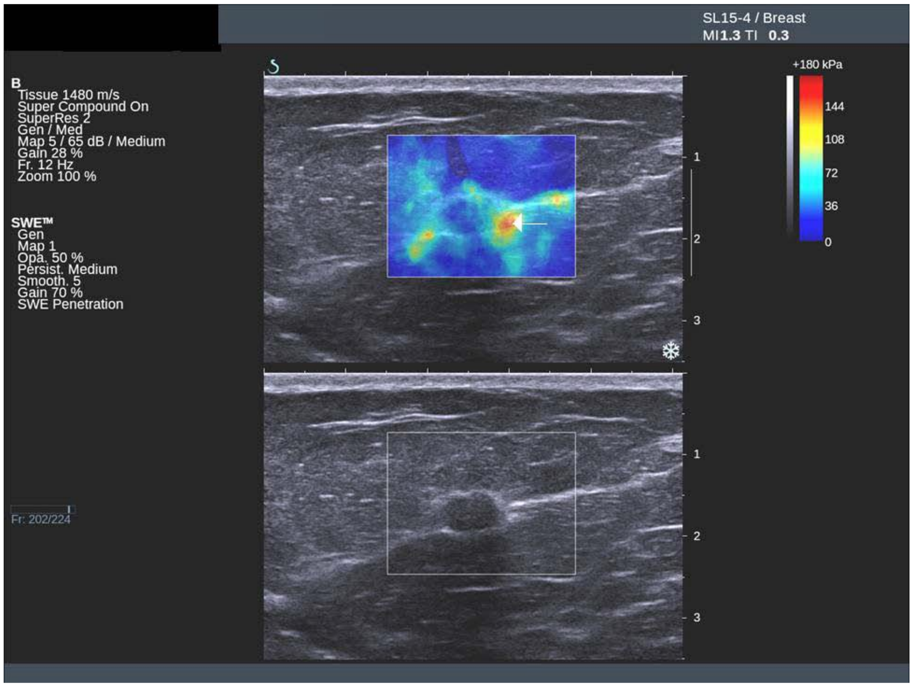

[redacted]

SL15-4 / Breast
MI1.3 TI 0.3

B
Tissue 1480 m/s
Super Compound On
SuperRes 2
Gen / Med
Map 5 / 65 dB / Medium
Gain 28 %
Fr. 12 Hz
Zoom 100 %

SWE™
Gen
Map 1
Opa. 50 %
Persist. Medium
Smooth. 5
Gain 70 %
SWE Penetration

Fr: 202/224

Figure 2.1 Ultrasound and elastography images of an invasive breast cancer. Ultrasound image showing a normal area with greyscale features but suspicious peri-tumoural stiffness on the elastography image (arrow). [46]

2.2.2 Magnetic resonance imaging (MRI)

MRI is based principally on sensitivity to the presence and properties of water. The properties and amount of water in the human body differs in different tissues and pathological conditions, which changes are reflected in the obtained MR image. This makes MRI extremely sensitive diagnostic tool. MRI is mainly concerned with the hydrogen nucleus, which consists of a single proton. Without external magnetic field, the spins have random direction. When the spins are exposed to an external magnetic field, they align with the direction of the external field. Magnetic field strength (with the unit T) is one of the key dynamics that contributes to production of higher quality images, thinner slice thickness and potentially earlier detection of pathology. When an electromagnetic field is exposed to stable spin system, it brings these spins from the equilibrium and energy can be introduced into such a stable spin system. This is called the resonance condition. MR signal rapidly fades and thus cause a return to the stable state present before excitation. Different receiving coils are designed for detecting the spin fading procedures of different parts of body, thus imaging the different amount of hydrogen nucleus which can represent the tissue structure.

Similar to ultrasound elastography, MRI can also track motions and vibrations in the tissue. By tracking shear wave propagating inside of body, MR elastography can be generated for the diagnosis of cancers [16, 47]. Figure 2.2 shows a typical MR elastography image of liver tumour from 39-year-old man. A large tumor in the right lobe of the liver was incidentally detected during an ultrasound examination. Patient underwent right hepatectomy and final diagnosis was hepatic adenoma.

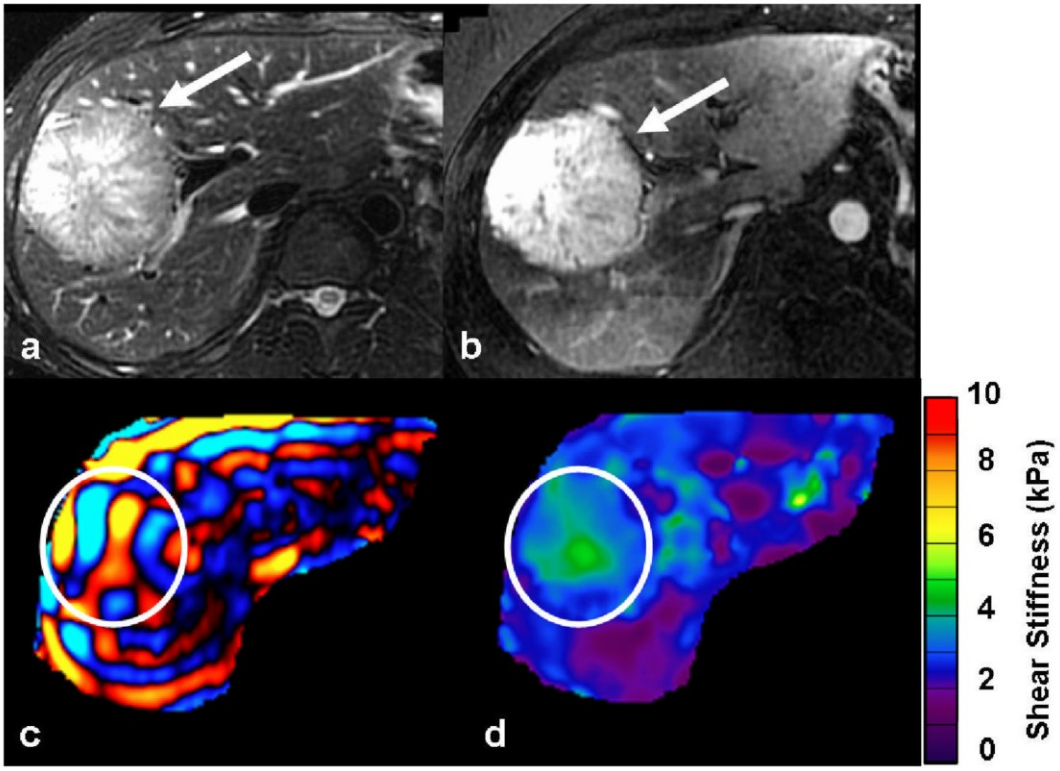

Figure 2.2 Incidental liver tumor (white arrow) is hyperintense on the T2-weighted image (a) and seen to intensely enhance in arterial phase of gadolinium enhanced T1-weighted image (b). Axial MRE wave image (c) showing good illumination of the tumor (ROI). Note that the waves in the tumor have slightly longer wavelength as compared to those in surrounding normal liver parenchyma. Elastogram (d) with ROI corresponding to the tumor. The shear stiffness value of the tumor was 3.1kPa and the surrounding liver, 2.4 kPa[16]

The advantages of ultrasound over other imaging techniques relate to its capability, versatility, portability, safety, and economic feasibility. Commercially available ultrasound imaging systems are capable of spatial resolution (~500 μm) approaching that of magnetic resonance microscopy as a result of advances in transducer and computing technology. However, there are limitations of ultrasound technique in motion tracking. Although high frequency ultrasound imaging greatly improve the resolution, it is still limited by low sensitivity of local displacement. In addition, ultrasound imaging requires the contact between ultrasound transducer and sample. It is not ideal in clinical environments.

MRI is more advantageous over other radiological techniques in analysing some tissue. One of the most advantages of MRI is its capacity for displaying soft tissue contrast. Image contrast can be tailored to the specific clinical application so that specific types of pathology are emphasized. However, the sensitivity of MRI system to phase change is relatively low. The cost of this method is much higher than other imaging methods. The MRI systems are not portable now. In addition, there are hazards intrinsic to the MR environment. It takes relatively longer time to obtain a MR image than other imaging techniques.

2.3 Basic Theory of Optical Coherence Tomography in biomedicine

OCT has emerged and developed as a rapid, non-contact and non-invasive optical imaging method which provides depth resolved cross-sectional images with micrometre scale resolution. OCT is similar to the ultrasound imaging: it measures echoes and time delays of light instead of sound. Since the speed of light ($\sim 3 \times 10^8$ m/s) is significantly higher than the speed of sound, direct time of flight imaging is not possible with the present electronic devices. Thus, OCT relies on low coherence interferometry for indirect measurement of depth ranging of echoes. These measurements of depth ranging with light were originally used in the field of optical coherence-domain reflectometry, a 1-D distance mapping technique that was developed to localize reflections from faults in fiber-optic networks. Then its potential of depth resolved imaging of layered medium was recognised and applied to practical biological applications.

2.3.1 Time-domain OCT

OCT was first introduced by Fujimoto, *et. al* [17] in 1991. It is based on low-coherence interferometry which utilizes low temporal coherent light sources (superluminescent diode) or ultra-short pulsed (femtosecond) lasers to create a coherence gating. First generation OCT systems are time-domain OCT (TDOCT) use depth-ranging to measure the time-of-flight of the optical signal reflected off of biological samples. This measurement provided depth-resolved images based on reflectivity in sample microstructure. The heart of OCT systems is a Michelson interferometer as shown in Figure 2.3.

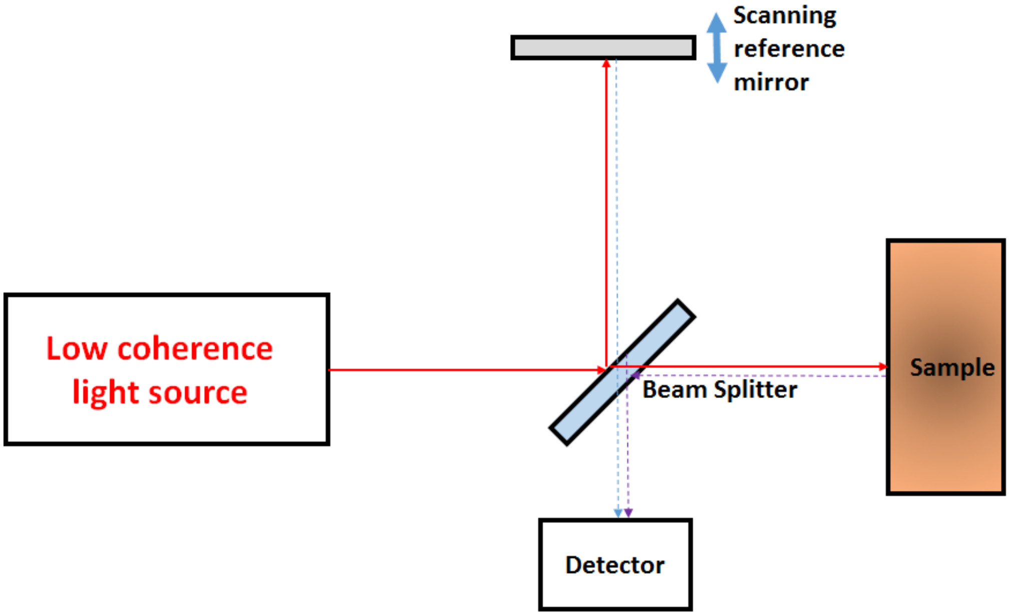

Figure 2.3 Michelson interferometer. Light from a low-coherence source is split into a reference and sample arm using a beam splitter. Reflections off the sample layers and reference mirror is recombined and the resulting interferometric signal measured using a photodiode detector.

In a Michelson interferometer, low coherent light is split into reference and sample arms using a beam splitter, or a fibre-optic coupler. Reflections off the sample are mixed with the reflection off the reference mirror. Amplitude and time-of-flight delays from the sample reflections are measured by translating the reference mirror and measuring the resultant interferometric signal using a photodiode detector. Constructive interference only occurs when the path-lengths between the reference mirror and sample reflectors are equal within the coherence length of the light source. Two-dimensional (B-mode) and three-dimensional images are created by laterally (and longitudinally) scanning the sample arm light across the sample. Assuming that $E_0 = |E_0|e^{j(\omega t - kz)}$ is the electric field of source light and E_R and E_S are the amplitudes of the electric field from reference and sample arm respectively, the intensity at the detector at any instant can be described as:

$$I_D \propto |E_R + E_s|^2 \tag{2.1}$$

$$I_D \propto |E_R|^2 + |E_s|^2 + 2|E_R||E_s|Re[\Upsilon(\tau)]\cos(\frac{2\pi}{\lambda_0}2z) \tag{2.2}$$

where $2z$ is the round trip optical path difference between reference and sample arms, λ_0 is the wavelength of the source and $\Upsilon(\tau)$ is the complex degree of coherence of the electric fields.

The complex degree of coherence $\Upsilon(\tau)$ can be defined as the normalized autocorrelation function of the electric field emitted by the light source:

$$\Upsilon(\tau) = \frac{\langle E^*(t)E(t+\tau)\rangle}{\langle E^*(t)E(t)\rangle} \tag{2.3}$$

The time delay τ between the light reaching the detector from sample and reference arms is related to the optical path difference between both the arms of the interferometer. The degree of coherence defines the temporal delay (or path delay) up to which the two light beams can interfere. The position of the reflecting interface in the sample arm can be determined with a resolution that depends on the width of the complex coherence function $\Upsilon(\tau)$ which is inversely proportional to the power spectral density. From this, it can be concluded that the broader the bandwidth of the light source used, narrower is the complex degree of coherence and hence better is the resolution of the OCT system (Figure 2.4).

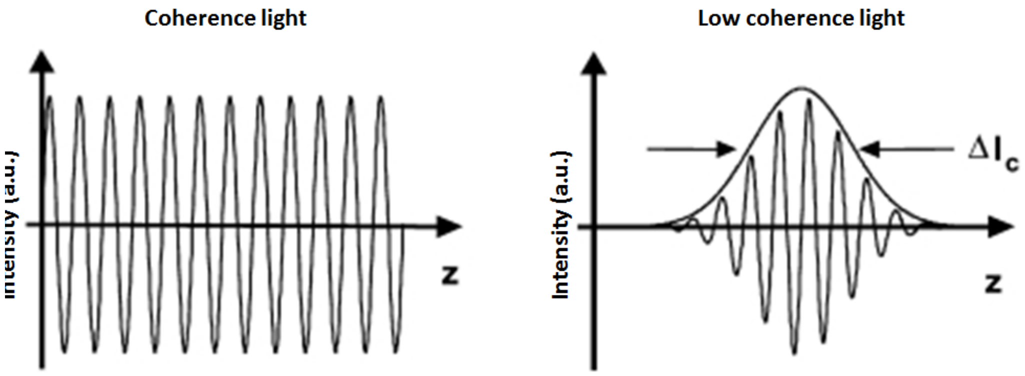

Figure 2.4 (left) Interference pattern observed for a high coherent light source. Interference is observed for longer distance due to long coherence length. (right) Interference pattern observed for a low coherent source. Interference is observed for short distance due to smaller coherence length. Axis z indicates the optical path delay.

For the normalized Gaussian power spectral density the coherence length of a light source can be defined as:

$$l_c = \frac{4ln2}{\pi}\frac{{\lambda_0}^2}{\Delta\lambda} \tag{2.4}$$

where λ_0 is the center wavelength of the source and $\Delta\lambda$ is 3 dB spectral bandwidth of the light source. Figure 2.4 left and right shows the interference patterns observed for a high coherent and low coherence source respectively. For the coherent source which has long coherence length, the interference is observed for longer distance whereas for low coherence source the interference pattern is observed for a shorter distance. To achieve better axial resolution, spectrally broader sources are used in OCT system. In case of biological samples which have multiple layers, the back-scattered light comes from all the depths. However, the interference occurs only when the path lengths in reference and sample arms match within the coherence length of the source. The reflectivity profile along the depth of the sample is acquired by varying the optical delay of reference arm mirror. The measured intensity at the detector for a varying optical path delay in reference arm is:

$$I_D \propto |E_R|^2 + |E_s|^2 + 2|E_R||E_s|Re[\mathrm{Y}(\tau)]\cos(\frac{2\pi}{\lambda_0}2z(t)) \tag{2.5}$$

Here the first and second terms of the right hand side of the Eq. 2.5 are the incoherent reflections of reference and sample fields respectively while the third term corresponds to the interference of the light between sample and reference fields. Optical path scanning with uniform velocity v in the reference arm therefore allows probing the sample at different depths and generates amplitude modulated interference signal with a carrier frequency determined by the speed of the reference path scanning. The intensity at the photodiode for time varying optical path length ($z = vt$) can be described as:

$$I_D \propto |E_R|^2 + |E_s|^2 + 2|E_R||E_s|Re[\Upsilon(\tau)]\cos(\frac{2\pi}{\lambda_0}2vt)\ )) \qquad (2.6)$$

This carrier frequency, $f_c = 2v/\lambda_0$, also known as Doppler frequency arises due to the Doppler shift in the optical frequency by moving the reference arm mirror. The strength of the oscillating signal corresponds to the ballistic component of the reflected light. The magnitude of the back-scattered or sample reflectivity can be obtained by demodulating the amplitude modulated interference signal. The depth resolved reflectivity of the sample can be obtained by varying the optical path length in reference arm. For visualization, the detected interference amplitude data is digitized and displayed as a two-dimensional grey-scale or false colour image on the computer screen. Since human eye has limited ability to differentiate the grey levels, these images are often displayed in false colour map to enhance the variation of reflectivity in the displayed images. In case of grey scale, the white colour represents the highest reflectivity while the black colour represents the lowest reflectivity. Similarly for false colour images, the colour map is chosen following the rainbow pattern where highest intensity value is represented by white or red colour while the lowest intensity is represented by black or blue colour.

In TDOCT the wavenumber-dependent detector current I_D in Eq. 2.6 is captured on a single receiver while the reference delay Z_r is scanned to reconstruct an approximation of the internal sample reflectivity profile. The resulting time-domain “A-scan” resulting from such a measurement is illustrated in figure 2.5.

There is a mechanical moving stage mounted with the mirror in reference arm in TDOCT, which performs the A-scan. The information along the longitudinal direction is accumulated over the course of the longitudinal scan time. Due to the nature of the slow mechanical moving speed, the scan time in TD-OCT is slow (~ 400 A-scans/second) which make it difficult if not impossible to perform real-time scanning.

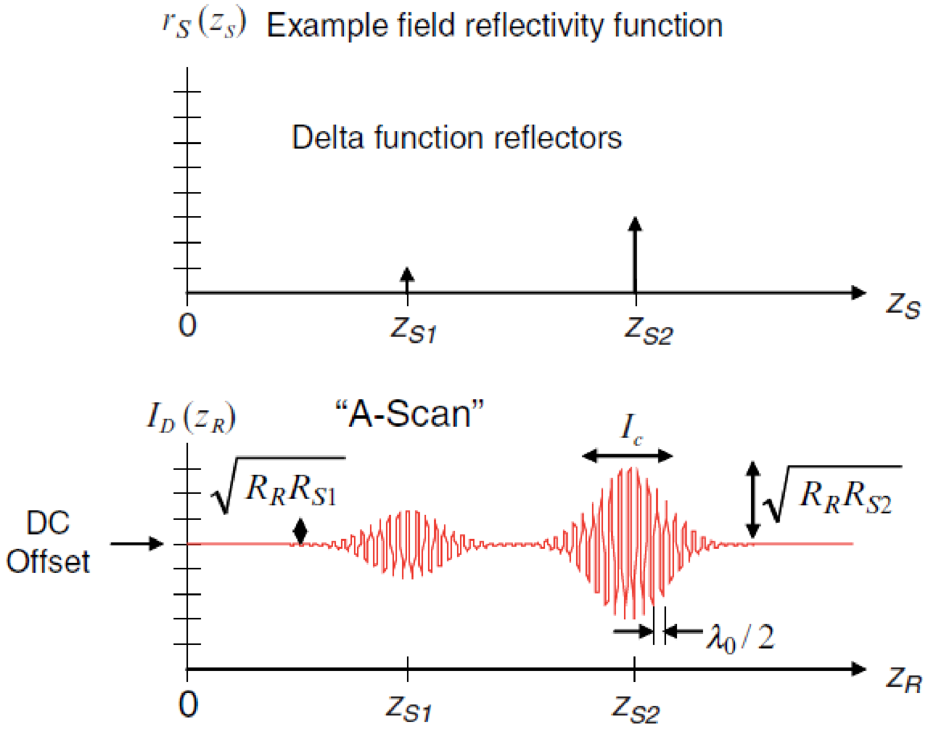
$r_S(z_S)$ Example field reflectivity function
Delta function reflectors
0
z_{S1}
z_{S2}
z_S
$I_D(z_R)$
"A-Scan"
l_c
$\sqrt{R_R R_{S1}}$
$\sqrt{R_R R_{S2}}$
DC Offset
$\lambda_0/2$
0
z_{S1}
z_{S2}
z_R

Figure 2.5 Illustration of the example discrete-reflector sample field reflectivity function and the A-scan resulting from time-domain low-coherence interferometry [48]

2.3.2 Fourier-domain OCT

Recently, a new generation of OCT technology has been developed, called Fourier-domain OCT (FDOCT). Based on Wolf's solution to the inverse scattering problem for determining the structure of weakly scattering objects, FDOCT was first demonstrated in 1995 by Fercher, e*t. al.* [49] In 2003, Leitgeb [50] and Izatt [51] showed that FDOCT techniques provide sensitivities two to three orders of magnitude greater than TDOCT. This sensitivity advantage would enable imaging hundreds of times faster than TDOCT without sacrificing image quality. FDOCT utilizes direct acquisition of the spectral interferogram for depth resolved measurement of back-scattered light. There are two methods for acquiring the spectral interferogram in FDOCT: 1) spectral-domain OCT (SDOCT) (Figure 2.3a) and 2) swept-source OCT (SSOCT) (Figure 2.3b).

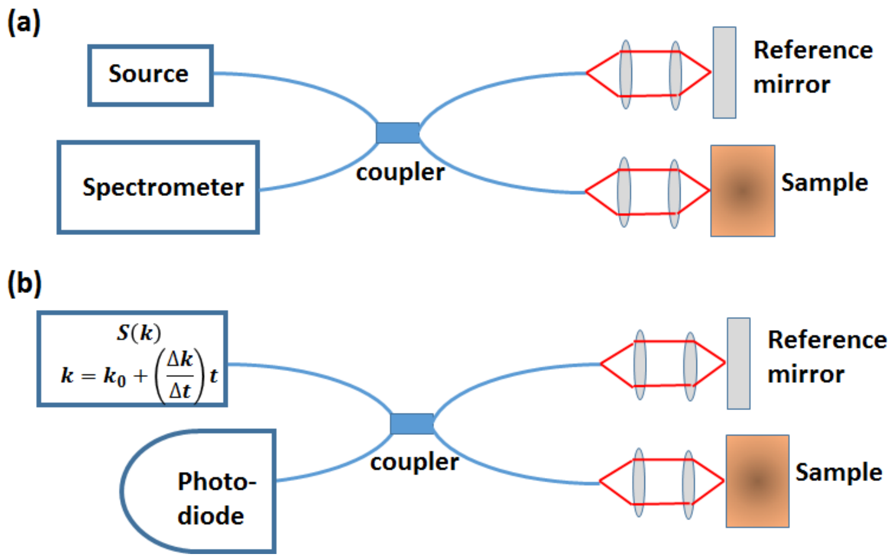

Figure 2.6 Fourier domain OCT. FDOCT techniques measure the spectral interferogram in two ways: (a) spectral domain OCT, which simultaneously measures the spectral interferogram using a spectrometer in the detection arm of the interferometer; and (b) swept-source OCT, which utilizes a light source that rapidly sweeps a narrow line-width across broad band light.

In FDOCT the reference mirror is kept at a fixed pathlength and the interferogram is measured as a function of optical wavenumber, k. In SDOCT, that spectral interferogram is acquired using a spectrometer in the detection arm of the interferometer (Figure 2.6a). The measured photocurrent signal generated by n reflectors is given by:

$$i(k) \propto S(k)\left[R_R + \sum_n R_n + 2\sqrt{R_R}\sum_n \begin{matrix}\sqrt{R_n}\cos(2k[z_R - z_n]) + \\ 2\sum_n \sum_{m\neq n}\sqrt{R_n R_m}\cos(2k[z_n - z_m])\end{matrix}\right] \tag{2.7}$$

where $i(k)$ is the detector photocurrent and $k = 2\pi/\lambda$; $S(k)$ is the source power spectral density; R_R and R_n are the reflectivities of the reference and nth sample reflector, respectively; and z_R and z_n are the positions of the reference and nth sample reflector, respectively. The first two terms in the brackets on the right-hand side represent non-interferometric spectral artefacts. The third term represents the cross-interferometric terms, and the fourth term represents the autocorrelation artefact. We calculate the back-scattered depth profile using the Fourier transform relationship between frequency and depth, as illustrated in Figure 2.7. n reflectors at various depths in the sample corresponds to a sinusoidal function with a frequency proportional to the path length difference between the reflector and reference arm (Figure 2.7a – c). The measured interferometric signal is the combination n interferograms multiplied by the source spectrum (Figure 2.4d). The Fourier transform produces an A-scan (Figure 2.7e) where each delta-function corresponds to the depth location of a sample reflector.

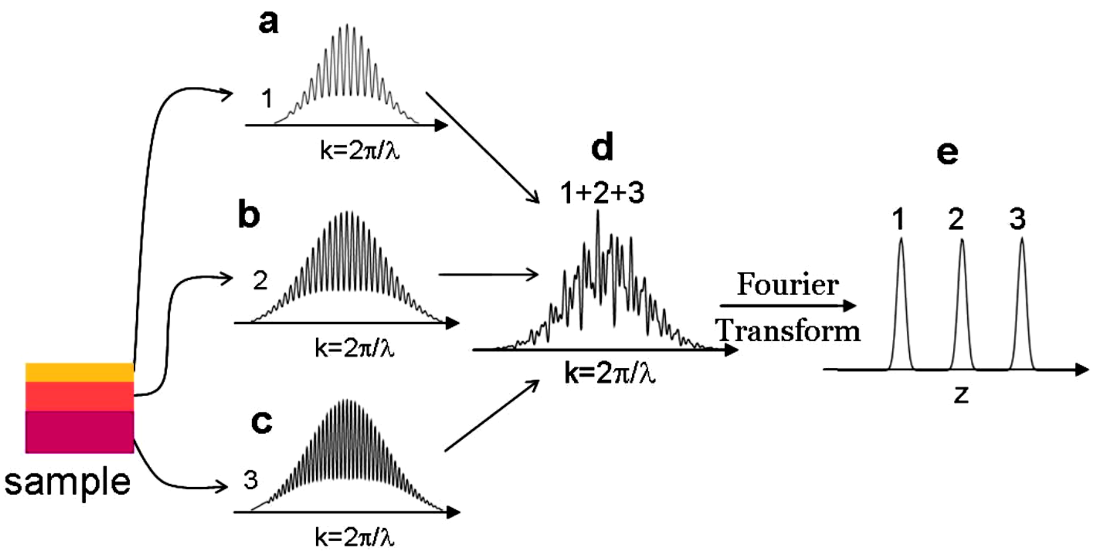

Figure 2.7 Fourier transform relationship. The detected spectral interferogram (d) is the combination of interferograms from reflectors at different depths in the sample (a)-(c). The Fourier transform of (d) produces an A-scan (e) where each peak location corresponds to the depth of the reflector.

In SSOCT, instead of using a spectrometer in the detection arm of the interferometer, a light source that rapidly scans a narrow spectral linewidth across broadband light is used. The spectral interferogram is collected, as a function of time, using a photodiode detector (Figure 2.6b). Wavenumber in Eq. 2.7 is parameterized in time t by the relationship $k = k_0 + t(dk/dt)$, where k_0 is the starting wavenumber, and dk/dt is the nonlinear sweep velocity. This sweeping leads to the conversion of pathlength differences in the auto- and cross-terms to an electronic frequency in *i(t)*, the time-varying photocurrent. The cross-frequencies have instantaneous values of $\omega_n = (dk/dt)(z_R - z_n)$, while the autocorrelation frequencies have instantaneous values of $\omega_{nm} = (dk/dt)(z_n - z_m)$. The time-varying photocurrent in SSOCT becomes:

$$i(t) \propto S(t) \left[R_R + \sum_n R_n + 2\sqrt{R_R} \sum_n \begin{matrix} \sqrt{R_n} \cos(2(\omega_R t + \phi_n)) + \\ 2 \sum_n \sum_{m \neq n} \sqrt{R_n R_m} \cos(2(\omega_{nm} t + \phi_{nm})) \end{matrix} \right] \quad (2.8)$$

Where $\phi_n = k_0 (z_R - z_n)$ and $\phi_{nm} = k_0 (z_n - z_m)$. Similar to SDOCT, the depth resolved A-scan is produced by using the Fourier transform relationship between temporal frequency and depth.

2.3.3 Applications of OCT

Since it was first introduced for human retina imaging by D. Huang et al [52], OCT and its variants are widely used in the field of biomedical imaging and diagnosis. In addition to the improvement in the OCT system hardware and performance, different methods for functional measurements of tissue beds have been developed and demonstrated as well.

One of the first applications was for imaging in ophthalmology [53, 54]. Ophthalmology is still the dominating field for OCT applications. Numerous basic as well as clinical studies, using both OCT and polarization sensitive OCT, have been performed in the last decade which have established OCT as a valuable tool for the diagnosis and monitoring of retinal diseases such as glaucoma, macular edema [53], macular hole [55] and age related macular degeneration, etc. [56].

Secondly, another important application of OCT is in cardiology. As the degree of coronary artery disease progresses, there may be near-complete obstruction of the lumen of the coronary artery, severely restricting the flow of oxygen-carrying blood to the myocardium, which result in acute heart infarction (heart attack) and threaten human life. Intravascular OCT imaging system for assessment of vulnerable plaques in coronary artery has been FDA approved for application during percutaneous coronary intervention (PCI). LightLab's C7-XR Imaging System and C7 DragonflyI Imaging Catheter become first OCT products available to U.S. interventional cardiologists for intracoronary imaging. The most important advantage of intravascular OCT is its high resolution, which can provide more detailed morphological information of arterial wall than any previously available imaging technology including intravascular ultrasound (IVUS). OCT has shown promise for intracoronary imaging and will definitely play a vital role in diagnosis and treatment of CAD and other cardiovascular diseases.

OCT is also being used in dermatology for imaging subcutaneous layers of the skin like of stratum corneum, epidermis and upper dermis [57]. OCT can identify the skin appendages (hair, sebaceous glands, sweat glands, nails) and blood vessels and helps in non-invasive monitoring of cutaneous inflammation and hyperkeratotic conditions [58]. Srinivas et al. [59] employed PSOCT to monitor burn depth in animal model and showed its potential to monitor thermal injury induced denaturization of the collagen in the skin which results in reduction of tissue birefringence. Yang et al. [60] used a Doppler OCT system for real-time monitoring of the micro-structural and micro-vascular tissue changes induced by laser thermal therapy. OCT is also a promising tool for investigating various types of skin wound as well as the wound healing.

The high scattering property of biological tissues limits the imaging depth to about a couple of millimeters only. However, in conjunction with the endoscopic and catheter-based procedures, the internal organs of the body such as gastro intestinal tract and intracoronary artery can be approached [61]. High resolution and high speed imaging are the important features of OCT that helps in detection of early neoplastic changes. The tissue architectural changes associated with early neoplasia can be observed by high resolution (a few micrometer) OCT. It can be used as a guiding tool for biopsy to reduce the false negative rates. Studies have also been performed to explore the use of OCT as a surgical guidance [62, 63]. However, the development of OCT for cancer detection will require detailed studies to investigate its capability to visualize and identify clinically relevant pathologies. Advances in OCT technology have made it possible to use OCT in other specifications like dentistry, gynaecology, urology, etc. [64-66].

2.4 Important parameters of OCT imaging

2.4.1 Resolutions

The highest priority requirements typically cited for all OCT applications including developmental biology studies, are axial and lateral resolution. In OCT systems the axial and lateral resolutions are separable. The axial (depth) resolution of the OCT system, defined as the smallest distance that can be discriminated between two tissue discontinuities. It is determined by the coherence length of the light source. The coherence length, l_c, is the spatial width of the field autocorrelation interferogram and can be determined by the Fourier transform of the source power spectrum. The axial resolution, δz, is inversely proportional to the optical bandwidth, and is determined by the following relationship:

$$\delta z = l_c = \frac{2ln2}{\pi}\frac{{\lambda_0}^2}{\Delta\lambda} \tag{2.9}$$

where $\Delta\lambda$ is the optical bandwidth, of the light source (assuming a Gaussian spectrum). For optimal axial resolution, it is desirable to utilize broadband light sources. Drexler *et. al.* [67] has provided an extensive review of light sources throughout the wavelength range of 500 nm to 1600 nm for ultra-high resolution OCT imaging.

The lateral resolution in OCT, as in microscopy, is determined by the focusing optics of the light incident on the sample. The lateral resolution, Δx, is the diffraction limited spot size on the sample and is given by:

$$\Delta x = \frac{4\lambda_0}{\pi}\frac{f_{obj}}{d} \tag{2.10}$$

where λ_0 is the centre wavelength of the light source, f_{obj} is the focal length of the objective lens and *d* is the spot size of the beam on the objective lens. There is a trade-off in the lateral resolution as a function of depth. The depth of focus is related to the lateral resolution by:

$$2z_R = \frac{\pi\Delta x^2}{2\lambda_0} \tag{2.11}$$

z_R decreases as the lateral resolution increases. Thus, tighter focusing will decrease the depth of focus and therefore the lateral resolution in regions outside of the depth of focus will suffer. It is important to consider the sample of interest and design the focusing optics to optimize the lateral resolution throughout the depth of interest. The primary sample of interest for this dissertation is the chicken embryo heart tube which typically has a diameter between 200 μm and 300 μm. In developing an OCT system for imaging the chick embryo heart tube, it is optimal to design the sample arm focusing optics to have a large enough depth of focus such that the lateral resolution is constant through the entire heart tube being imaged. To achieve a depth of focus of 200 - 300 μm the lateral resolution, while maintaining the highest resolution for the 1310 nm OCT, sample arm needs to be between 13 μm and 16 μm.

2.4.2 Imaging depth

The penetration depth of OCT imaging depends upon the wavelength and power of the light source, the system implementation, and ultimately the absorption and scattering properties of the sample under investigation. The most common light source wavelengths used in OCT are 830 nm and 1310 nm. For imaging ophthalmic structures, 830 nm is the preferred wavelength because of the increased transparency of the aqueous and vitreous humors, the higher axial resolution for the same bandwidth afforded by Eq. 2.9. For non-ophthalmic applications such as developmental biology, 1310 nm is the preferred wavelength because of reduced scattering in tissue at this wavelength. Typical penetration depths in tissues at 1310 nm are between 1-3 mm, ideal for early embryonic chick hearts which reside less than 2 mm in depth during much of the early stages of development.

The imaging depth realized using FDOCT systems is limited by two mechanisms, which do not have counterparts in time-domain OCT system: (a) the spectral sampling interval (which limits the maximum depth observable) and (b) the system spectral resolution (which leads to a falloff of SNR with depth). The maximum imaging depth in FDOCT systems is given as [68]:

$$\Delta z_{max} = \frac{1}{4\delta_s k} \tag{2.12}$$

where $\delta_s k$ is the spectral sampling interval of the FDOCT system (which is limited by the pixel spacing of the CCD in SDOCT systems).

A second parameter which limits the imaging depth in FDOCT systems is SNR falloff. Falloff is the degradation of the signal sensitivity as a function of imaging depth due to fringe washout. The -6 dB falloff depth, derived from the analysis reported by Yun, et. al. is given by:

$$\Delta z_{-6dB} = \frac{ln2}{\pi \delta_r k} \tag{2.12}$$

where Δz_{-6dB} is the imaging depth at which the signal-to-noise ratio is reduced by half and $\delta_r k$ is the spectral resolution of the system. The spectral resolution is limited by the instantaneous linewidth of the laser in SSOCT systems, and by the spectrometer optics in SDOCT systems.

2.4.3 Imaging speed

Imaging speed is an important parameter of any imaging system. Depending upon the configuration of OCT imaging system, imaging time of OCT system ranges from a few tens of seconds to a few microseconds. Since an OCT image consists of two dimensional arrangements of pixels having interference intensity information, the imaging speed is decided by the speed at which these image pixels are acquired. To generate cross-sectional images in OCT, a raster scanning is typically performed. For this both fast and slow scanning arrangements are required. The imaging speed is ultimately determined by the speed of the fast scanner and the number of fast scans required for an OCT image. The initial OCT systems used linear translation based scanning systems which were considerably slow. The use of resonant scanner based delay line which can scan at ~ 1-4 kHz scan rate could provide video rate images but with limited ~125 fast scans (A-scans for depth priority imaging) per image.

2.4.4 Sensitivity

Sensitivity, signal to noise ratio (SNR) and sometimes dynamic range are the terms used in OCT literature to define the system's capability to detect the smallest back-reflections originated from the tissue. These back-reflections arising due to small refractive index variation in tissue are very weak. However, interferometry enables optical heterodyne gain by multiplying the weak sample electric field with the strong reference arm electric field which results in an increase in the magnitude of the interference or oscillating term and thereby improves the sensitivity of the detection.

Also the scanning reference arm generates a Doppler shift in the reference arm optical frequency. The amplitude of the back-scattered light is measured by electronic filtering at the Doppler frequency. These features of OCT enables high sensitivity or SNR of the order of 10^{-9} -10^{-10} of incident power. Because of significant larger exponential term it is generally represented in dB scale i.e. 90-100 dB. The SNR of an OCT system can be expressed as:

$$Sensitivity\ (SNR) = 10log\left(\frac{\eta P}{hvNEB}\right) \tag{2.13}$$

where η is the quantum yield of the detector, P is the detected power from sample, hv is photon energy, and NEB is the noise equivalent bandwidth. The main sources of noise in OCT are thermal noise, shot noise, and excess intensity noise [69]. Figure 2.8 shows the individual SNR for these noises as a function of reference reflectivity. It can be concluded from the figure that, while the excess intensity noise dominates for high reference mirror reflectivity (Rr), thermal noise dominates for low Rr. Between these two extreme regimes is the optimum Rr, at which the SNR approaches the shot-noise limit as closely as possible. The shot noise limited regime is the optimum operation window for OCT systems.

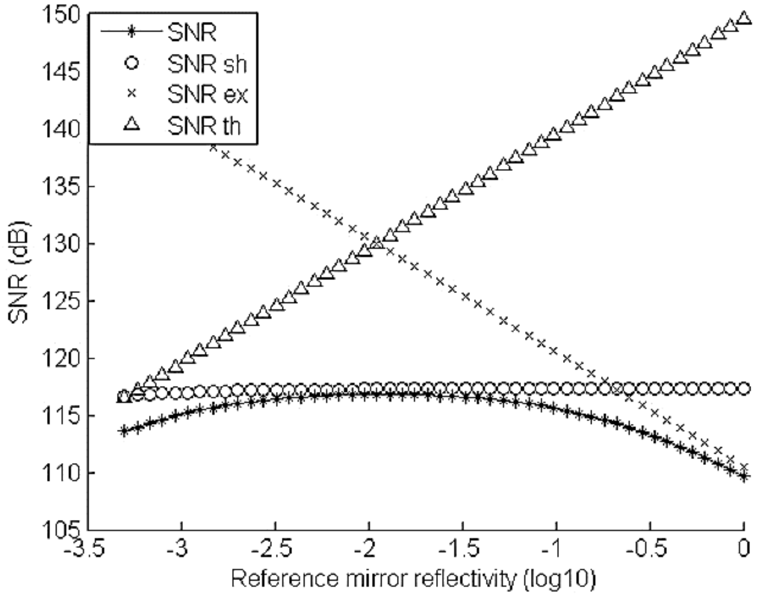

Figure 2.8 SNR as a function of reference-arm reflectivity. Also shown are the signal-to-thermal - noise ratio (SNRth), the signal-to-shot-noise ratio (SNRsh), and the signal-to-excess-intensity noise ratio (SNRex).

A higher SNR for OCT system will lead to a greater imaging depth and better image quality of OCT images. To achieve better SNR the power from sample (or source power) should be higher and the NEB should be lower. NEB depends on the imaging speed of the system and optical bandwidth of the source ($\Delta f = v\Delta\lambda/\lambda^2$). High imaging speed (or high speed reference scanning) and large spectral bandwidth of the source result in high NEB and thus degrade SNR. Hence there is a trade-off between SNR and imaging speed of the system for a given power and bandwidth of the source. In order to achieve high imaging speed for a given source power we need to compromise on sensitivity and/or axial resolution of the system.

2.4.5 Artefacts and noises

OCT images exhibit different imaging artefacts and noise components. Possible artefacts may be caused by over-exposure of the detectors at glossy or highly specular reflecting structures. Vibrations during measurements may also result in erroneous signals and may interrupt lateral structures. For highly dispersive samples dispersion compensation techniques have to be applied. Multiple scattering and back reflection at nearly parallel structures (comparable with the etalon effect) leads to delayed signals and ghost images.

In addition, different contributions of noises have to be considered: Noise caused by the electronic setup (e.g. photon shot noise, amplification noise, thermal noise at resistors), and speckle noise, resulting from the fluctuations of the propagating wave field.

2.5 Functional OCT imaging systems and applications

Conventional OCT, while imaging the structural composition of the sample, has a considerable drawback: it cannot directly differentiate between different tissues. Especially in diseases where tissue are damaged, distorted, displaced, disrupted or vanished, it is often difficult to identify specific layers based on backscattered intensity. This, however, is mandatory for correct diagnosis, monitoring, and follow up. To overcome this and other limitations, OCT can be modified to obtain additional information about material behaviour and functionality.

OCT can probe pathological aspects that alter the amplitude, phase and polarization of the scattered light. This additional information may be intimately related to functional disturbances, which usually precede morphological changes and could be useful for early diagnosis of diseases. In this context, different versions of OCT systems such as polarization sensitive OCT (PS-OCT), phase sensitive OCT (PhS-OCT), Doppler OCT, spectroscopic OCT, second harmonic generation (SHG) OCT, Coherent anti-Stokes Raman spectroscopy (CARS) OCT, etc. have been developed to provide functional information like flow velocity, birefringence and molecular information of the tissue sample under study. However, among these OCT technologies, PS-OCT, spectroscopic OCT, Doppler OCT and PhS-OCT are the OCT technologies which moved furthest while the SHG-OCT and CARS-OCT need further advancements for research as well as clinical acceptance.

2.5.1 Polarization sensitive OCT (PS-OCT)

In contrast to conventional OCT, in which only the magnitude of the backscattered light is imaged, polarisation sensitive OCT (PS-OCT) gives access to additional physical parameters like birefringence. Basically, it is the combination of OCT with polarimetry. The PS-OCT measurement apparatus is similar to that of TDOCT or FDOCT, except that it allows measurements to be made for two orthogonal polarizations by incorporation of some polarizing elements like linear polarizer and quarter wave plates and a polarizing beam-splitter. Hee et al. (1992) were the first to develop a polarisation sensitive low-coherence reflectometer and demonstrate depth resolved birefringence measurements in different samples like a wave plate, an electro-optic modulator and calf coronary artery [70]. This technique was later extended by de Boer et al. (1997) for two-dimensional mapping of the birefringence within a biological sample and used to demonstrate the birefringence changes in laser induced thermally damaged tissue [71]. Several biological tissues containing collagen and elastin fibres such as muscle, tendons exhibit birefringence. Propagation of light through these samples alters the polarization state of the light. In addition to the structural features of the tissue, polarization sensitive measurements can also be used for monitoring the ordering of birefringent constituents of the tissue [72]. The original intention for the development of PS-OCT was to identify the abnormality in tissues such as in tendon, cartilage, and muscle. Abnormalities arising from damage/disease are known to cause disruption of polarization.

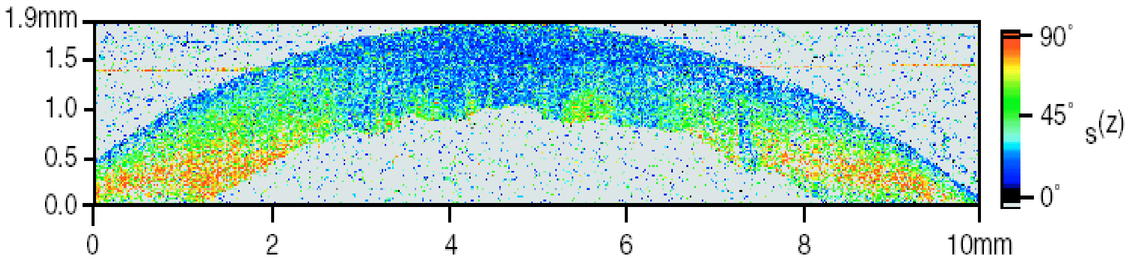

Figure 2.9 Image from PS-OCT of in vivo human cornea [73]

An example image (Figure 2.9) displays a human cornea acquired using PS-OCT. Stacked lamellae of collagen fibres create a highly anisotropic structure. In the anterior part the lamellae are oriented at various degrees to one another but in the posterior part they are nearly orthogonal. The higher signal from the posterior part indicate the more anisotropic structure.

PS-OCT has been widely applied to different clinical problems. In ophthalmology, it can provide the in vivo examination of the polarization properties of retinal nerve fibre layer [74, 75], anterior eye segment imaging [76, 77], detection of age related macular degeneration (AMD) and diabetic retinopathy [78, 79]. In dermatology, PS-OCT is helpful in wound healing [80], burn injuries monitoring [59], skin cancer detection and treatment monitoring [81]. PS-OCT can also be used in examination of articular cartilage for detection of osteoarthritis [82] and for the detection and monitoring of caries lesion progression and treatment [83, 84]. It has promising sensitivity to physiological and pathogenic changes of dentin and enamel unavailable by current diagnostic or imaging methods [85].

2.5.2 Spectroscopic OCT

Spectroscopic optical coherence tomography (SOCT) is also a functional extension of OCT which performs depth-resolved spectroscopic measurements in addition to the morphology of the tissue, making it possible to differentiate tissue pathologies or functional state by their spectroscopic properties [69]. Spectral information can be obtained by measuring the full interference signal and using appropriate digital signal processing. Since there are two mechanisms for the modification of the light spectrum in tissue: scattering and absorption, therefore, depending on the contrast mechanism, the applications of SOCT imaging can be classified into two imaging modes: absorption-mode SOCT and scattering-mode SOCT. Endogenous (melanin, haemoglobin, etc.) or exogenous (contrast-enhancing dye) materials with characteristic absorption profiles can be used to provide spectroscopic contrast based on wavelength dependant absorption [86]. Similarly, wavelength-dependant scattering alters the spectral modulations present in spectroscopic OCT signal which can also be used for enhancement of contrast in OCT image [86].

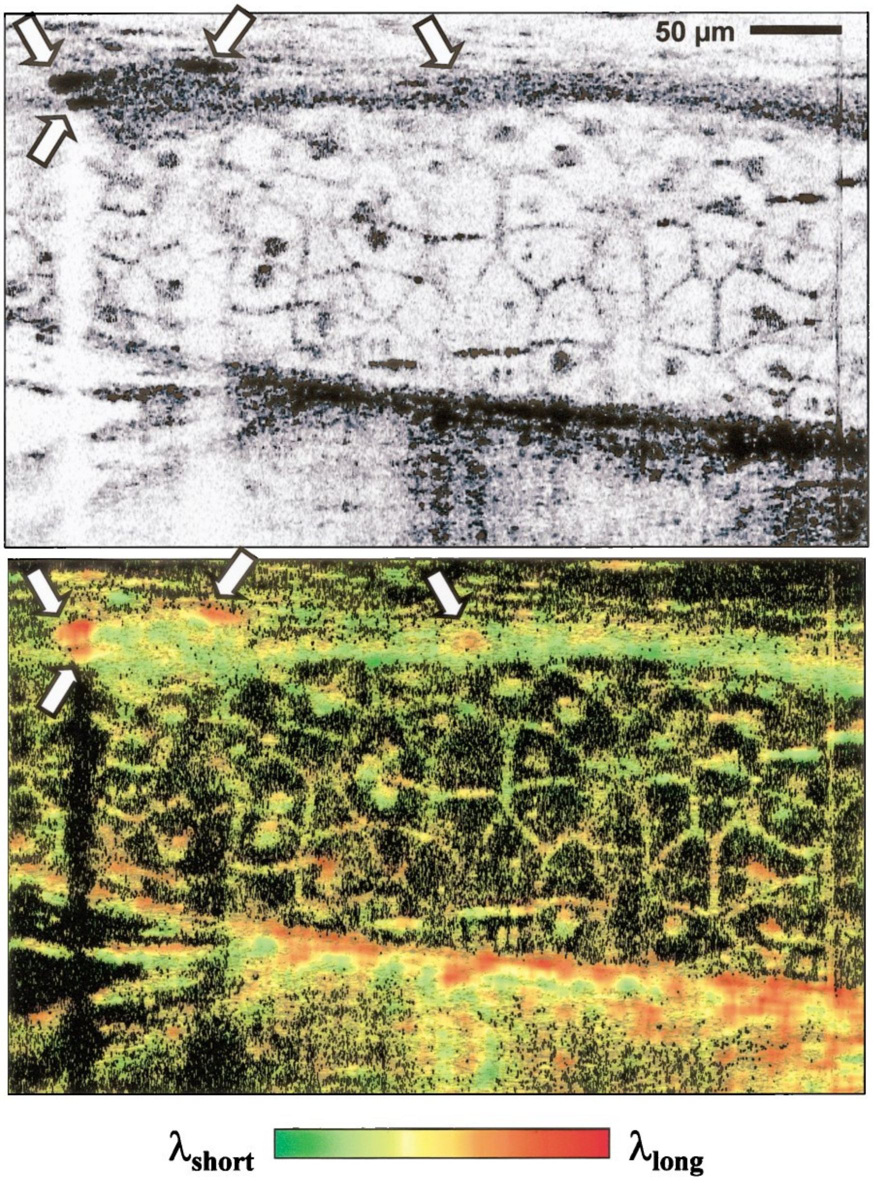

Figure 2.10 *In vivo* conventional OCT and spectroscopic OCT of an African frog tadpole (Xenopus laevis). Mesanchymal cells of various sizes are clearly visualized. A green hue indicates a short-wavelength shift of the centre of gravity of the spectrum, and a red hue, a long-wavelength shift. Melanocytes (arrows) appear bright red, probably because of enhanced absorption of melanin at shorter wavelengths. Some melanocytes are differentiated by spectroscopic OCT that are difficult to resolve by use of conventional OCT. [31].

An example image of SOCT is shown in Figure 2.10 which takes Xenopus laevis (African frog) tadpole as sample. The top part of Figure 2.10 shows conventional B-frame structure image of the sample while the bottom part shows the spectral enhanced image. A red hue indicates a long wavelength enhancement of the backscattered light, whereas a green hue is a short-wavelength enhancement. The spectroscopic OCT image is consistent with the fact that longer wavelengths penetrate deeper than shorter wavelengths. The shallower structures have a green hue, whereas deeper structures have a red hue. Melanocytes appear bright red in the spectroscopic OCT image, indicating that they are strongly scattering and that they red shift light. It probably because of enhanced absorption of melanin at shorter wavelengths. The pigmented layer below the cell layer appears red in the spectroscopic OCT image. A melanocyte that is difficult to identify in the conventional OCT image is visible in the upper middle of the image.

One application is measuring the oxygen saturation (SO_2) of hemoglobin in blood based on its SO_2-dependent absorption spectrum [87, 88]. Although other photonic methods for pulse oximetry are currently employed, SOCT has the potential to assess SO_2 over a small imaging volume (such as a single blood vessel). In addition, it is possible to use the SOCT to estimate the dye concentration. Beyond molecular contrast imaging, another important application of absorption contrast imaging is to monitor the diffusion of photosensitizers used in photodynamic therapy (PDT). However, to date, they have been primarily used for their overall scattering enhancement in standard OCT.

2.5.3 Doppler OCT

The principle of Doppler shift of light scattered from moving particles is being exploited by laser Doppler velocimetry for the determination of flow velocities. Combining these approaches with OCT imaging leads to Doppler OCT (DOCT) which simultaneously gives access to structural data and velocity profiles of flowing, scattering media, and most importantly also of flowing media embedded in scattering structures [48, 89]. The first report that measured localized flow velocity with coherence gating was demonstrated in 1991 [90]. The first two-dimensional in vivo DOCT imaging was demonstrated in 1997 [89, 91]. Currently, Doppler OCT imaging has been demonstrated on tissue phantoms, embryos, small animal skin-flap models, etc. and also on *in-vivo* blood flow in the skin and in retina [92-94].

In early DOCT systems, the Doppler frequency shift was obtained by a spectrogram method which used short time fast Fourier transformation or wavelet transformation [89, 95, 96]. However, spectrogram methods suffer from low sensitivity and are limited for imaging speed. Phase-sensitive DOCT was developed to overcome these limitations. This method uses the phase change between sequential A-line scans for velocity image reconstruction [97-99]. Phase-sensitive DOCT decouples spatial resolution and velocity sensitivity in flow images and increases imaging speed by more than two orders of magnitude without compromising spatial resolution and velocity sensitivity [97]. The first demonstration of Phase-sensitive DOCT was based on time domain OCT systems [97, 98]. Recently, the development of Fourier domain OCT systems has greatly improved the imaging speed and sensitivity [50, 51, 100]. Phase-sensitive DOCT in Fourier domain systems have been demonstrated by several groups [92, 93, 101, 102]. Further development of DOCT and phase sensitive DOCT called phase sensitive OCT (PhS-OCT). PhS-OCT is method uses the phase change between sequential B-frames. Such an approach has been shown to be capable of measuring tissue internal deformations as small as a few microns and has seen promising applications in the investigations of arterial wall biomechanics, atherosclerotic plaques, and engineered and developing tissues.

This thesis aims to detect micro-motion in biology tissue using OCT systems. Micro-motion causes phase changes that can be detected using Doppler OCT systems. Thus, Doppler OCT are considered to be utilised in this research. Detailed principles will be introduced and discussed in Chapter 3.

2.6 Conclusion

Although different imaging techniques are available in biomedicine now, very limited applications have been taken place in the detection of micro-motion. It is because there is no ideal technique available to provide high resolution and high sensitive measurement.

Comparing to other imaging techniques, OCT imaging technique has great advantages: it can provide high sensitivity of motion measurement. It can provide high resolution of tested samples, with low cost, portable nature and relatively acceptable imaging depth. It is also a non-contact method which applicable in varies environments. Thus, this study chooses OCT as a base, and develops its application in micro-motion measurement, which aims to provide quantitative characterisation of biological tissues.

Taking advantages of high resolution image provided by OCT technique, a system will be developed, which allows the rapid quantitative functional characterisation of tissue in motion or vibration. Thus in next Chapter, the principle of motion detection of OCT will be introduced. The OCT system will be designed and developed for the usage of different application of micro-motion in biological tissues.

Chapter 3 Phase sensitive OCT (PhS-OCT) and dual camera system: principles and development

3.1 Introduction

A phase change caused by micro-motion can be detected by Doppler optical coherence tomography (DOCT). Thus, DOCT is ideal to be utilized as a functional OCT technique to detect micro-motion in this thesis. With the development of OCT technology, traditional DOCT is developed to phase-resolved DOCT (PRDOCT) then phase sensitive OCT (PhS-OCT) with significant improvement of sensitivity of phase change detection. In this chapter, the principles of traditional DOCT, PRDOCT and PhS-OCT will be introduced. The advantages and disadvantages of them are compared and discussed, from which the system that will be utilized in this thesis can be determined.

The experimental OCT system development and setup will be introduced in this chapter. Here, two PhS-OCT systems are designed and built: single camera PhS-OCT and dual camera PhS-OCT system.

3.2 The development of Doppler optical coherence tomography (DOCT)

3.2.1 Traditional Doppler OCT

Doppler OCT combines the Doppler principle with OCT to obtain high resolution tomographic images of static and moving constituents in high scattering media. Figure 3.1 shows a qualitative visualization of dynamics in the time and frequency domains of blood flow caused Doppler shifts and decorrelation in OCT signal.

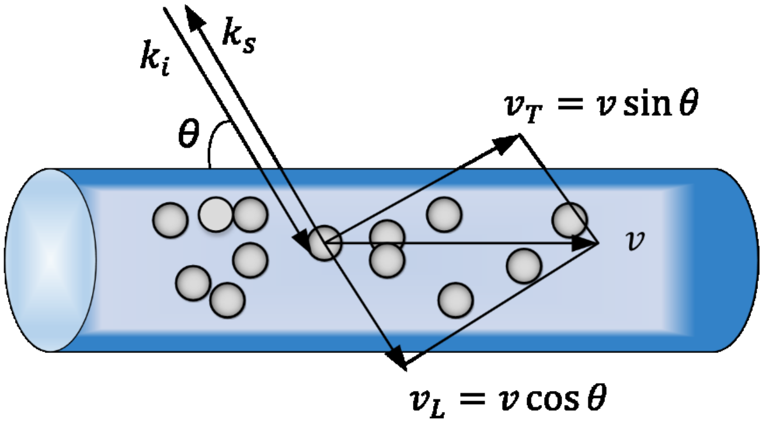

Figure 3.1 Schematic of flow direction and probe beam angle

Doppler shifting (the axial motion of red blood cell) causes a pure rotation of the OCT signal in the complex plane, and leads to a frequency shift of the power spectrum, figure 3.2 (A-B). Decorrelation (both axial and transverse motion of red blood cell) causes random deviations of the OCT signal in the complex plane, and leads to a broadening of the power spectrum figure 3.2 (C-D). When light backscattered from a moving particle interferes with the reference beam, a Doppler frequency shift f_d occurs in the interference fringe:

$$f_d = \frac{1}{2\pi}(k_s - k_i) \cdot v \tag{3.1}$$

Where k_i and k_s are wave vectors of incoming and scattered light, respectively, and v is the velocity vector of the moving particle (Figure 3.1). Since Doppler OCT measures the backscattered light, assuming the angle between flow and sampling beam is θ, the Doppler shift equation is simplified to:

$$f_d = \frac{2V cos\theta}{\lambda_0} \tag{3.2}$$

Where λ_0 is the vacuum centre wavelength of the light source.

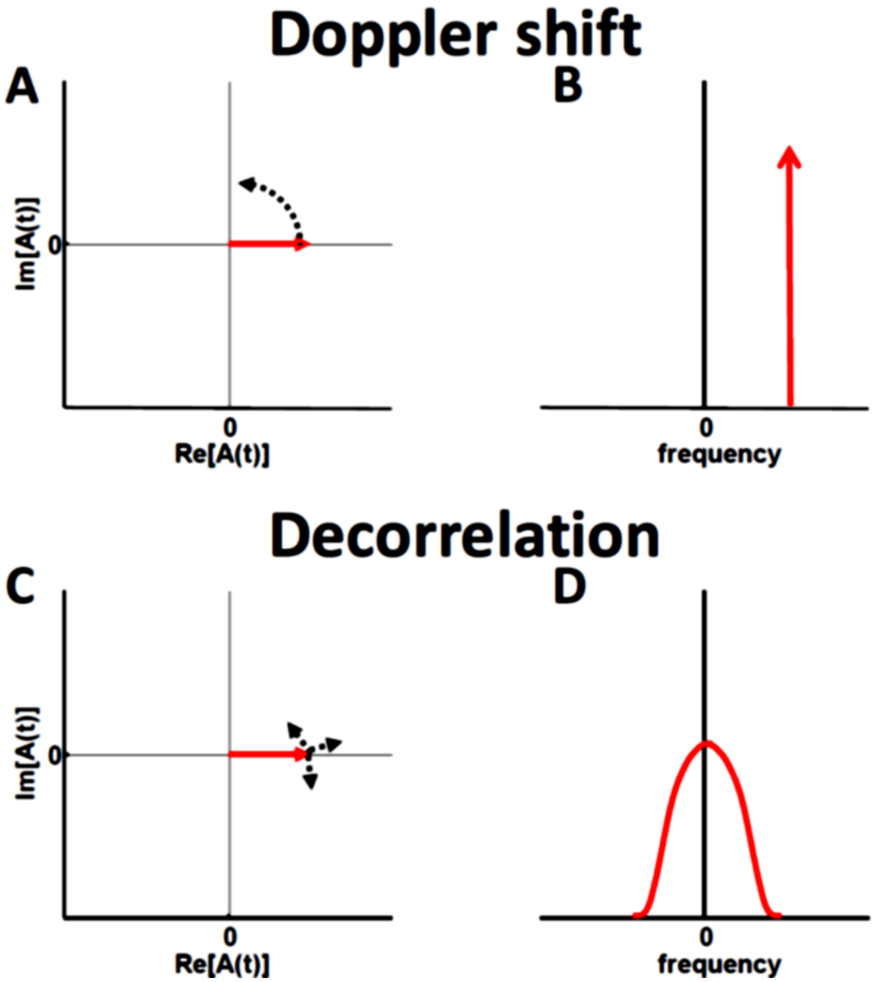

Figure 3.2 OCT for blood flow detection relies on the fact that Blood flow is accompanied by both Doppler shifts (A-B) and decorrelation (C-D), leading to both shifting and broadening of the power spectrum.

Currently, the main application of DOCT is the functional imaging of blood flow mapping of biological tissues. By analyzing the Doppler effect of a flowing particle on light frequency, DOCT allows the quantification of the blood flow speed. However, traditional DOCT meets some drawbacks, e.g. the sensitivity for imaging the flow velocity by decoupling the spatial resolution and velocity sensitivity is relatively low. With the development of DOCT, phase-resolved Doppler OCT (PRDOCT) technique is developed [95, 103]. Compared to traditional Doppler OCT, PRDOCT provides a number of strategies to enable better contrast and detection sensitivity of phase changes. The following paragraph will introduce the theory of PRDOCT.

3.2.2 Phase-Resolved Doppler OCT (PRDOCT)

Phase change between sequential scans was used to construct the flow velocity image. The phase information of the fringe signal can be determined from the complex analytical signal $\tilde{\Gamma}_{(t)}$, which is determined through analytic continuation of the measured interference fringe function, $\Gamma_{(t)}$, using a Hilbert transformation:

$$\tilde{\Gamma}_{(t)} = \Gamma_{(t)} + \frac{i}{\pi} P \int_{-\infty}^{\infty} \frac{\Gamma_{(t)}}{\tau - t} d\tau = A(t) e^{i\emptyset(t)} \tag{3.3}$$

where P denotes the Cauchy principle value, i is the complex number, and $A(t)$ and $\emptyset(t)$ are amplitude and phase term of $\tilde{\Gamma}_{(t)}$, respectively. Because the interference signal $\Gamma_{(t)}$ is quasi-monochromatic, the complex analytical signal can be determined by:

$$\tilde{\Gamma}_{(t)} = 2 \int_0^{+\infty} \int_0^{+\tau} \Gamma(t') \exp(-2\pi i v t') dt' \exp(2\pi i v t) dv \tag{3.4}$$

where τ is the time duration of the fringe signal in each axial scan.

The Doppler frequency shift f_n at nth pixel in the axial direction is determined from the average phase shift between sequential A-scans. This can be accomplished by calculating the phase change of sequential scans from the individual analytical fringe signal:

$$f_n = \frac{\Delta\phi}{2\pi T} = \frac{1}{2\pi T} \sum_{m=(n-1)M}^{nM} \sum_{j=1}^{N} \left[\tan^{-1}\left(\frac{Im\tilde{\Gamma}_{(j+1)}(t_m)}{Re\tilde{\Gamma}_{(j+1)}(t_m)} \right) - \tan^{-1}\left(\frac{Im\tilde{\Gamma}_{(j)}(t_m)}{Re\tilde{\Gamma}_{(j)}(t_m)} \right) \right] \tag{3.5}$$

Alternatively, the phase change can also be calculated by the cross correlation method:

$$f_n = \frac{1}{2\pi T} \tan^{-1}\left(\frac{Im\left[\sum_{m=(n-1)M}^{nM} \sum_{j=1}^{N} \tilde{\Gamma}_{(j)}(t_m) \cdot \tilde{\Gamma}^*_{(j+1)}(t_m)\right]}{Re\left[\left[\sum_{m=(n-1)M}^{nM} \sum_{j=1}^{N} \tilde{\Gamma}_{(j)}(t_m) \cdot \tilde{\Gamma}^*_{(j+1)}(t_m)\right]\right]} \right) \tag{3.6}$$

where $\tilde{\Gamma}_{(j)}(t_m)$ and $\tilde{\Gamma}^*_{(j+1)}$ are the complex signals at axial time tm corresponding to the j th A-scan and its respective conjugate; $\tilde{\Gamma}_{(j+1)}$ and $\tilde{\Gamma}^*_{(j+1)}(t_m)$ are the complex signals at axial time tm corresponding to the next A-scan and its respective conjugate; M is an even number that denotes the window size in the axial direction for each pixel; N is the number of sequential scans used to calculate the cross correlation; and T is the time duration between A-scans. Because T is much longer than the pixel time window within each scan used in the spectrogram method, high velocity sensitivity can be achieved.

In addition to the local velocity information, the standard deviation of the Doppler spectrum gives the variance of local velocity and can be determined from the measured analytical fringe signal:

$$\sigma^2 = \frac{\int_{-\infty}^{\infty}(f - f_D)^2 P(f)\mathrm{d}f}{\int_{-\infty}^{\infty} P(f)\mathrm{d}f} = \frac{1}{(2\pi T)^2}\left(1 - \frac{\left|\sum_{m=(n-1)M}^{nM}\sum_{j=1}^{N}\tilde{\Gamma}_{(j)}(t_m)\cdot\tilde{\Gamma}_{(j+1)}^{*}(t_m)\right|}{\frac{1}{2}\sum_{m=(n-1)M}^{nM}\sum_{j=1}^{N}\left[\tilde{\Gamma}_{(j)}(t_m)\cdot\tilde{\Gamma}_{(j)}^{*}(t_m) + \tilde{\Gamma}_{(j+1)}(t_m)\cdot\tilde{\Gamma}_{(j+1)}^{*}(t_m)\right]}\right) \tag{3.7}$$

where $P(f)$ is the Doppler power spectrum and f_D is the centroid value of the Doppler frequency shift. The σ value depends on the flow velocity distribution. Variations in flow velocity will broaden the Doppler frequency spectrum and result in a large σ value. Thus, the Doppler variance image can be an indicator of flow variations and can be used to study flow turbulences. In addition, Doppler variance imaging can also be used to map microvasculature, because it is less sensitive to the random direction and the pulsatile nature of blood flow in small vessels [97, 104]. Finally, standard deviation imaging can also be used to determine the transverse flow velocity [105].

PRDOCT decouples spatial resolution and velocity sensitivity in flow images and increases imaging speed by more than two orders of magnitude without compromising spatial resolution and velocity sensitivity. In addition, because two sequential A-line scans are compared at the same location, speckle modulations in the fringe signals cancel each other and, therefore, will not affect the phase difference calculation. Consequently, the phase-resolved method reduces the speckle noise in the velocity image. Furthermore, if the phase difference between sequential frames is used, the velocity sensitivity can be further increased. In addition to digital processing of the fringe signal using Hilbert transformation, the complex analytical signal can also be achieved through hardware implementation. Optical Hilbert transformation using polarization optics has been implemented for real-time PRDOCT imaging.

3.2.3 Phase sensitive OCT (PhS-OCT)

Recently, a technique based on the measurement of phase changes in complex OCT images has been developed to map tissue deformations in real time. It is similar to phase-resolved Doppler OCT and that uses phase changes between successive A scans to determine the tissue Doppler frequencies and thereby the localized deformations. By relying on the phase changes between the adjacent A scans, this approach, however, is not capable of measuring very small tissue deformations (< 1um) between successive B scans when the sample is subjected to slow dynamic compression. An alternative, but similar, approach that uses the phase changes between successive OCT-B scans to visualize and quantify in real time minute tissue deformations, thus enabling the creation of micro-strain rate and micro-strain maps of tissue subjected to a slow, dynamic compression force. This PhS-OCT approach achieves extremely high sensitivity in characterization of tissue deformation, resolving deformations as small as 0.26 nm [39] with a spectral domain OCT system.

The intensity of the interference pattern captured can be expressed as follows:

$$I(k) = S(k)R_k + S(k)R_s + 2S(k)\sqrt{R_R R_S}\cos(2k\Delta d + \theta) \tag{3.8}$$

Where k is the wavenumber, $S(k)$ is the spectral density of the light source, R_R and R_s are the reflectivities from the reference surface and the sample surface, respectively, Δd is the optical path-length delay (OPD) between the sample and the reference signals, and θ is a constant phase term.

The first two expressions in Eq. (3.8) are constants for a given setup, thus the intensity is modulated by the cosine expression. The challenge is to determine the phase expression and extract the depth information from it:

$$\varphi(k) = 2k\Delta d + \theta \tag{3.9}$$

To determine the OPD, the phase function needs to be unwrapped. The slope of the phase function is used and combined with the phase value to increase depth precision. Several single frame methods have been proposed for the calculation of the phase [106]. Such as wavelet transform [107], Fourier transform [108], windowed Fourier transform

[109], Hilbert transform [110], and spatial shifting [111]. The critical part is spatial phase shifting to indicating the phase reconstruction does not suffer from huge errors. Take the Fourier transform method for example: first, perform a Fourier transform on the spectral data giving the depth space. Then an inverse Fourier transform is applied for turning to wavenumbers space and giving the complex expression:

$$\tilde{I}(k) = 2S(k)\sqrt{R_R R_S}\,\exp[j(2k\Delta d + \theta)] \tag{3.10}$$

The phase term can be expressed as:

$$\varphi(k) = \tan^{-1}\left(\frac{Im(\tilde{I})}{Re(\tilde{I})}\right) \tag{3.11}$$

To unwrap the phase function, first, a least –square algorithm is used to determine the slop of the phase as a function of the wavelength. Then, the slope of the phase function is used as the reference to remove 2π ambiguity, and one phase component is chosen to give the absolute OPD as:

$$\Delta d = \frac{\varphi(k_i)}{2k_i} + \frac{\pi}{k_i}\left[floor\left(\frac{\varphi'}{2\pi}\right)\right] \tag{3.12}$$

where φ' is the phase that calculated from the slope of the phase function. An illustration of the process is shown in Figure 3.3.

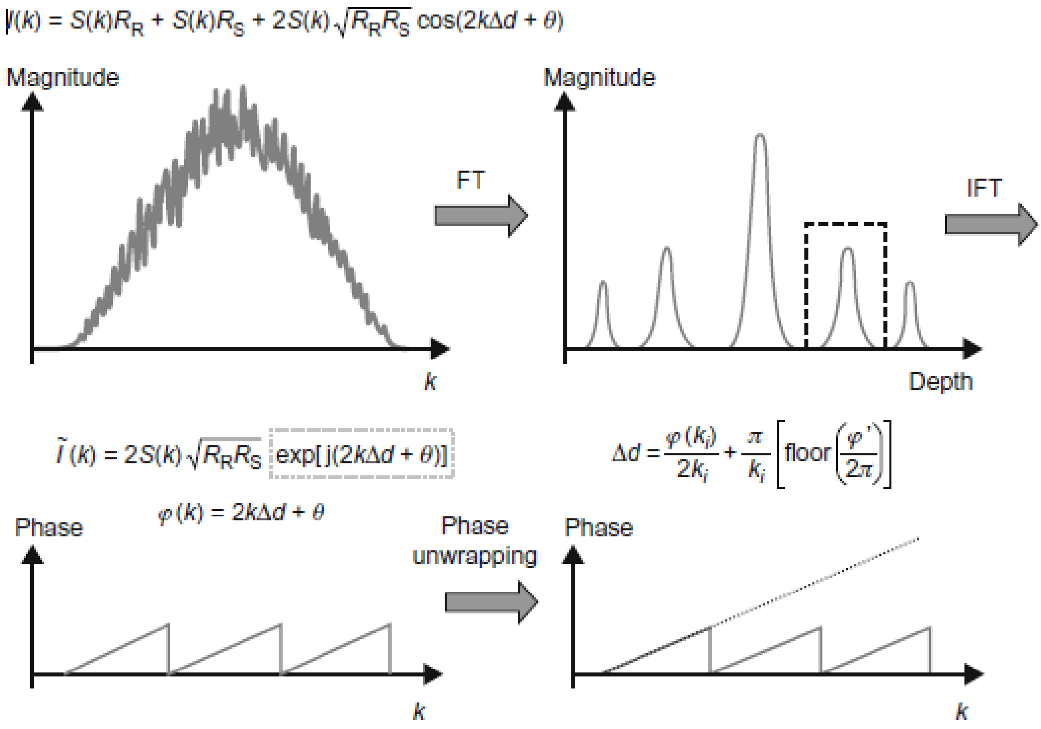
$I(k) = S(k)R_R + S(k)R_S + 2S(k)\sqrt{R_R R_S}\cos(2k\Delta d + \theta)$
Magnitude
k
FT
Magnitude
Depth
IFT
$\tilde{I}(k) = 2S(k)\sqrt{R_R R_S}\exp[j(2k\Delta d + \theta)]$
$\Delta d = \frac{\varphi(k_i)}{2k_i} + \frac{\pi}{k_i}\left[\mathrm{floor}\left(\frac{\varphi'}{2\pi}\right)\right]$
Phase
$\varphi(k) = 2k\Delta d + \theta$
Phase unwrapping
Phase
k
k

Figure 3.3 Digital processing procedures for PhS-OCT

3.2.4 Comparison between the DOCT technologies

Traditional DOCT was unable to achieve simultaneously both high velocity sensitivity and high imaging speed [89]. Typical phase stability for a spectrometer-based DOCT is a few milliradians. For swept-source based FDOCT, the phase stability can also reach a few milliradians to tens of milliradians range after phase correction. Assuming the A-line rate of the OCT system is 100,000 A-lines per second, the phase stability of the system is 10 milliradians and the refraction index is 1.4, the minimum velocity (along the incident beam direction) that can be resolved by an DOCT system with a central wavelength of 1.3 µm is around 74 µm/s.

PRDOCT uses the phase change between sequential A-line scans for velocity image reconstruction, which has been significantly improved to overcome limitations of sensitivity. As mentioned before, PRDOCT decouples spatial resolution and velocity sensitivity in flow images and increases imaging speed by more than two orders of magnitude without compromising spatial resolution and velocity sensitivity. A minimum velocity sensitivity as low as 100 μm/s with a resolution of 100 μm/s could be achieved, by relying on the phase changes between the adjacent A-scans, this approach, however, is not capable of measuring very small tissue deformations ($< 1\mu m$) between successive B scans when the sample is subjected to slow dynamic compression.

As higher speed detectors were developed, PhS-OCT was proposed to overcome the limitation by measuring phase changes between OCT-B scans, it was reported to be able to resolving deformations as small as 0.26 nm [39]. Thus, PhS-OCT is selected as the experimental system for the micro-motion detection for its extremely high sensitivity in characterization of motions. In the next section of this chapter, two kinds of PhS-OCT systems are designed, developed and built: single camera and dual camera PhS-OCT systems.

3.3 Development of Single camera PhS-OCT system

3.3.1 Background

High speed OCT system is required in order to detect the micro-motions in real time, and get 3D volume structure image of sample. Consequently TDOCT is eliminated for its low scanning speed due to the slow mechanical moving speed of reference arm. For FDOCT, though SSOCT demonstrated several advantages in many aspects, such as lower sensitivity loss along depth direction, longer imaging depth, and higher imaging speed and so on [112, 113], the commercial application of SSOCT on ophthalmology field is still not approved by FDA. The development of SDOCT is more attractive from the commercial perspective. In addition, the phase stability achieved by SDOCT is much higher than that of SSOCT, which enable SDOCT to achieve more accurate results on micro-motion detection. In this thesis, our work is focused onto the development of SDOCT technology.

The development of Single camera PhS-OCT system include the selection of hardware (optical components and electronic devices), optical design and software control for data acquiring and processing.

3.3.2 Light source

3.3.2.1 General Source Criteria

Four primary considerations for evaluating optical sources for OCT imaging are wavelength, bandwidth, single-transverse-mode power, and stability. In general, OCT imaging depth of penetration is limited by both absorption and scattering. Both of these sources of attenuation are wavelength-dependent. The red end of the visible spectrum is known as the therapeutic or diagnostic window, because it is the location of a relative minimum in the absorption of typical tissue constituents such as water and blood. Scattering, however, presents a nearly monotonic decrease with increasing wavelength over the visible and near-infrared spectral region. Maximizing OCT imaging depth of penetration therefore requires the use of a centre wavelength that balances these two influences. Theoretical treatments and investigations of tissue optical properties suggest that optimal image depth of penetration should occur near 1.3μm and near 1.65μm.

Axial resolution in OCT imaging is determined by the bandwidth of the light source through Eq. 2.9. For a given source wavelength, an increase in bandwidth gives rise to a proportional increase in resolution.

Spatially incoherent sources are difficult to use for OCT because the signal that is detected arises from interference between light returning from the sample and light returning from the interferometer reference arm. Unless both the sample and reference electric fields are returned to the detector with identical wave fronts, the interference will be washed out upon integration. In typical interferometers, the wave front transformations of the two pathways are not identical. When a single-transverse-mode source is used, spatial filters can be employed to remove any light that is scattered from the lowest order mode into higher order modes and thus preserve interference fringe contrast. High power could enhance the sensitivity for detecting the weak back scattering signal from deeper area.

A final general criterion for evaluating optical sources for OCT is suitability to the application environment. Early studies demonstrating OCT imaging were performed in the laboratory, where the complexity of the system or source is not a critical issue. Many studies are now moving toward in situ and even in vivo imaging, for which a simple, compact, and robust system is essential. Unfortunately, the best sources in terms of resolution and image acquisition rate (femtosecond solid-state lasers) are the worst in terms of complexity, size, and environmental stability. Femtosecond lasers can already provide resolution near 1µm and are available at several near-infrared wavelengths; the most exciting future advancements for OCT sources are likely to be reductions in the size, cost, and complexity of these sources.

3.3.2.2 Light source for PhS-OCT system

There are some common used commercial light source for OCT, such as Super Luminescent Diode (SLD), femtosecond laser and thermal tungsten halogen. Compared to other light source, femtosecond laser is expensive and the high power could bring high level shot noise. Thermal tungsten halogen sources usually have insufficient power to achieve good image depth of bio-tissues and cooling system is required when in operation. Also considering experiments requirements and cost, SLD was adapted for the system development.

DL-BX9-CS3159A SLD light source from DenseLight Semiconductors Pte Ltd was adapted. This light source has a central wavelength of 1310 nm and a full width at half maximum (FWHM) bandwidth of 83 nm. The maximum ex-fiber output power was rated at ~ 15 mW. The Physical dimensions and mechanical specification is shown in Table 3.1 and figure 3.4

Table 3.1 Physical dimensions and mechanical specification

Dimension	L100 x W80 x H16 mm
Enclosure	Metal Case
Optical output	1 m SMF-28 fiber, 900um loose tube with FC/APC
Cooling	Air-cooled
Electronic interface	10-way single row HE14 shrouded header

3.3.3 High-speed spectrometer

The detection unit is high speed spectrometer which consisted of a transmission grating and line scan CCD camera. The spectrum can be calculated from the captured data by using the coefficient from the known light source and optical components.

3.3.3.1 Diffraction Grating

An optical diffracting grating is an optical component with a periodic structure, which splits and diffracts light into several beams travelling in different directions. It can be manufactured by engraving regular ridges or rulings on glass or metal surface. The relationship between the grating spacing and the angles of the incident and diffracted beams of light is known as the grating equation.

$$d(\sin\theta_i + \sin\theta_d) = m\lambda \quad m = 0, \pm1, \pm2 \cdots \tag{3.13}$$

Where d is the distance from the centre of one slit to the centre of the adjacent slit, θ_i is incident angle and θ_d is the diffraction angle. From Eq. 3.13 it is obviously that for a given grating, when a complex light irradiation, dispersion will happened for different wavelengths of light components beside the zero-order. An example is shown in figure 3.4.

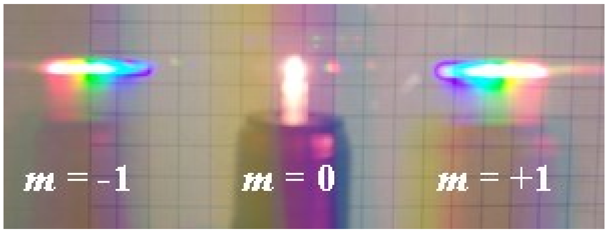

Figure 3.4 A light bulb of a flashlight seen through a transmissive grating, showing three diffracted orders. The order m = 0 corresponds to a direct transmission of light through the grating. In the first positive order (m = +1), colors with increasing wavelengths (from blue to red) are diffracted at increasing angles.[114]

1145 l/mm @ 1310nm Dickson® Diffraction Grating [115] from Wasatch Photonics was employed for the development of PhS-OCT system. These high-efficiency grating works well in the NIR spectrum region around 1310 nm. They are created by using coherent laser light to write the interference pattern in dichromated gelatin. After processing, the grating is capped with a protective glass cover and then AR coated. The results are a grating with low scatter, high diffraction efficiency and low wave front distortion. The grating is durable and can be cleaned using the same methods to clean AR coated optics. These gratings are available in 25.4 mm and 50.8 mm diameter sizes. The transmission geometry of grating is shown in figure 3.5.

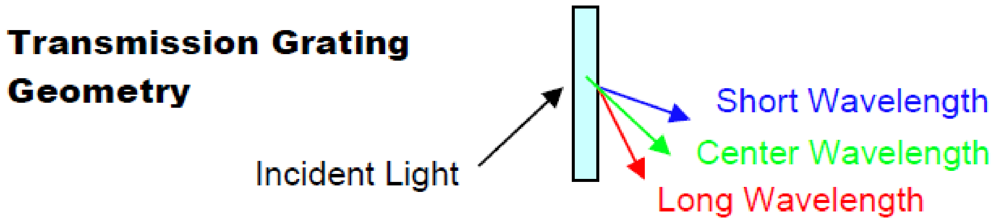
Transmission Grating Geometry
Incident Light
Short Wavelength
Center Wavelength
Long Wavelength

Figure 3.5 Transmission grating geometry

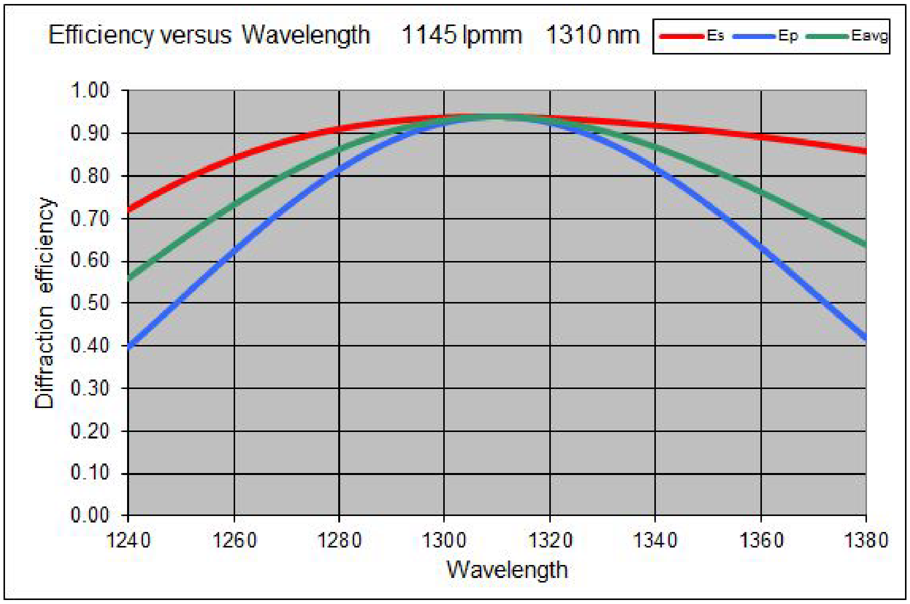

Figure 3.6 Grating characteristic curve of diffraction efficiency versus wavelength

Figure 3.6 shows the diffraction efficiency of grating at different wavelength. Red curve and blue curve are the diffraction efficiency for different polarization status, and green curve represents the average diffraction efficiency. It can be observed from the curve that at the central wavelength of 1310 nm the average diffraction efficiency is as high as 93%.

Table 3.2 Specifications of Grating

General	
Surface quality	60-40 scratch-dig
Diffracted wavefront	< λ.5 rms @632.8 nm
Spatial Frequency	1145 l/mm +/- 0.5 l/mm
CWL	1310nm
Angle of incidence (AOI)	48.6 @1310nm
Thickness Tolerance	+/- 0.25
Diameter Tolerance	+0/-0.15
Chamfers	0.25-0.75 mm face width
Chamfers Angle/Tolerance	45 +/- 15
AR Coating	< 0.5% Reflection; 1240nm- 1380nm
25.4 mm gratings	
Substrate and Cover Glass	1.55 mm BK7 3 mm total thickness
Clear Aperture	20mm
Dimensions	A = 25.4 mm B = 3mm

3.3.3.2 CCD camera

Indium Gallium Arsenide (InGaAs) semiconductors have optimized responsively in the near IR wavelengths (1000 - 1600nm) Yun, et. al. [116] published work on the development of a 1310 nm SDOCT system using a high-speed InGaAs line scan CCD. SU1024-LDH2 92KHz InGaAs line-scan camera (SUI, Goodrich Corp, NJ, USA) was employed for the system build up. This camera is a 2nd generation high-speed 1024 pixel lines-can InGaAs camera that increases the A-line rate to 91,911 lines per second. This enables spectral-domain optical coherence tomography (SD-OCT) at 1.04 μm to capture detailed 3-D volumes of the retina, nerve head and choroid layer in a blink of the eye. For 1.31 μm SD-OCT, diode array based OCT systems offer superior phase stability for Doppler or Polarization-Sensitive OCT. The LDH2 provides 12-bit digital capture into base-format Camera Link® interface cards, while providing maximum dynamic range up over 2300:1 for high line rates. Two pixel apertures are available: 500-μm tall pixels for easy alignment in SD-OCT systems, or 25-μm square pixels for ultra-fast machine vision or dual-camera PS-OCT.

SDR 26-pin connector is used for the control and image data transport with base camera link cable. Two SMA connectors are employed for Sync output and trigger input respectively. LED light with three different colors is adapted to indicate the working status of camera. The main features of SU1024-LDH2 is shown at Table 3.3

Table 3.3 Features of SU1024-LDH2 [117]

91,911 A-line rate per second for 1024 pixels at 12 bits
Integrate-while-read snapshot acquisition
Wavelength response over 0.8 μm to 1.7 μm with flat QE for 1.05 and 1.31 μm OCT
25 μm pixel pitch with aperture heights of 25 μm (defined by on-chip mask) or 500 μm
12-bit base Camera Link® compatible output and control
High quantum efficiency and dynamic range
Operating temperature range of -10 to +50°C
Mounts easily to spectrometers due to 5.7 mm image plane depth and O-ring light seal
Mounts easily to optics benches or MV system switch tripod, front or side fastener hole patterns
Optional adapters for F-mount or C-mount, lenses (C-mount lenses may not fully illuminate the full width of the 25.6 mm wide arrays)

3.3.4 System design

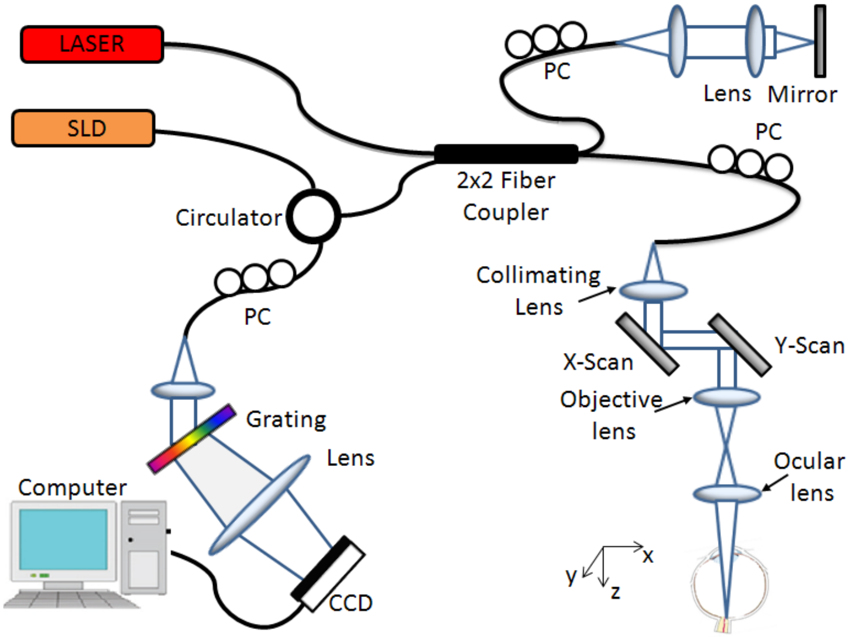
LASER
SLD
PC
Lens
Mirror
PC
2x2 Fiber Coupler
Circulator
Collimating Lens
PC
Y-Scan
X-Scan
Objective lens
Grating
Lens
Ocular lens
Computer
CCD
x
y
z

Figure 3.7 Typical schematic of the one camera PhS-OCT system: SLD – super luminescent diode, PC – polarization controller, Laser- pilot laser for beam guiding, CCD – line-scan camera.

The single camera PhS-OCT system used to study the micro-motion is shown in Figure 3.7. This system employed a broadband infrared Superluminescent Diode (SLD, Denselight Ltd, Singapore) with a 1310 nm central wavelength and a full width at half maximum (FWHM) bandwidth of 83 nm as the illuminating light source. The maximum ex-fiber output power was rated at ~ 15 mW. Most of the optic components were bought from Thorlabs.

The light from the SLD was split into two paths by a 10:90 fiber coupler (FC1310-70-10-APC). The ninety percent power goes to the sample arm and focused by an objective lens (AC254-050-C), a Galvo mirror (GVS002) in both x and y directions was adapted to achieve the 3-Dimentional scanning. The lateral resolution was decided by the size of beam spot which is controlled by the collimate lens (F280APC-C) and objective lens, for this setup, it was about 18 μm in air. The axil resolution was about 8.9 μm which is depend on the central wavelength and FWHM of lighter source.

The ten percent power goes to the reference arm. The lights reflected back from both reference and sample arms meet and interfere with each other at the fiber-coupler, and the resulting interferograms emerging at the output of interferometer was sent, via the optical circulator, to a custom-built high-speed spectrometer.

The spectrometer consisted of a transmission grating (1200 lines/mm), a camera lens (AC-508-100-C) with a focal length of 100 mm, and 1024 element line scan infrared InGaAs detector (Goodrich Ltd, USA). The total depth range was measured to be ~2.8 mm in air (2.1 mm in biological tissue by assuming that the refractive index of the sample is ~1.35). The maximal imaging speed of the system was 92,000 A-scans rate, with which the measured signal to noise ratio (SNR) was ~100 dB at the focus spot of the sampling beam, which was ~500 μm below the zero delay line.

The phase sensitivity of current developed PhS-OCT system is mainly depended on the commercial camera in the system, which limits the application of PhS-OCT for micro-motion detection. This thesis propose a useful method to boost the imaging speed for PhS-OCT by multiplying a number of high-speed spectrometers used in the system with selective precise control of data-recording and data-reading phases for spectral cameras employed in each spectrometer.

3.4 Dual camera PhS-OCT system development

To demonstrate the proposed method, two spectrometers built in a 1310 nm-band PhS-OCT system were used, each equipped with a high-speed InGaAs line-scan camera capable of 92-kHz line-scan rate, to achieve an unprecedented imaging speed at 184,000 lines/s.

The schematic of ultrahigh speed dual camera PhS-OCT system was illustrated in Figure3.8. The newly developed system utilized a superluminesent diode as the light source, which could emit 83 nm bandwidth and 1310 nm central wavelength broad band light. With this light source, the system could achieve ~8.9 μm axial resolution, which is the same with single camera PhS-OCT system. The output light was coupled into a fiber-based Mach-Zehnder interferometer through a 20/80 fiber coupler, with 20% delivered to the sample arm and 80% to the reference arm via optical circulators. In the sample arm, the light was coupled into an optical probe, which contains a collimator, objective lens, an ocular lens and a pair of galvanometer scanner. The optical components of the optical probe could achieve ~ 16 μm lateral resolution for the system in biological tissues. Through controlling he input waveforms of the X-Y scanners, the system could achieve difference 2D scanning patterns. In the reference arm, a 20 mm water cell was utilized to compensate the dispersion caused by the water of the human eye. The light back scattered from the sample and reflected from the reference mirror were collected and split into two equal portions via a 50/50 fiber splitter, which was then delivered to two home-built high speed spectrometers separately. Through using the same components (a transmission grating (1200 lines/mm), an achromatic focusing lens (100 mm focal length) and a high speed line scan CMOS camera (Basler, Sprint spL4096-140k).) and careful adjustment, the two spectrometers could deliver almost the same performance for OCT imaging.

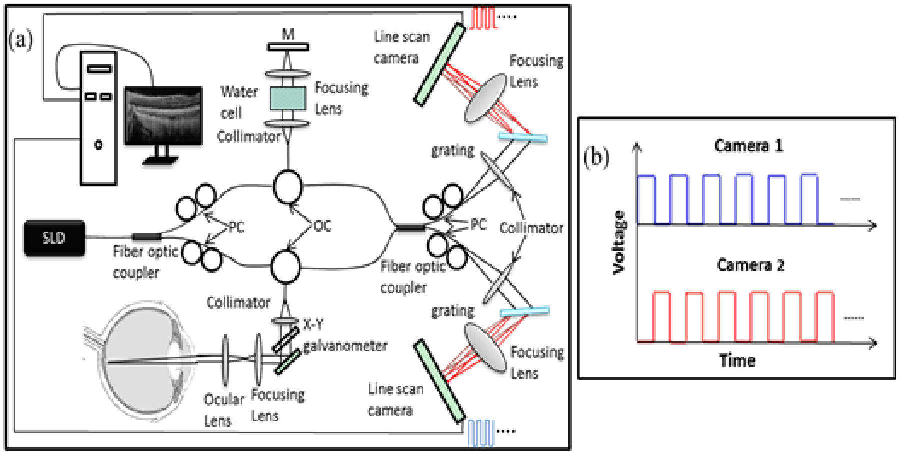
(a)
M
Water cell
Focusing Lens
Collimator
Line scan camera
Focusing Lens
grating
SLD
PC
OC
Fiber optic coupler
PC
Collimator
Fiber optic coupler
Collimator
grating
X-Y galvanometer
Focusing Lens
Ocular Lens
Focusing Lens
Line scan camera
(b)
Camera 1
Camera 2
Voltage
Time

Figure 3.8 Schematic of the ultrahigh speed SDOCT system. (a); and the trigger signal sequences for dual-camera system. SLD: superluminescent diode; PC: polarization controller; OC: optical circulator. (b) trigger-sequences for two cameras

The critical components of the newly developed dual camera PhS-OCT system are two high speed line scan CMOS cameras. Through modify the working pixel number and pixel positions, both of them could work at different imaging speed [118]. The system setup needs sacrifice the spectral resolution through decreasing the working pixel number, the two cameras were sequentially controlled through two carefully designed trigger sequences, which were illustrated in Figure3.8 (b). Considering the balance between the imaging speed, axial resolution and the system detectable depth range, the working pixel number of each camera could be set as 800. When the light with 83 nm bandwidth was illuminated onto the 800 pixels sensor array, the system could achieve ~2.5 mm imaging depth on both sides of the zero-delay line. To generate the trigger sequences, a 250 kHz square wave form (with 50% duty cycle) was first produced as the trigger sequence for the first camera (the blue signal of Figure3.8 (b)). Within one signal cycle, the data recording was triggered when the signal is on in the first half time and data transmission otherwise. Secondly, a reversed trigger sequence to the first one was generated as the trigger signal for the second camera (illustrated in Figure3.8 (b), the red signal). Combining these two signals, the two cameras of the developed system could work continuously to realize 100 percent duty cycle for imaging recording. Compared to the previously reported fastest PhS-OCT system in [118], dual camera PhS-OCT system demonstrated two major advantages. At first, the new developed system could achieve much higher imaging speed of than [118] single PhS-OCT system, which is enabled through sequentially controlling two cameras. Second, the new system utilized more pixels for image recording (800 versus 576), which could enable deeper imaging depth for similar axial resolution.

3.4.1 System evaluation

3.4.1.1 System performance evaluation

To achieve the best performance of the dual-camera system, there is an additional requirement for system configurations, which need the identical performance of the two individual spectrometers. However, it is very hard if not impossible to obtain exactly the same performances for both spectrometers during the alignment process due to the nonidentical performance of the optics components and the aligning errors. In order to achieve the best performance of the proposed system, a digital spectrum reshaping method [119] was utilized.

To test the performance of the digital spectrum reshaping method, a reflecting mirror was placed in the sample arm and the reference mirror was placed at 0.5 mm away from the zero delay line. The interferogram was recorded and the point spread functions before and after applying the digital spectrum reshaping method were calculated for comparison. For further evaluating the performance of the ultrahigh speed SDOCT system, a sensitivity testing experiment was performed. A reflecting mirror was placed on the sample arm. A 40 dB OD filter was installed onto the sample arm to reduce the light reflected from the mirror in the sample arm. The reference mirror was moved from ~0.15 mm to the ~2.4 mm (~0.15 mm interval), which is almost the end the measurable depth range of the system. At each position, the interferogram was recorded and transferred from the wavenumber space to the depth space. The signal to noise ratios (SNR) of the peak at each position plus 40 dB (reduced by the OD filter) would be the sensitivities of the system. The peak positions were recorded as the measured optical delay line. For each peak, full width at half max (FWHM) of was measured as the resolution in air. The calculated results could be used as a demonstration of the system performance.

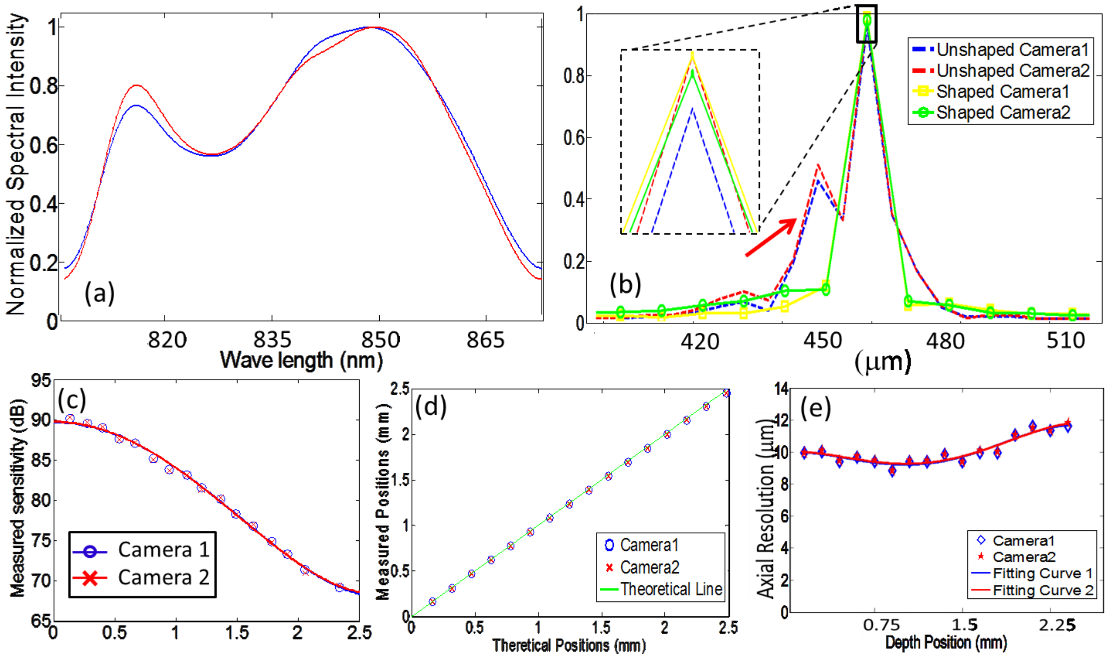

Figure 3.9 System performance of the ultrahigh speed SDOCT. (a), light source spectrums captured by the two cameras of the system; (b) the PSF of the two spectrometers before (red and blue) and after (yellow and green) the digital beam shaping. (c) system sensitivity falling off curve of the two spectrometers. (d) measured optical delay line positions of the two spectrometers. (e) system axial resolution.

The results of the system evaluations experiments are demonstrated in Figure 3.9. Figure 3.9 (a) demonstrates the light source spectrum captured by the two spectrometers used in dual camera PhS-OCT system. The apparent non-Gaussian shaped spectrum will generate sidelobes, which would impair the image quality. Besides, the differences between the spectrums captured by the cameras would generate different modulations to the final system performances. These two effects could be better illustrated by the point spread function (PSF) presented by the blue and red curves in Figure 3.9 (b) (normalized to the first camera, the red curve), where the red arrow points out the side lobes and the zoomed in view (marked by the black dash square) presents the non-equal effect between the system sensitivity achieved by two spectrometers. After applying the digital spectrum reshaping method [119], the effects coming from the spectrum captured by the home-built spectrometers could be minimized. In Figure 3.9 (b), the yellow and green curves are the PSF after the spectrum re-shaping (normalized to the first camera the yellow curve). As presented in Figure 3.9 (b), the sidelobes of the yellow and green curves were sufficiently minimized compared to the red and blue curves. In addition, the differences between the SPF of two cameras were greatly compressed after the spectrum reshaping. As illustrated in Figure 3.9 (b) (the black square and it zoomed black dash square), the difference between the green and yellow curve are much smaller compared to the difference between the red and blue curves. After reshaping, the PSF of two cameras are almost exactly the same except the noise region. Figure 3.9 (c), (d) and (e) demonstrate measured system falling off curve, optical delay lines and axial resolutions of the two spectrometers. As we can see, the two individual spectrometers have almost the same performance under the control of the trigger sequences discussed above. Both of them achieve ~90 dB around the zero-delay line and ~83 dB at 1.2 mm imaging depth position (presented in Figure 3.9 (c)). The measured and fitting sensitivity falling off curves of both cameras are almost exactly the same. As to the measured peak position, both of them could provide the same information about the imaging depth, as illustrated in Figure 3.9 (d). The measured depth results (the circle and cross) are accurately matched with the real setting positions (the green line). Figure 3.9 (e) demonstrated the resolution performances of both spectrometers. The blue diamond and red star are measured system axial resolutions at different depth of camera 1 and camera 2 respectively. The blue and red curves are the corresponding fitting curves. Both spectrometers achieved less 10 μm axial resolution above 1.8 mm imaging depth and ~ 12 μm at deeper imaging depth.

3.4.1.2 Phantom experiment

To demonstrate the proposed system capable of a 184-kHz line-scan rate by employing dual 92-kHz spectrometers, it elected to image a purpose-made flow phantom to assess the system on two aspects: microstructure imaging and flow imaging using phase-resolved measurement. Because it is known that if under the condition of 184-kHz line-scan rate, the phase differences assessed between two adjacent A-lines must be half that when the system runs at 92 kHz by the use of the triggering protocol described above. To make the flow phantom, an inner diameter of a ~250 μm plastic tube was buried within a tissue phantom made by mixing the gelatin with 2% milk. A ~1% intralipid water solution was driven to flow in the plastic tube by a precision syringe pump. In the experiment, the system captured 1000 A-lines to form one B-scan covering ~1 mm. With the triggering protocol described above, 500 odd-numbered A-lines were captured by the first camera and the other 500 A-lines by the second camera.

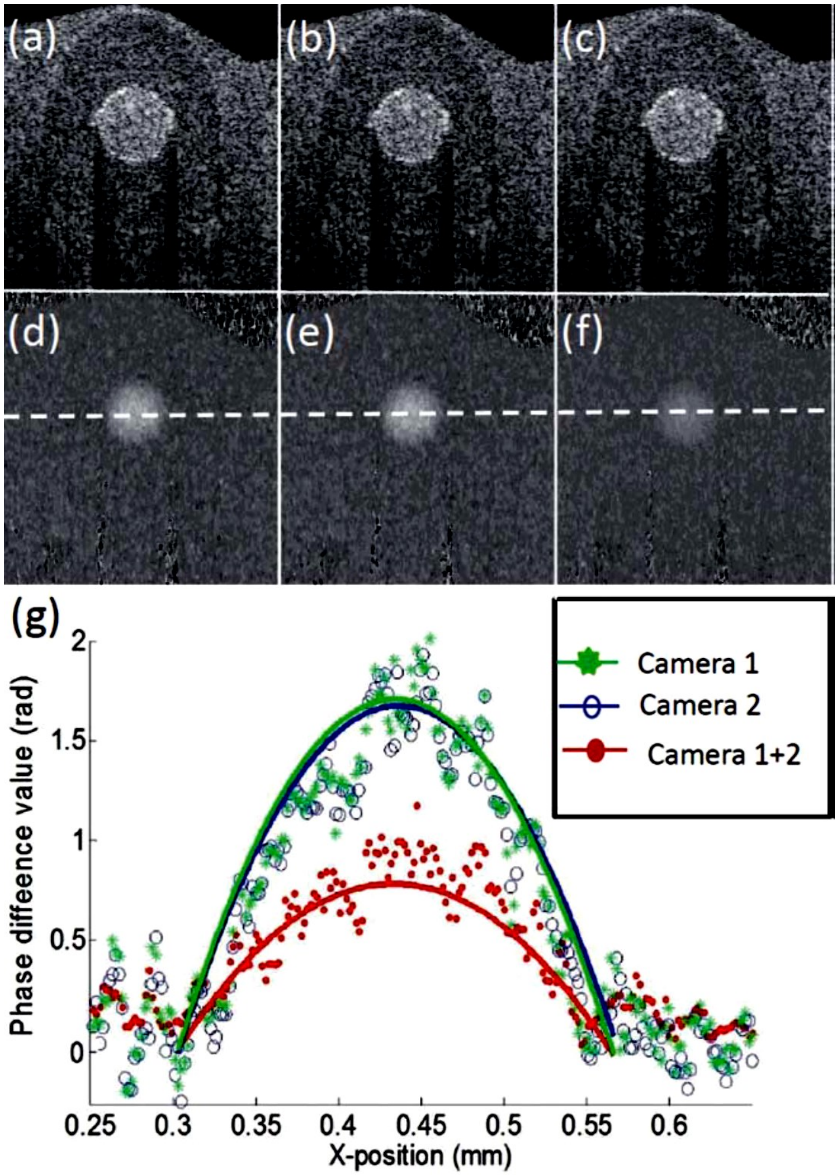

Figure 3.10 Cross-sectional structure and phase-difference images obtained from the flow phantom experiments. (a) and (b) single camera PhS-OCT structural images resulting from the first and second spectrometers, respectively. (c) Structural image from the dual-camera PhS-OCT system. (d), (e) and (f) Corresponding PhS-OCT phase difference maps evaluated from the system employing the first, second, and dual-spectrometers, respectively. (g) Phase-difference plot along the dashed line (see middle images), passing through the center of the flow-tube. The solid curves are the parabolic fitting to the measured data.

The results are shown in Figure 3.10, where (a) and (b) are the cross-sectional microstructure images obtained from the first and second spectrometers, respectively, while (c) is from the combined system but twice the imaging speed. Due to the same performance of the spectrometers used, the image qualities from the individual and combined spectrometers are almost identical to each other as expected, both in system sensitivity and imaging depth. Next the PhS-OCT algorithm was applied to obtain phase difference maps of the flow to verify the system sampling rate. Figure 3.10 (d) shows the phase difference map obtained from the data captured by the first camera, while Figure 3.10 (e) is from the second camera. Because of the identical performance of two spectrometers, the phase difference values within the flow regions are without visible difference between the two, both giving an average flow velocity of 5.68 mm/s after converting the phases into the velocities, agreeing well with the pre-set value (5.8 mm/s, Doppler angle corrected) at the pump. Figure 3.10 (f) gives the phase-difference map obtained from the merged dataset from the first and second spectrometers. Compared to Figs. 3.10 (d) and (e), the phase values in Figure 3.10 (f) are halved due to being twice the A-line rate, however, the evaluated average flow velocity (5.66 mm/s) is about the same as that of the single spectrometer. The phase values can be better illustrated in Figure 3.10 (g) by plotting them along the dashed line passing through the tube center. It is clear that the phase-difference values at the flow region are statistically the same for the first and second spectrometers. However, these values are twice as high as those from the dual-spectrometers. These results demonstrate that the dual-spectrometer system doubled the sampling rate of the single-spectrometer system.

It has demonstrated the 184-kHz line-scan rate for a dual-spectrometer system working at 1310 nm band. The concept can be extended to include more spectrometers in a PhS-OCT system, including that at other wavelength bands, to further increase the imaging speed. With a speed of 184 kHz as demonstrated here, a 3D imaging cube of 512×512×512 pixels can be acquired within ~0.7 s, important for in vivo imaging applications where the subject movement is inevitable. With such high speed, multiple advantages can be envisioned for in vivo imaging. For example, high speed makes rapid survey of large tissue volumes possible as well as increasing the imaging throughput. In addition, high speed also allows for multi-frame averaging or acquisition of high-pixel-density images, which can be used to improve image quality or reduce speckle. However, the price that has to be paid for the proposed approach is the increased cost of the likely system, which may become a main factor limiting its clinical applications.

3.5 Conclusion

Compared with traditional DOCT and PRDOCT, PhS-OCT have higher sensitivity for phase change that can be used in this thesis for micro-motion detection. This thesis have proposed a useful method to boost the imaging speed of a single camera PhS-OCT system, in which multiple spectrometers can be employed to multiply the system line-scan rate by precise timing control of the reading and recording phases in the cameras. It has demonstrated the concept by use of a dual-spectrometer that employed the state-of-the-art InGaAs line-scan cameras to achieve an unprecedented imaging speed of 184,000 lines per second at the 1310-nm wavelength band. However, only single camera PhS-OCT system was used for further researches and studies as presented in the following chapters. It is because the spectrometer in an OCT system is the main cost in system building up. Dual camera system will increase the system cost by ~ 50% which is with low cost performance. The scanning speed (92KHz) for single camera PhS-OCT is enough for the study in following chapters, thus this thesis mainly focused on the development of single camera PhS-OCT system and its applications.

Chapter 4 Photothermal OCT

4.1 Introduction

In this chapter, photo-thermal OCT (PT-OCT) is presented as one of the application of PhS-OCT for micro-motion detection. The background and theory PT-OCT is introduced. Detailed system set-up, data acquisition and processing algorisms are fully demonstrated. The system contains an 808nm pump laser, which excites the photothermal compound, and the PT system detects the changes in the optical path length of the sample induced by the temperature increase.

A model that describes the optical path length (OPL) change due to the increase of temperature from a photothermal compound is provided. The study demonstrates experimentally the phase (and OPL) accumulation as a function of depth in homogeneous solid gel phantoms, and uses the experimental results to determine the model coefficients. Finally the model by reconstructing the photothermal drug concentration in single and double layer solid gel phantoms are validated. This study is the first demonstration of using a PT-OCT model to reconstruct optically absorbing compound concentrations as a function of depth. The model is used in thick samples and high resolution images are obtained.

In chapter 4 an overview of PT-OCT is provided as one of the application of PhS-OCT combine micro-motion. The background, detailed system set-up, data acquisition and processing algorisms of PT-OCT are fully demonstrated. This study is the first demonstration of using a PT-OCT model to reconstruct optically absorbing compound concentrations as a function of depth.

4.2 Background of photothermal (PT) phenomena

Photothermal (PT) response is generated by heating of a sample due to absorption of electromagnetic radiation in a short pulse or continuous train of pulses [120]. Absorption of pulsed laser radiation in a sample generates PT effects including a temperature increase, refractive index change, and thermoelastic surface displacement [120]. Detection of PT effects and associated signal processing have been applied in many areas including photoacoustic spectroscopy, nondestructive evaluation and thermal property determination [121].

The detection of laser-induced optical path length change and thermal expansion, as a photothermal effect, may aid tissue diagnostics in biomedical applications such as imaging [122] and sensing [123]. Optical path length changes in tissue in response to absorption of pulsed laser light result from refractive index change [124]. Thermal expansion as well as refractive index change results in a transient optical path length variation in laser-heated tissue [124]. Spatial variation of refractive index is a fundamental optical property of tissue and can provide useful and critical information about structure and physiological function. Because water and protein are primary constituents of all living systems, the relevant optical and thermal properties are of interest in investigating optical effects in tissue. Fortunately, national and international standards organizations have invested substantial resources in characterizing the thermophysical properties of water. For proteins, substantially less data is available relating to refractive index and variation with temperature and pressure. The dependence of water refractive index on temperature has been measured [125-127] and a formulation for the refractive index of water in the temperature range of -10 to 500°C was published over the wavelength range of 0.2 to 2.5 μm [127]. The formulation was based on data collected by Thormählen *et al.*[128]. Most published data relates to refractive index of water in the visible wavelength range. Direct measurement of water refractive index in the near infrared (NIR) is complicated by thermal effects induced by absorption of the probing radiation [125]. For refractive index change in the IR, studies using interferometers, including Fabry-Perot, Mach-Zehnder configurations, have produced the most accurate data [126]. Richerzhagen used a single Michelson interferometer to measure refractive index of liquid water. In these experiments, water in a thermally isolated cell is maintained at a constant temperature by external circulation which allows direct refractive index measurement without knowledge of thermal expansion [126]. Water refractive index was measured by displacing a mirror positioned inside the water cell [126]. For thermal expansion measurement, Takenaka and Masui measured thermal expansion of pure water by the dilatometric method in a temperature range from 0 to 85°C [129]. However, the dilatometer requires a mercury bulb which is connected to the water cell covered by a thermostat. Therefore, a non-invasive optical interferometric technique to measure both refractive index change and thermal expansion with higher sensitivity may be useful.

Optical Coherence Tomography (OCT) was introduced as a technique to record a cross-sectional image of subsurface tissue structure with micron-scale resolution [17]. Conventional OCT has been used as a promising diagnostic modality for imaging a variety of tissues and detecting tissue structures [130, 131]. However, photothermal response requires a relative strain or stress change measurement related to light absorption by specific tissue chromophores. Correspondingly, detection of laser-induced thermoelastic displacement requires measurement of relative displacement between two points in a sample to deduce optical path length change due to thermal expansion [132].

Non-invasive measurements of the concentration distributions of endogenous (i.e. oxyhemoglobin and deoxyhemoglobin) and exogenous (i.e. chemotherapy and photodynamic therapy) agents in biological tissues may have implications in diagnosing, monitoring and treating several diseases, such as cancer [133, 134]. Several methods have previously been used to determine non-invasively the drug concentration inside biological tissues. These methods include fluorescence [135-138], reflectance spectroscopy [139, 140] and optical coherence tomography (OCT) [141, 142].

PhS-OCT is a variation of the OCT system, which allows the detection of OPL changes that are smaller than a wavelength of light. Optically absorbing drugs can absorb light energy from an excitation laser, and convert it into heat. This phenomenon is known as a photothermal effect. The increase in temperature by the drug will change the index of refraction of the surrounding tissue and induce thermal expansion; which changes the OPL of light. Photothermal OCT (PT-OCT) is a new system that combines a PhS-OCT with a pump-laser. The pump laser light heats the optically absorbing agent and the PhS-OCT detects the OPL changes. The OPL changes on biological tissues will depend on the concentration of the optically absorbing drug. PT-OCT has previously been used in different configurations such as low coherence interferometry [132], using a swept-source PhS-OCT beam [143], using two pump laser wavelengths [144] or having a pump laser located on the opposite side as the PhS-OCT beam[144, 145]. Illuminating the sample from the opposite side of the PhS-OCT beam limits the thickness of the sample for which images can be obtained.

Most PT-OCT experiments have been carried out in liquid phantoms such as dyes [146], hemoglobin [144], and nanoparticles [143]. It is difficult to obtain an accurate phase signal within a liquid due to the Brownian motion of the scattering centres. Therefore, these techniques have been limited to measuring the phase signal at the interface of the liquid. Models for the increase in temperature due to the pump laser have previously been derived [143, 146]; however, experimental measurements of the temperature change have been challenging to obtain at different depths. Measurement of the average temperature change of a whole tissue volume has been previously obtained experimentally [147]. Applications of PT-OCT include obtaining phase signal in *ex vivo* human breast tissues using gold nanoshells [148], obtaining images for targeted molecules in cell cultures [149], determining the concentration of nanoparticles inside sentinel lymph nodes based on a calibration phantom [150], and estimating the concentration of nanorose in thin samples of rabbit arteries [145].

4.3 Materials and methods

4.3.1 Photothermal optical coherence tomography system

Figure 4.1 shows a PT-OCT system that consists of a pump laser integrated with a PhS-OCT system has been designed. The PhS-OCT is single camera system demonstrated in chapter 3. The sample arm of the system is coupled with an 808nm pump laser, which was collimated by a telescopic system, via a dichroic mirror. The pump laser was modulated with a square wave signal generator and a 50% duty cycle. A lateral resolution of ~16μm for the 1310nm laser is achieved by using a 50mm focal length objective lens. The beam size of the pump laser was reshaped by using telescopic lenses and an iris. A one dimensional micropositioning stage was adopted to move the sample in one direction to obtain a cross-sectional image.

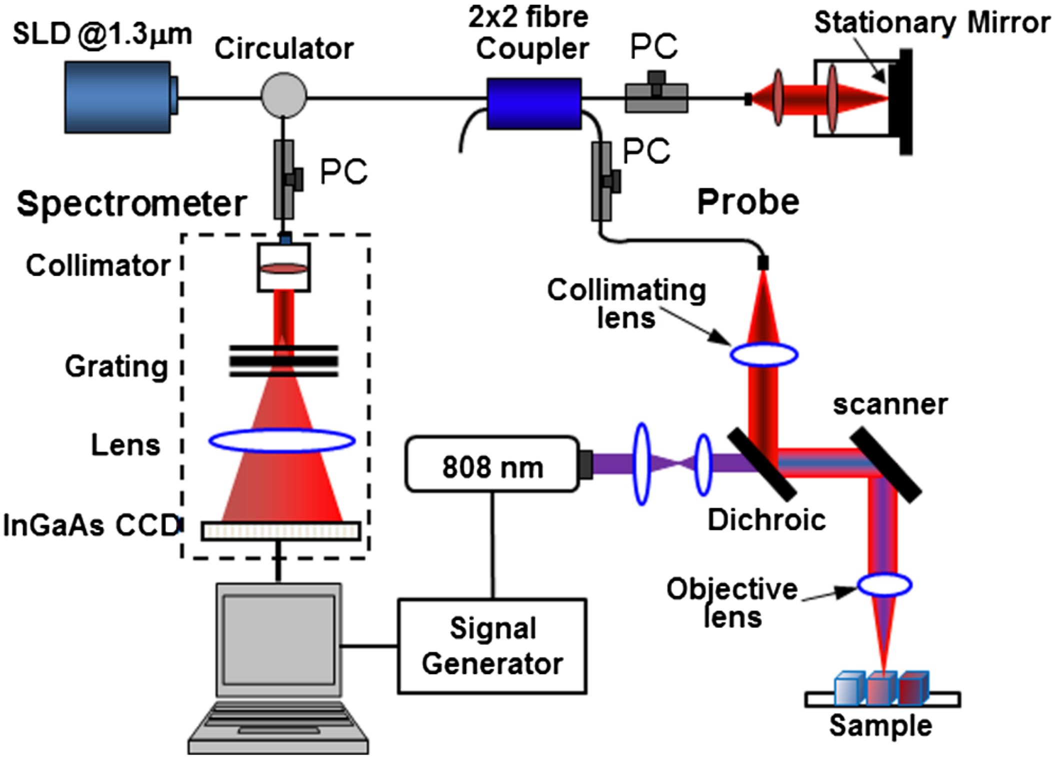
SLD @1.3µm
Circulator
2x2 fibre Coupler
PC
Stationary Mirror
PC
PC
Spectrometer
Probe
Collimator
Collimating lens
Grating
scanner
Lens
808 nm
Dichroic
InGaAs CCD
Objective lens
Signal Generator
Sample

Figure 4.1 Schematic illustration of photothermal OCT

4.3.2 Phantom preparation

Solid gel tissue phantoms that absorb and scatter light were produced to simulate biological tissues. The phantoms contained water and agar (Fisher Scientific) at a concentration of 2 grams/100ml to produce a solid gel. Agar is known to have very low scattering and absorption properties. Milk [151, 152] was used to provide a scattering background, and black India ink [151, 153, 154] (Bombay Black™, Dr. Ph. Martin's) was used to control the absorption properties of the phantom. When the India ink absorbs light its temperature increases, known as a photothermal effect. The wavelength dependent extinction coefficient of India ink was measured using a spectrophotometer, and its absorption spectrum, normalized at 808nm, is shown in Figure 4.3 (a).

Solid phantoms were created by heating the agar and water solution in a microwave for 1 minute. Then, milk and ink were added at the appropriate concentrations, and the liquid was poured in a mold that produced phantoms with a 1mm thickness. The bottom of the phantom was in contact with a glass slide and the top of the phantom was in contact with a glass cover which has a thickness of ~225µm. The phantom solidified within a few minutes.

Double layer phantoms were created in two steps. First, the bottom layer was created as previously described for the single layer phantom, but instead of using a glass cover on the top surface, a plastic film which has a thickness of ~40µm was used. Then, the top layer phantom was prepared by heating the agar and water solution in the microwave for 1 minute and then mixing in the milk and ink at the appropriate concentrations. The solution was poured over the saran wrap after the bottom layer had solidified, and a mold was used to produce a layer with a thickness of ~225µm. The top layer solidified within a few minutes and the top surface was bound by a glass cover. The glass cover placed on the top of the phantom was used as a mold to produce a flat top surface. The cover also prevented evaporated water from escaping and drying the phantom while it was heated by the pump laser. Although the phantoms were bounded on the top and bottom, they were not bounded on the sides.

For the double layer phantoms, a plastic film was placed in between the layers. This plastic film was used to avoid ink diffusion between both layers. The plastic film attenuated the laser light by less than 10%, which was considered acceptable for this study.

4.3.3 Data acquisition and processing

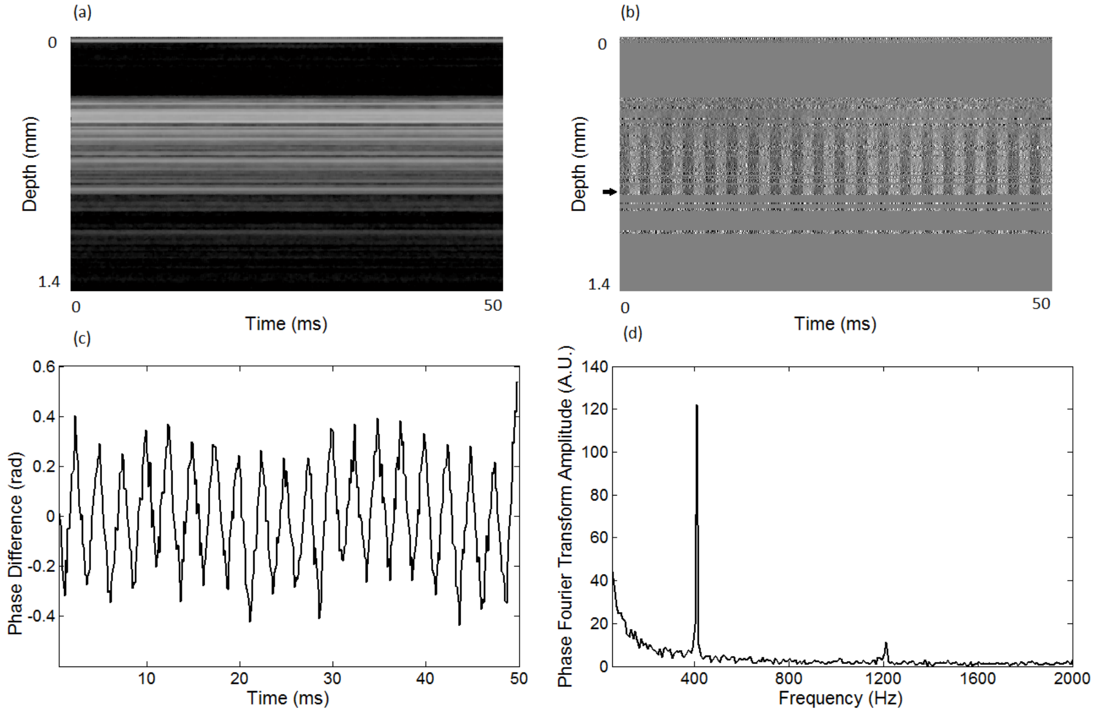

Figure 4.2 (a) M-scan structure image from a phantom that has a 1.5% concentration of India ink. (b) M-scan of the phase difference obtained from the phantom. (c) Phase difference as a function of time at a depth of 530µm below the tissue surface (arrow in (b)). (d) Absolute value of the Fourier transform of the phase difference (c).

Photothermal images were obtained by modulating the pump laser at 400Hz with a square wave (50% duty cycle), and obtaining 1000 A-scans from the same location (also known as an M-Scan) at a frequency of 8.717kHz. It took 115ms to obtain an M-scan. Figure 4.2 (a) shows an example of the OCT structural image of an M-scan obtained from a homogeneous solid gel phantom that contain 1% milk and 1.5% ink. The bright spots identify the location of the scatters in the tissue as a function of depth. It can be noted that the scattering signal remains constant through time as observed by the horizontal lines in the image.

At the depth locations where the scattering signal was greater than a predefined threshold value (10 dB above the noise floor), the phase change between the first and all the other A-scans was calculated within an M-scan set ($\phi_i - \phi_1$), where i is a value between 1 and 1000 and ϕ is the phase of the A-line at a specific depth. We can observe that the phase changes at each depth in Figure 4.2 (b). The image presents two interesting characteristics. First, it can be seen that the dark and light bands through time. These bands have a frequency of 400Hz which is due to the modulation of the pump laser. The second characteristic is that the intensity of the dark and light patches increases through depth. This is due to the phase accumulation which will be discussed in the next section.

Figure 4.2 (c) shows the phase change through time at a depth of 530µm from the tissue surface (the depth location is identified with an arrow in Figure 4.2 (b)). Finally, Figure 4.2 (d) presents the fast-fourier transform of the phase difference ($FFT(\Delta\phi)$). A peak at 400Hz is clearly observed. The amplitude of this peak at each depth, after subtracting the background noise, is used to create the phase image.

4.3.4 Theoretical model

The optical pathlength (OPL) is defined as the product of the geometric length of the path of light undergoing through a system (L) times the index of refraction of the medium through which it propagates (n):

$$OPL(T_0) = \int_0^L n(T_0)dl = n(T_0)L \tag{4.1}$$

Both, the length and the index of refraction are dependent on the temperature of the system (T_0). For the model it assumes that the index of refraction at T_0, is a constant for the whole tissue, for example different tissue layers have the same index of refraction. When there is an increase in temperature (ΔT), as is the case in photothermal systems, the following applies:

$$n(T_0 + \Delta T) = n(T_0) + \frac{dn}{dT}\Delta T \tag{4.2}$$

$$L(T_0 + \Delta T) = (1 + \beta\Delta T)L(T_0) \tag{4.3}$$

where, dn/dT represents the change of the index of refraction with temperature which can be assumed to be constant for a wide range of temperatures [127], and β is the thermal expansion coefficient. The OPL with a temperature increase is given by:

$$OPL(T_0+\Delta T) = \int_0^L \left(n(T_0) + \frac{dn}{dT}\Delta T\right)\cdot(1+\beta\Delta T)\,dl \tag{4.4}$$

The change in temperature is proportional to the absorption coefficient of the dyes, the power of the laser per unit area, the heat capacity and density of the sample, etc. [147, 155] which it has condensed into a coefficient α. The power of the laser decays exponentially as it travels through the medium following a Beer-Lambert expression:

$$\Delta T = \alpha e^{-\mu_t l} \tag{4.5}$$

where μ_t is the extinction coefficient of the medium. The change in optical pathlength (ΔOPL) is then given by:

$$\Delta OPL = OPL(T_0+\Delta T) - OPL(T_0) =$$

$$\int_0^L \left(\left(\frac{dn}{dT} + n(T_0)\beta\right)\alpha e^{-\mu_t l} + \frac{dn}{dT}\beta\alpha^2 e^{-2\mu_t l}\right) dl =$$

$$\left(\frac{dn}{dT} + n(T)\beta\right)\frac{\alpha}{\mu_t}(1-e^{-\mu_t L}) + \frac{dn}{dT}\beta\frac{\alpha^2}{2\mu_t}(1-e^{-2\mu_t L}) \tag{4.6}$$

The phase difference ($\Delta\phi$) relates to the change in optical pathlength and the wavelength of the light (λ_0) by:

$$\Delta\phi = \frac{4\pi\Delta OPL}{\lambda_0} \tag{4.7}$$

The change in the optical pathlength and the amplitude of the FFT of the phase, described in the previous section, are linearly related. Usually, dn/dT and β have values in the order of ~10^{-5} °C^{-1} [143, 146]. Therefore, the second term of Eq. 4.6 is usually much smaller than the first term and can be ignored, leaving us with:

$$\Delta OPL \approx \frac{a'}{\mu_t}(1-e^{-\mu_t L}) \rightarrow FFT(\Delta\phi) \approx \frac{a}{\mu_t}(1-e^{-\mu_t L}) \tag{4.8}$$

where a' is a constant which includes the constants in the first term of Eq. 4.6, and a is a constant related to the amplitude of the FFT of the phase difference which it will refer to as the slope of the curve. For small values of the product of the attenuation coefficient times the pathlength, the equation can be linearized to:

$$\Delta OPL \approx a'L \rightarrow FFT(\Delta\phi) \approx aL \tag{4.9}$$

Eq. 4.9, indicates that the change in the optical pathlength is proportional to the physical length of the medium; which means that the changes increase at deeper tissue structures, which is also described as a phase accumulation. The development of this model assumes that the beam of the pump laser is collimated; however, experimentally the system developed has a focused beam with a large Rayleigh length (~1.28mm).

4.4. Results

4.4.1 Photothermal signal as a function of the absorber concentration

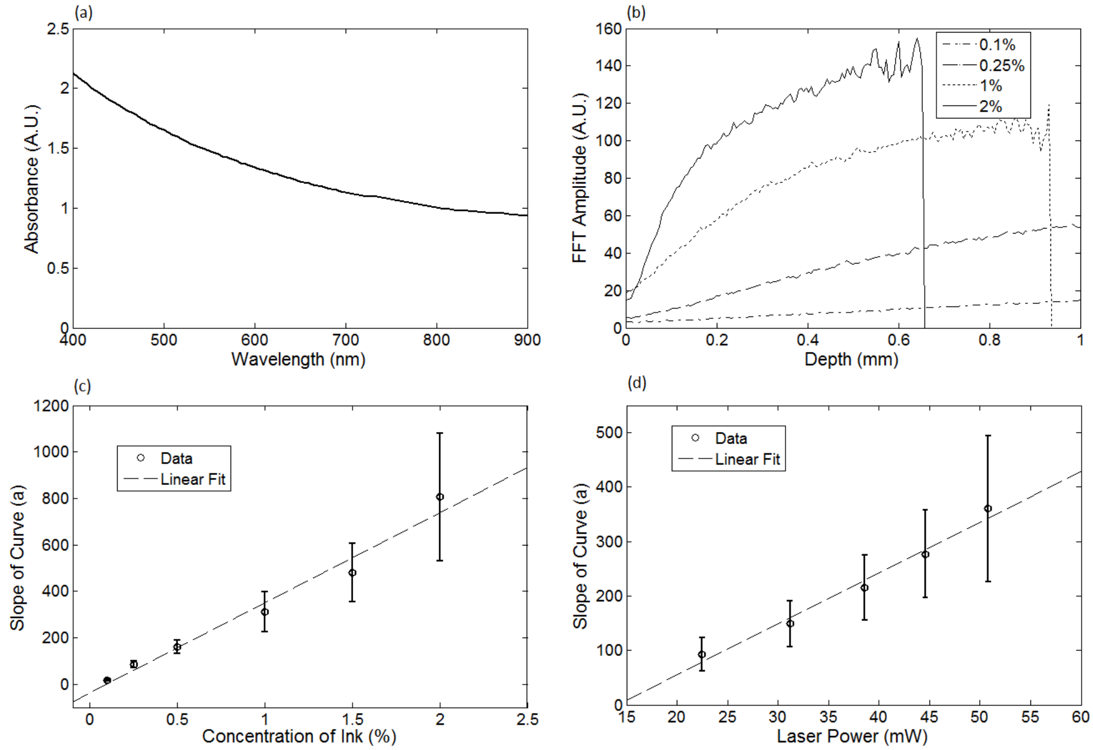

Figure 4.3 (a) Absorption spectra of black India ink normalized at 808nm. (b) FFT amplitude of the phase at different depths for phantoms with different ink concentrations. (c) Mean and standard deviation of the slope of the curve *a* for different ink concentrations with 1% milk and laser power of 50.8mW. (d) Mean and standard deviation of the slope of the curve *a* for different laser powers with 1.5% ink and 1% milk.

To understand the photothermal signal as a function of depth for different absorber concentrations, 6 homogeneous single layer phantoms were created. Each phantom had the same scattering properties and different absorption properties. Milk was added to each phantom at a concentration of 1% to produce a scattering background similar to what is found in biological tissues. India ink was added as the absorber in each phantom at a concentration of 0.1, 0.25, 0.5, 1, 1.5 or 2%. The pump laser had a power of 50.8mW at the sample. For each phantom a B-scan that contained 200 A-lines separated by a distance of 15µm was obtained. The FFT of the phase change was calculated for each M-scan at each depth as previously described, and the amplitude of the FFT was used to obtain a phase image.

The A-lines of the phase image of each phantom were averaged at each depth. Figure 4.3 (b) shows examples of the averaged phase FFT amplitude signal as a function of depth. At higher ink concentrations (which also contain a higher μ_t value) the curve presents an exponential shape; however, for smaller ink concentrations, the shape of the curve is linear. This is expected as described by Eq. 4.8 and 4.9. Also, the higher the attenuation coefficient, the less signal is obtained from deeper tissue structures; which explains why the 1 and 2% ink curves have signal up to a depth of ~0.95 and ~0.65mm, respectively. Each of the 200 individual A-lines from each phantom was fitted to Eq. 4.8 where a and μ_t were fitting parameters. The average and standard deviation of the slope of the curve (a) as a function of the ink concentration is presented in Figure 4.3 (c). A linear dependence is observed for the slope of the curve as a function of the concentration of ink.

4.4.2 Photothermal signal as a function of the laser power

To determine the photothermal signal as a function of the laser power, a homogeneous single layer phantom with 1% milk and 1.5% India ink was prepared. Five B-scans were obtained from the phantom with different laser powers with values of 22.5, 31.2, 38.6, 44.6 and 50.8mW. The laser power was measured using a power meter. Each of the 200 A-lines from each B-scan was fitted to Eq. 4.8. The average and standard deviation of the slope of the curve (a) is presented as a function of the laser power in Figure 4.3 (d). The slope of the curve is linearly dependent on the power of the laser.

4.4.3 Photothermal signal as a function of the distance from the zero-delay line

The model developed assumes that the pump laser beam is collimated; however, in reality it is focused and has a beam waist that varies with the axial position. The PT-OCT system design was optimized to have a large depth of focus (~1.28mm) such that the beam waist would minimally affect the experimental results. Also, the surface of the tissue samples is not always flat, and it is difficult to guarantee that the focal point of the pump laser will always be located at the same position from the tissue surface. Therefore, it is important to design a system that is minimally sensitive to the location of the surface from the zero-delay line, assuming the focal point is maintained at a fixed position.

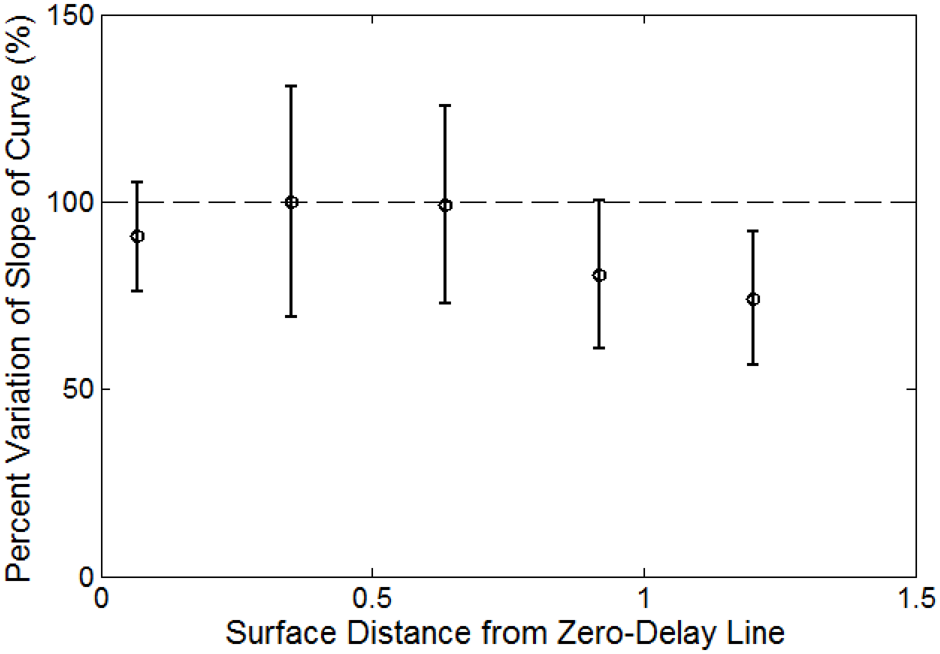

Figure 4.4 Percent variation of the slope of the curve for different distances between the surface of the sample and the zero-delay line normalized to the 350μm distance.

To experimentally validate the large depth of focus, a homogeneous single layer phantom with 1% milk and 1.5% India ink, was used to obtain phase images. The surface of the phantom was placed at a distance of 70, 350, 630, 910 and 1200μm from the zero delay line. The mean and standard deviation of the curve *a* was calculated for each A-line obtained from each phantom location, and normalized to the mean value obtained for the 350μm location. This location was selected because it was the standard for the experiments in this paper. The results are presented in Figure 4.4. For surface distances smaller than ~1mm, the variation of the mean of the slope was less than 25%.

4.4.4 Reconstruction of single and double layer phantoms

Eq. 4.9 is a simplification of the photothermal model that is valid for values of the product of the depth times the attenuation coefficient smaller than 1. The equation states that the photothermal signal is linearly proportional to the depth and the slope of the curve *a*. The slope of the curve is related to the concentration of the ink and the power of the laser, and minimally dependent on the surface distance from the zero-delay line (for a wide range of distances).

To demonstrate the validity of the model, the concentration as a function of depth was reconstructed from single and double layer tissue phantoms. B-scans where obtained from 5 phantoms. Three homogeneous phantoms were created with 1% milk and 0.1, 0.5 and 1.5% India ink. Also, two-double layered phantoms with a top ink concentration of 0.1 and 0.5% and a bottom ink concentration of 0.25% were produced. The pump laser power was 50.8mW.

Each A-line consisted of 512 pixels. Given that in real tissues it will not know a priori the number of tissue layers nor the tissue concentration, a small window of 15 pixels was selected and assumed that the concentration of the drug is constant within that range. This window is large enough to minimize the sensitivity to noise but small enough to produce high resolution. The reconstruction algorithm consisted on fitting a linear equation to 15 consecutive pixels, and determining the slope of the linear fit. Therefore, the slope of pixels 1 through 15 was obtained, and recorded it on pixel 1; then the slope of pixels 2 through 16 was obtained and recorded it in pixel 2; and so on. It was able to ignore the last 15 pixels, since they belong to deep tissue structures where there is almost no signal. Using the linear fit in Figure 4.3 (c) it was able to determine the ink concentration at each pixel based on the slope of the curve. Finally, a median filter was used on the reconstructed concentration image to minimize noise.

The structure, phase and reconstructed concentration images for the single and double layer phantoms are shown in Figure 4.5 and Figure 4.6, respectively. The average of the A-lines in the phase image for the double layer phantom with a top and bottom concentration of 0.5 and 0.25%, respectively; is shown in Figure 4.7. Lines with the slope of the 0.5 and 0.25% phantoms obtained from the single layer phantoms are shown.

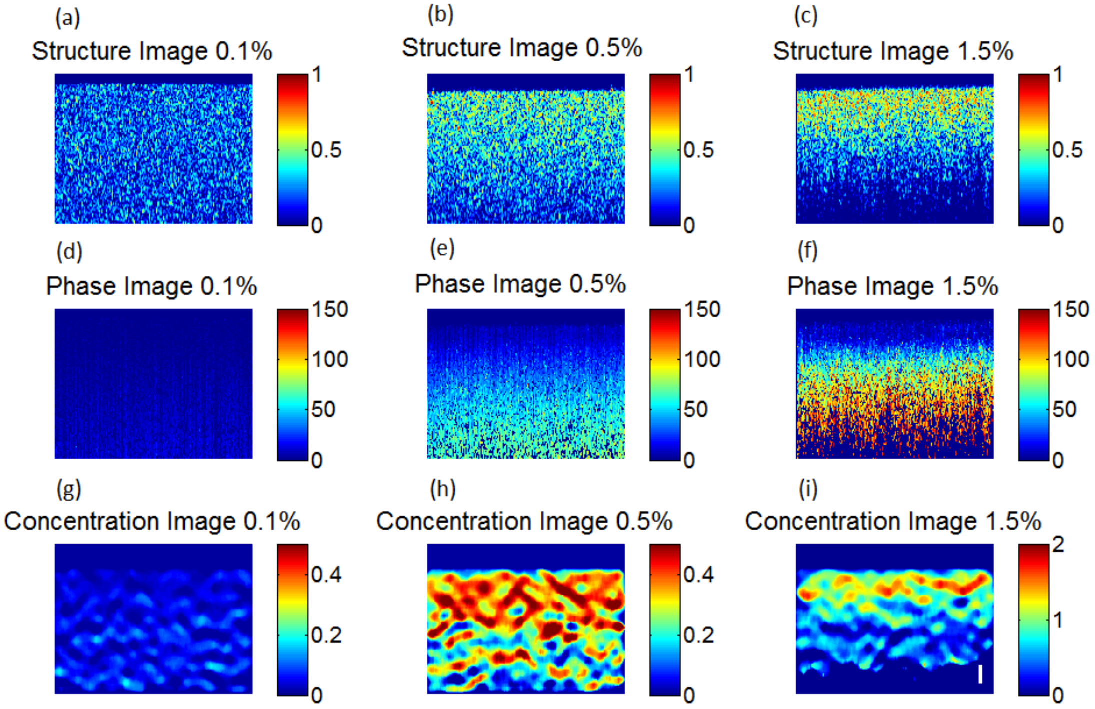
(a)
Structure Image 0.1%
1
0.5
0
(b)
Structure Image 0.5%
1
0.5
0
(c)
Structure Image 1.5%
1
0.5
0
(d)
Phase Image 0.1%
150
100
50
0
(e)
Phase Image 0.5%
150
100
50
0
(f)
Phase Image 1.5%
150
100
50
0
(g)
Concentration Image 0.1%
0.4
0.2
0
(h)
Concentration Image 0.5%
0.4
0.2
0
(i)
Concentration Image 1.5%
2
1
0

Figure 4.5 Structure image for a phantom with an ink concentration of (a) 0.1%, (b) 0.5% and (c) 1.5%. Phase image for a phantom with an ink concentration of (d) 0.1%, (e) 0.5% and (f) 1.5%. Reconstructed concentration image for a phantom with an ink concentration of (g) 0.1%, (h) 0.5% and (i) 1.5%.White line of figure (i): 100μm.

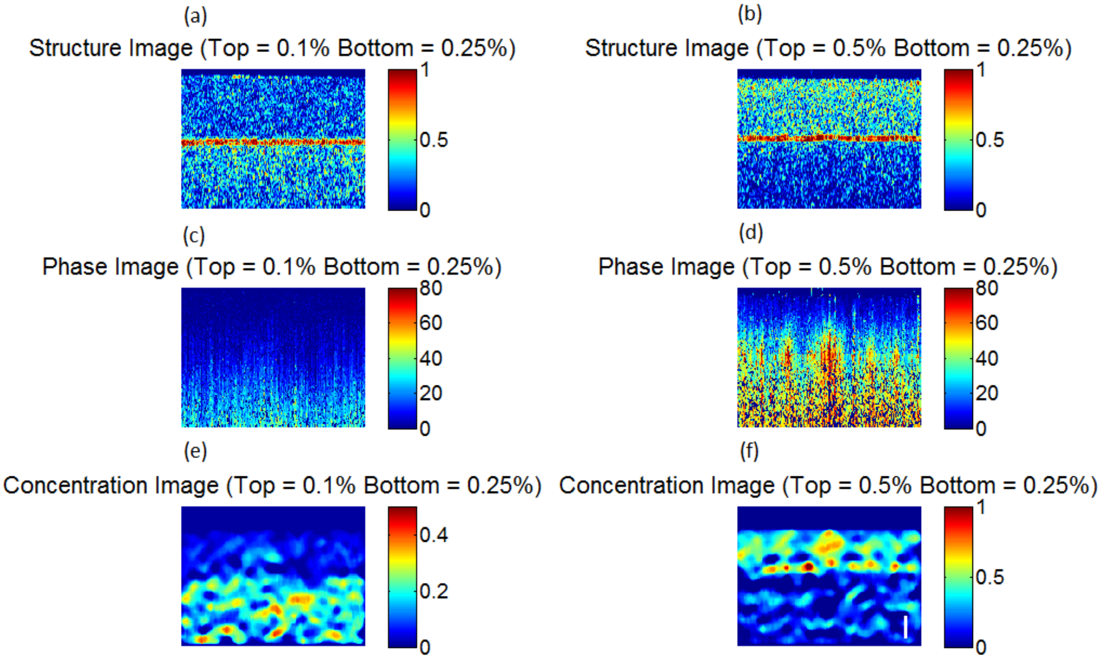
(a)
Structure Image (Top = 0.1% Bottom = 0.25%)
1
0.5
0
(b)
Structure Image (Top = 0.5% Bottom = 0.25%)
1
0.5
0
(c)
Phase Image (Top = 0.1% Bottom = 0.25%)
80
60
40
20
0
(d)
Phase Image (Top = 0.5% Bottom = 0.25%)
80
60
40
20
0
(e)
Concentration Image (Top = 0.1% Bottom = 0.25%)
0.4
0.2
0
(f)
Concentration Image (Top = 0.5% Bottom = 0.25%)
1
0.5
0

Figure 4.6 Structure image for a phantom with a top layer ink concentration of (a) 0.1% and (b) 0.5%. Phase image for a phantom with a top layer ink concentration of (a) 0.1% and (b) 0.5%. Reconstructed concentration image for a phantom with a top layer ink concentration of (a) 0.1% and (b) 0.5%. The bottom layer ink concentration for both phantoms was 0.25%. White line of figure (f): 100µm.

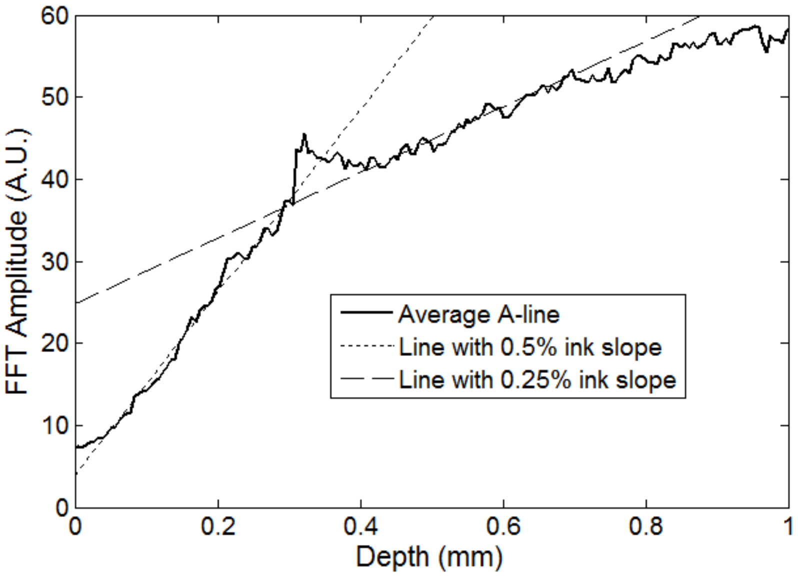

Figure 4.7 Average A-line from the phase image (Figure 6 (d)) for a phantom with a top and bottom layer ink concentration of 0.5 and 0.25%, respectively. The image includes a line with the 0.25 and 0.5% ink slope obtained from the homogeneous phantoms.

4.5 Discussion

Figure 4.3 (b) presents the amplitude of the FFT of the phase changes at different depths in homogeneous single layer phantoms. This figure demonstrates that Eq. 4.8 and Eq. 4.9 are valid description of the shape of the curve. Lower ink concentrations (lower attenuation coefficients) present a linear shape and higher ink concentrations (higher attenuation coefficients) present an exponential curve (linear shape for small depths). Also, as the concentration of the ink increases, the OCT signal is weaker in deeper structures and it limits the depth of the signal acquired. This explains the lack of signal for the 1 and 2% ink concentrations at depth greater than ~0.95 and ~0.65 mm, respectively.

From Figure 4.3 (c) and (d), it is demonstrated that the slope of the curve is linearly proportional to the ink concentration and the power of the laser, respectively. Although the mean values show the linear trend, a large standard deviation is observed at each data point. Large standard deviations of the data was attributed to the lack of stability of the power of the pump laser, which has high intensity fluctuations through time. In future implementations of the system, it expected to minimize these variations by measuring the power of the laser in real-time and properly calibrating the results. Also, although the phantoms prepared were homogeneous, some spots where the dye had accumulated were visually noticeable.

The linear fit obtained in Figure 4.3 (d), for the slope of the curve as a function of the laser power, does not cross the origin. The reason for this is that there needs to be a minimum threshold of laser power for which the increase in temperature by the ink is higher than the heat diffusion from the surrounding medium. Once the threshold is exceeded, the ink will increase its temperature producing changes in the index of refraction and thermal expansion, which can be detected with the PT-OCT system.

Due to the long focal length of the system, the surface of the sample can be located at any distance smaller than ~1mm from the zero-delay line, producing a variation of the slope of the curve of less than 25%. It is important to determine this range because the surface of biological tissues have curvatures (i.e. they are not flat), and it would be difficult to guarantee that the surface will be located at a fixed position from the zero-delay line as a B-scan is obtained. Also, given that the pump laser is focused, the power per unit area varies with depth. For the range of 350 to 630μm, the power per unit area is almost constant for all depths.

From Figure 4.5 it is observed that the ink concentration of homogeneous single layer phantoms can properly be reconstructed. The reconstruction is accurate for low ink concentrations. At higher ink concentrations the reconstruction close to the tissue surface is accurate; however, at deeper locations the concentration decreases. This is expected because the linearity of the phase image is only valid for small values of the product of the attenuation coefficient times the depth, and the inverse reconstruction model only works for the linear regions. Also, at higher ink concentrations there is less signal coming from deeper structures as can be observed in the structure OCT image (Figure 4.5 (c)). The reconstruction algorithm uses Eq. 4.9 instead of Eq. 4.8 because in real tissues it cannot be assumed that the absorber concentration is homogeneous at all depths.

Figure 4.6 shows the concentration image reconstruction from two double layer phantoms were the top ink concentration is higher and lower than the bottom layer ink concentration. Low values of ink concentration (≤ 0.5%) were selected such that the phase image will be linear for large depths. The structure images show the plastic film that separates both layers (red horizontal line on Figure 4.6 (a) and (b)).

If it was known that the concentration within a layer of tissue was constant, the reconstruction algorithm could be modified to find the slope of the curve for the number of pixels within a specified layer. The number of pixels belonging to a layer could be determined by observing the structure image, as shown in Figure 4.6 (a) and (b). However, since it is not possible to know for sure that the concentration is homogeneous within a tissue layer it is imprudent to modify the algorithm.

Ideally, the slope of the curve could be determined by using the gradient between each two consecutive pixels of an A-line from a phase image. However, this approach is highly sensitive to noise. In this method, 15 pixels was chosen because it offered a balance between too few pixels (which are highly sensitive to noise), and too many pixels, which reduce the resolution of the reconstructed concentration image. It is important to note that the slope of the curve (a) as a function of concentration (Figure 4.3 (c)), needs to be determined for each drug that is being used.

Figure 4.7 shows the average of all the A-lines in the phase image from the top and bottom ink concentration of 0.5 and 0.25% (Figure 4.6 (d)). The figure includes two linear curves that have the 0.5 and 0.25% slope determined from the single homogeneous phantoms (Figure 4.2 (c)). The curve of the top layer of the double layer phantom agrees with the 0.5% linear curve and the curve of the bottom layer agrees with the 0.25% slope. An artifact is observed at a depth of ~300μm which is due to the plastic film that was used to separate both layers. Also, at about ~700μm the curve of the bottom layer deviates from its linearity. This is because the product of the depth times the attenuation coefficient is no longer smaller than 1; therefore, the reconstruction for these depths becomes less accurate.

The experiments presented in this paper were done in solid gel phantoms. These phantoms allowed us to obtain strong signals from the structure inside the phantoms. For liquid phantoms, these experiments are more challenging because the structures inside the liquids are constantly moving due to Brownian motion and make it difficult to accurately determine the phase of the scattering structure. A solution for liquid phantoms has previously been demonstrated by measuring the signal at the interfaces at the surface of the liquid [143, 144, 146]. A challenge of this method for measuring hemoglobin *in vivo*, is that OCT images present shadow effects underneath blood vessels, which would reduce the signal obtained at the vessel boundary.

A limitation of the system is that it is slow (125ms for an M-scan). This can be improved by increasing the modulation frequency of the pump laser. However, a higher modulation frequency will mean less time to allow for the drug to increase its temperature; therefore, a lower signal will be obtained. This can be compensated by increasing the laser power, but the temperature increase should be carefully monitored to avoid therapeutic effects.

This model can be used for imaging absorber concentrations *in vivo*. It is assumed that the thermal expansion properties and changes of the index of refraction as a function of temperature between the agar gel phantom and biological tissues are similar.

4.6 Conclusions

In this chapter, using PT-OCT, a model that describes the photothermal signal as a function of depth has been developed. The parameters of the model have been empirically derived using homogeneous single layer phantoms, and it has been determined that the slope of the curve of the model is dependent on both the laser power and the ink concentration. The model is also minimally dependent on the distance between the surface of the phantom and the zero-delay line for distances smaller than ~1mm. A concentration reconstruction algorithm is developed that is limited to small values of the product of the depth times the attenuation coefficient. The algorithm was validated in solid homogeneous single and double layer phantoms.

This technique can be used in biological tissues using exogenous and endogenous contrast agents that are more suitable for medical applications; such as gold nanoparticles, indocyanine green and hemoglobin. By monitoring the pump laser power and properly calibrating the results, it expects to minimize the noise in the results obtained. An advantage of using photothermal compounds is that they can be multifunctional, where they can be used as contrast agents for imaging and also as a therapeutic drug. Concentration images can be obtained from biological tissues, and when a specific dose is achieved, the temperature of the drug can be properly increased to damage the surrounding tissues.

Chapter 5 PT-OCT for detection of Nanoparticles

This chapter demonstrates an application of PT-OCT, for imaging multifunctional nanoparticles as a contrast agent for enhance the imaging quality of PT-OCT. The results is achieved with the assistance of Dr Yeongri Jung who fabricated the nano-probers and prepared the animals for study.

5.1 Introduction

Several contrast agents have been developed to enhance the performance of current imaging modalities, such as ultrasound and nuclear magnetic resonance (MRI) imaging [156, 157]. Recently advances in nanotechnology have enabled the development of various nano-sized contrast agents for applications in many research areas such as diagnosis and therapy as well as the development of innovative imaging techniques [158].The physical and structural properties of these agents can be customized to enhance the signal-to-noise ratio (SNR) of the imaging modalities they have been developed for. For example, quantum dots with uniform size and fluorescence properties have been developed for the study of intercellular and/or intracellular processes at the single-molecular level [159]. Unfortunately, these agents present potential human toxicity and cytotoxicity due to the semiconductor materials from which they are made; this is a significant limitation for in vivo biological applications.

Gold nanoparticles have become an attractive imaging contrast agent because they present low toxicity and can be synthesized for immuno-targeting. Recently, the light scattering properties of gold nanoparticles have been used with scattering-based optical modalities, such as optical coherence tomography (OCT), to enable high resolution imaging for early cancer detection [160, 161]. However, the improvements are limited by the low SNR due to the high scattering background of biological tissues.

Unlike the conventional OCT image, which is reconstructed from the back scatted photons, the PT-OCT image can distinguish the gold nanoparticles from the biological tissues by using the difference of optical absorption properties. Gold nanoparticles can be easily customized to absorb light within the near-infrared (NIR) region, an attractive spectral window that presents low absorption in biological tissues enabling deeper light penetration. Also, gold nanoparticles exhibit PT (converts light into heat) and PA (converts light to sound) properties, which have been used for both diagnosis and treatment (i.e. photothermal therapy) of several diseases [158].

Similarly, magnetic nanoparticles (MNP) have been designed for diagnosis and therapy in magnetic resonance imaging (MRI) [157, 162]. Their most unique feature is the ability to react to a magnetic force, which has been utilized for a number of bio-applications [163]. MRI provides high tissue penetration; however, it presents low spatial resolution and molecular sensitivity, which limits its applicability for molecular imaging. On the other hand, optical imaging techniques generally have higher spatial resolution and molecular sensitivity, but with a tissue penetration depth limited to a few millimeters. A contrast agent with multifunctional properties can enable a combination or new imaging method that takes advantage of the benefits from each imaging technique.

In this regard, Jin et al.[164] recently developed a new class of multifunctional nanoprobes that uses iron oxide and gold coupled core-shell nanoparticles with well-defined structural characteristics to yield magnetic and absorption properties appropriate for MRI and photoacoustic imaging. However, the size of the synthesized nanoparticles is in the order of ~30 nm, difficult to be used as a contrast agent to enhance the ability of scattering-based optical imaging techniques. In this study, we report the synthesis of gold-coated magnetic silica nanoparticle (GMSNP) that exhibits coupled magnetic, scattering, and NIR absorption properties. We then focus on the potential use of these synthesized, multifunctional nanoparticles to enhance the utility of scattering-based optical coherence tomography (OCT), photothermal OCT, and magnetomotive photoacoustic (mmPA) imaging techniques.

Sentinel lymph nodes (SLN) are the first draining lymph nodes that are reached by a metastatic cancer cells from a primary tumour. Thus the SLN surgery is performed to determine if the cancer has spread to the very first draining lymph node or not, which can be used as the indicator of cancer metastasized. The standard of care requires pathologists to observe histological samples of the SLN, which requires destroying the samples. Some imaging techniques have been used to mapping the location of SLN *in vivo* noninvasively, such as, MRI, nuclear imaging and computed tomography [165-168]. Various contrast agents such as iron oxide nanoparticles and quantum dots [165, 169, 170] have been applied to enhance the success rate of these non-invasive imaging modalities. Recently, photoacoustic imaging has been reported mapping the location of SLN's in vivo using nanoparticles as the contrast agent [171, 172]. Although these technologies succeed on identifying the location of the SLN, they have poor resolution for imaging the structure detail when compare to histological samples.

OCT is a non-invasive label free technology to three-dimensional cellular and subcellular tissue morphology with micrometer-scale resolution. OCT has recently been used to provide images of lymph node morphology ex vivo [173]. The reported OCT images depict morphological structures that corresponded well with histological features of the lymph nodes (LN), suggesting the potential of using OCT to visualize lymph node microstructures on a scale of micrometastases and to detect metastatic nodal diseases intraoperatively. However the morphological studies detected no significant differences between the OCT structure image of lymph nodes from tumor-bearing animals and control animals. PT-OCT is sensitive to the optical path length changes that are induced in the tissue by temperature changes caused by pumping laser. Contrast agent such as gold nanorods (GNRs) could be customized to have high absorption with a narrow spectral bandwidth in the near infrared (NIR) region, an optical window where biological tissues have low absorption. GNRs are biocompatible and the gold surface can be conjugated with antibodies and peptides that bind selectively with proteins associated with specific diseases, such as cancer [174].

In this chapter, the use of multifunctional nanoparticles as a contrast agent for enhance the imaging quality of PT-OCT was demonstrated. The phantom experiment was carried out for the validation of the concept and SLN with multifunctional nanoparticles was studied to test the capability of the PT-OCT for detecting the uptake of multifunctional nanoparticles at different SLN structures. The application of PT-OCT, for imaging multifunctional nanoprobe uptake in sentinel lymph node of mice in situ was presented. This application can obtain higher quality images of lymph node structures due to the photothermal contrast properties of the multifunctional nanoparticles. It is also demonstrated that multifunctional nanoparticles accumulate differently within several lymph node structures, and this uptake is time dependent.

5.2 Material and methods

5.2.1 System configuration

A spectral domain photothermal optical coherence tomography (PT-OCT) system, which has been described in Chapter 4 was used. The experimental system is illustrated in Figure 4.1, a super luminescent diode (SLD) with a central wavelength of 1310 nm and a bandwidth of 83 nm was used as an OCT light source, providing an axial resolution of ~9 µm (SLD). The diode output was split into two beams (reference and sample arm) via a beam splitter. Light in the reference arm was reflected from a stationary mirror. A pump laser beam with a wavelength of 808 nm was used to photothermally excite the nanoprobe (maximum absorption peak of ~790 nm). The pump laser was modulated at 400 Hz with a function generator, producing an average optical power of ~0.125 mJ / cm2.

Light from the SLD and the pump laser were combined in the sample arm with a dichroic mirror, and focused into the sample with an achromatic objective lens with a focal length of 50 mm. The size of the focal spot on the sample was ~120 µm and ~20 µm for the 808 and 1310 nm light sources, respectively. A 2 × 2 optical fiber coupler was used to recombine the light backscattered from the sample and reflected from the reference mirror. The combined light was re-routed with the optical circulator towards a spectrometer, consisting of a 100 mm focal length collimator, a 1200 lines / mm transmitting grating, an achromatic lens with a 50 mm focal length, and a 14 bit, 1024 pixels InGaAs line scan camera with a maximum acquisition rate of 47 kHz. This spectrometer setup had a spectral resolution of 0.055 nm, which gave a maximum imaging depth of ~3.0 mm. A personal computer was used to synchronously control the acquisition of the camera and the square wave excitation of the pump laser. 1000-line M-mode acquisition was performed at each transverse position with an acquisition rate of 2238 Hz.

To determine the photothermal effect, nanoparticles were excited with the 808 nm light source. The absorbed light increases the temperature of the nanoparticles, leading to a change in the optical path length of the tissue where the absorber is localized.

Optical path length changes were detected by measuring phase changes in the OCT signals using the PT-OCT system.

5.2.2 Sample preparation

5.2.2.1 Multi-functional magnetic gold nanoshell preparation

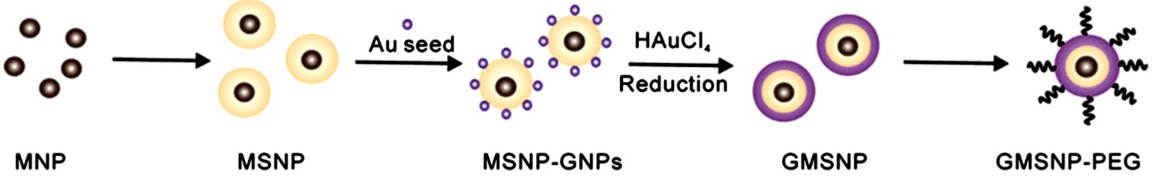

Figure 5.1 Schematic illustration of GMSNP synthesis.

Figure 5.1 schematically steps through multifunctional magnetic gold nanoshell preparation. First, the MNPs were prepared by thermal composition as previously described [175], onto which the magnetic silica nanoparticles (MSNP) were prepared through the water-in-oil micro-emulsion technique using tetraethyl orthosilicate (TEOS). In doing so, pre-dissolved magnetic nanocrystals in cyclohexane (2 mg mL^{-1}) were injected into a predissolved surfactant of 8 mL Igepal CO 520 in 200 mL cyclohexane. In this case, the concentration of MNP dissolved in cyclohexane was varied from 0.4 to 2 mg mL^{-1}, which would make desired silica shells with a thickness ranging from 7 to 12 nm. Then, 1.3 mL of 30% NH4OH solution was added drop by drop and vigorously stirred for 10 min with an additional 3 mL TEOS. The mixed solution was stirred for 15 h at room temperature and then was washed with ethanol and centrifuged five times to produce MSNP. The surface of the resultant MSNP (0.4 g) was functionalized with amine groups by treating with 3-aminopropyltrimethoxysilane (75 μL) in refluxing ethanol (50 mL) for 3 h. Subsequently, the MSNPs were purified by centrifuging and dispersed in water. A gold seed solution of 2 to 3 nm was prepared to synthesize the gold-nanoparticle attached MSNP (MSNP-GNP) according to the protocol reported [176]. Briefly, 0.5 mL of 1M NaOH and 1 mL tetrakis(hydroxymethyl) phosphonium chloride (THPC, prepared by adding 12 μL of 80% THPC in water to 1 mL deionized water) were added into 45 mL water, and then the mixture was stirred for 5 min. 2 mL of 1 wt.% HAuCl4 was added quickly to the stirred solution. Next, 10 mg of amine functionalized MSNP in 5 mL ethanol were stirred with freshly prepared 2 to 3 nm sized gold seed solution for 2 h. The resulted solution was centrifuged and dispersed in 1 mL water, resulting in MSNP-GNP ready for use.

The following steps were used to grow gold nanoshells onto the MSNP-GNPs. First, 25 mg potassium carbonate in 100 mL water was mixed with 2 mL of 1 wt.% HAuCl4. In this way, the color of the mixed solution would change from yellow to colorless. At this step, while vigorously stirring the solution, we added 200 μL of the MSNP-GNPs into 5 mL of the colorless solution, the color of which changed from colorless to blue, meaning that the GMSNP was formed. Then, the GMSNPs were centrifuged and re-dispersed them 1 mL water. For ultimate in vivo imaging applications, polyethylene glycol with attached thiol group (mPEG-SH) can be conjugated with the GMSNP so that it is biocompatible. Note that apart from the GMSNP, all nanoparticles resulting from intermediate steps above are readily available for different imaging purposes by utilizing their unique optical properties.

5.2.2.2 Animal Preparation

Thirty six mice (C57 BL/6) that weighed ~23g were used to image the uptake of GNRs within their left popliteal SLN in situ. All experimental animal procedures were in compliance with the Federal guidelines for care and handling of small rodents. Each mouse was anesthetized with vaporized isoflurane (0.2 L/min oxygen and 0.8 L/min air), and their body temperature was kept at 37 C with the use of a heating pad. A volume of 100 μL of GNRs (0.8 nM) was injected through the femoral vein of the right leg. At each time point (0, 0.25, 4, 8, 12, 24, 48, 96, 140, 320, 456, and 672 h), three mice were sacrificed and their left SLN was dissected and imaged with the PT-OCT system. During imaging, the SLN was kept in solidized 1% agar gel.

5.3 Data Acquisition and Processing

The procedure is similar as descripted at chapter 4.2.3 for the scanning of each B-frame. Photothermal images were obtained by modulating the pump laser at 400Hz with a square wave (50% duty cycle), and obtaining 1000 A-scans from the same location (also known as an M-Scan) at a frequency of 2.238kHz. Figure 5.2 illustrates the data processing procedure. The GNRs absorb the energy from the 808 nm laser and cause the temperature change of the tissue where the absorption is localized. Therefore, unlike the scattering based conventional OCT, PT-OCT image is directly related to optical absorption, leading to background free imaging of endogenous and exogenous contrasting agent.

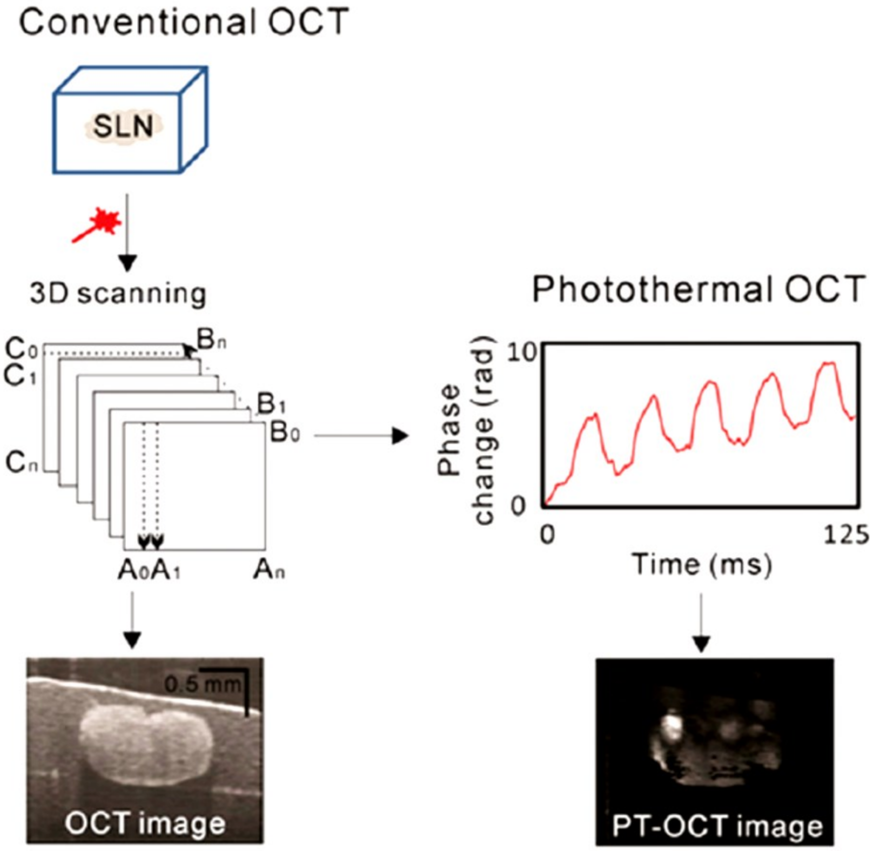
Conventional OCT
SLN
3D scanning
C0
C1
Cn
Bn
B1
B0
A0A1
An
Photothermal OCT
Phase change (rad)
10
0
0
125
Time (ms)
0.5 mm
OCT image
PT-OCT image

Figure 5.2 Diagram of the data processing method to image the GNRs uptake in the SLN

5.4. Results and discussion

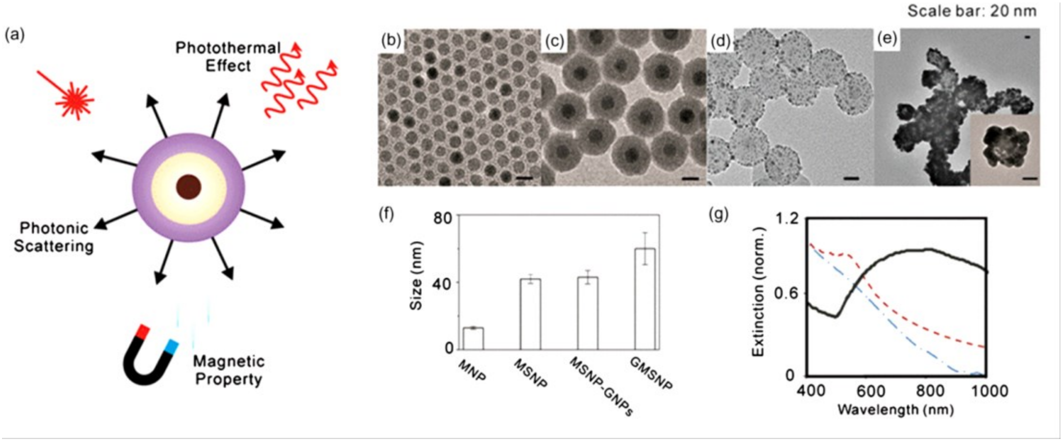

Figure 5.3 (a) Illustration of the multifunctional properties of GMSNP as a contrast agent for optical imaging techniques. Transmission electron microscopy images of (b) MNP, (c) MSNP, (d) MSNP-GNRs (e) GMSNP. (f) The size distribution of each nanoparticle. (g) UV-Vis-NIR extinction of MNP, MSNP and GMSNP. The characteristic absorbance of GMSNP is red-shifted due to the outer gold shell.

Figure 5.3 illustrates the multifunctional properties of the nanoprobe. The gold shell's physical properties are similar to gold colloids and exhibit high scattering and absorption properties due to the strong plasmon resonance of the metallic, dielectric, concentric, and spherical configuration [177]. To illustrate the multifunctionality of the nanoprobes as a contrast agent for optical imaging techniques, we tested their physical and characteristic properties including size, extinction spectrum, photothermal and magnetic properties. Using TEM, we were able to determine the diameter of the particles at different stages of synthesis. Fig 5.4(b)–(e) present TEM images of MNP, MSNP, MSNP-GNPs and GMSNP, respectively, and Figure 5.3(f) shows the average and standard deviation of particle diameters. The spectral extinction at different stages of nanoprobe development is presented in Figure 5.3(g). The maximum absorbance (λ max) of the GNPs as seeds is at 520 nm; however, λ max of GMSNP is red-shifted to 800 nm due to the formation of a gold nanoshell on the silica surface. The peak of the extinction can be tuned by varying the core size and shell thickness. Ideally, the desired absorption peak should be located within the NIR region where the optical penetration depth in biological tissue is high due to low absorption.

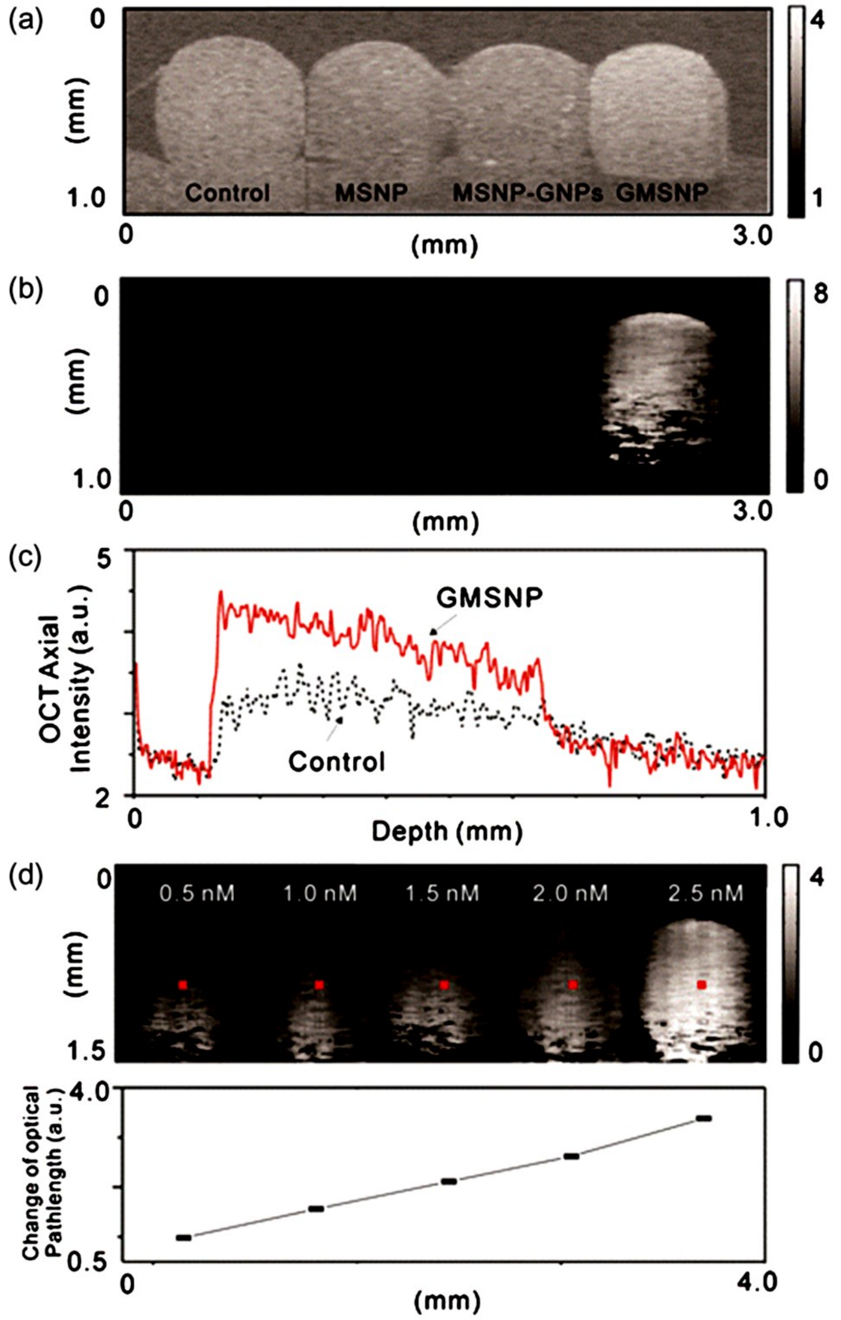

Figure 5.4 (a) Conventional scattering and (b) photothermal OCT images of control, MSNP, MSNP-GNPs and GMSNP at a concentration of 5.0 nM. (c) depth-dependent OCT intensity decay of control and 5.0 nM GMSNP. (d) At different concentrations of GMSNP, photothermal images show distinguishable contrast, even though the concentration increases over a small range (left: 0.5 nM, middle: 1.5 nM, Right: 2.5 nM). Red spots indicate the central area of phantoms (e) Plot of photothermal signal strength at the center of each phantom in (d).

Fig 5.4 (a) and (b) show scattering and phothothermal OCT images obtained from a control phantom and phantoms with 5 nM MSNP, MSNP-GNP, and GMSNP. Qualitatively, we can observe that the signal of the GMSNP phantom is higher compared to the others. Figure 5.4 (c) shows an example of the OCT axial intensity (A-scan) obtained from the middle point of the control phantom and the GMSNP phantom. The slope of the GMSNP phantom is higher than the control, an indication of higher attenuation coefficient.17 The MSNP and MSNP-GNP had a similar curve as the control phantom (data not shown).

To test the efficacy of GMSNP as a photothermal contrast agent, we obtained PT-OCT images. The phantoms were excited with an 808 nm laser. Figure 5.4 (b) shows a B-scan photothermal OCT image of the phantom before and after gold nanoshells are delivered at a concentration of 5.0 nM. Compared with nonabsorbing nanoparticles, GMSNP was the only particle with a photothermal signal due to its strong surface plasmon resonance from the outer gold nanoshell. Figure 5.4 (d) shows photothermal images at concentrations of 0.5, 1.0, 1.5, 2.0, and 2.5 nM. The PT signal increases with increased GMSNP concentration. Figure 5.4 (e) shows the photothermal signal obtained from the center point of each phantom. As expected, the photothermal signal is nearly linear with the concentration of GMSNP. It is important to note that the photothermal properties could also be used for phototherapeutic applications.

The sensitivity of GMSNP on photothermal OCT is 0.5 nM, for an illumination power of 0.125 mJ / cm2. The sensitivity would increase proportionally with an increase in the laser power. It has been demonstrated that with a power of 2.5 mJ / cm2, photothermal OCT can be sensitive to 2 pM gold nanorods [178].

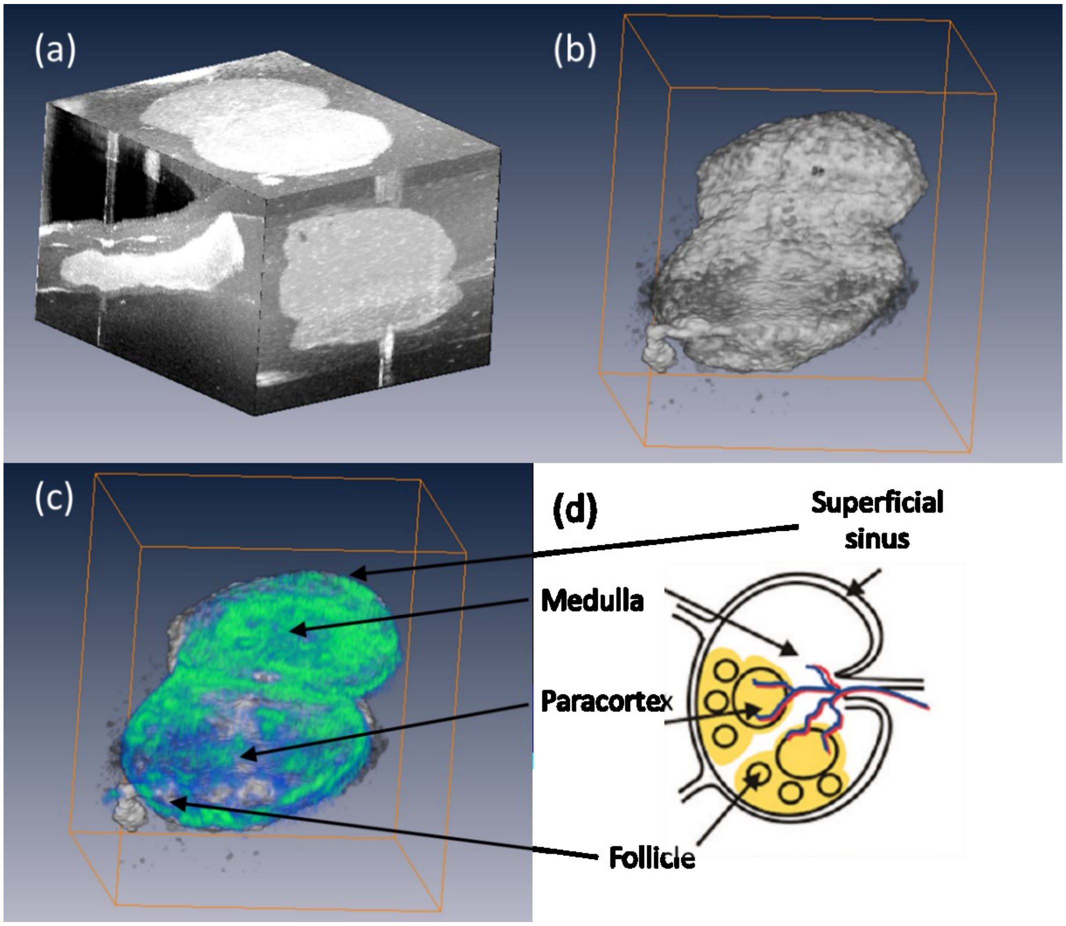

Figure 5.5 (a) Three-dimensional OCT projection image of a dissected SLN at 140 h after GMSNP injection. (b) 3D OCT view of SLN morphology (c) The same as in (b) but was from PT-OCT images to highlight SLN structures. (d) Schematic diagram of a dissected SLN. (Volume size = 2.5 x 2.5 x 2.0 mm)

Fig 5.5 (a) shows the three-dimensional projection view of a dissected SLN at 140 hours after GMSNP injection obtained with the PhS-OCT system. Fig 5.5 (b) shows the three-dimensional SLN structure image which delineates the typical morphological features of the SLN. It can be observed that the conventional OCT structure image cannot detect the nanoparticle accumulation because of the low scattering contrast that is present on the GMSNP. However, in the PT-OCT image (colourful image in Fig 5.5 (c)), the imaging contrast is significantly improved by the phothothermal properties of the GMSNP. The PT-OCT image delineates the uptake of GMSNP throughout the SLN, and by combining both the OCT and PT-OCT images we can distinguish the distribution of GMSNP in several SLN structures. The intravenously injected GMSNP migrate out of the venules and mostly accumulate in the superficial sinus, which is a channel that filters foreign organisms. Also, the GMSNP accumulate at the cortex surrounding follicles, where mainly B cells and intrabecular sinus are filtered.

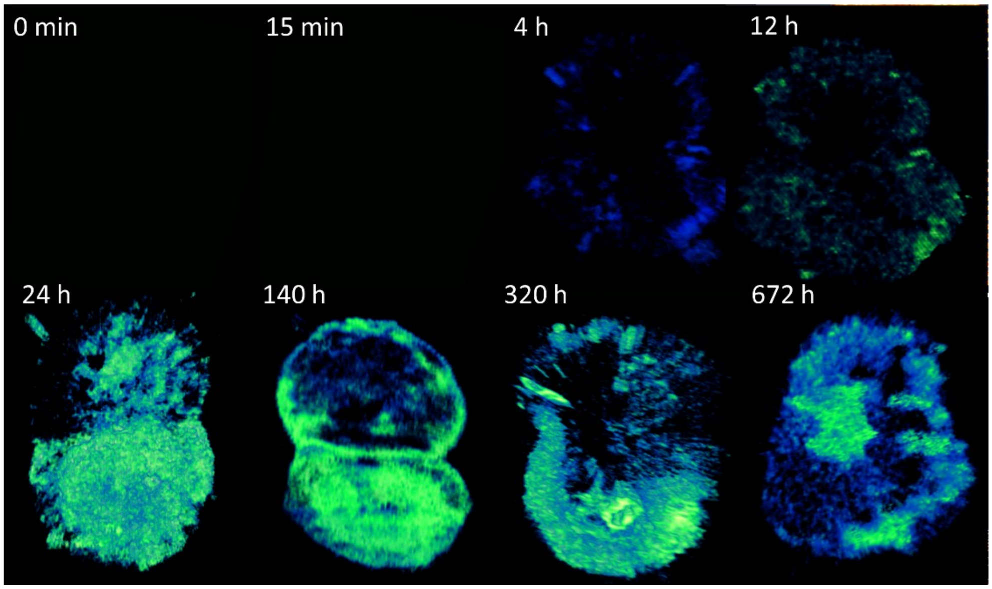

Figure 5.6 Uptake of GMSNP within the SLN at different time points.

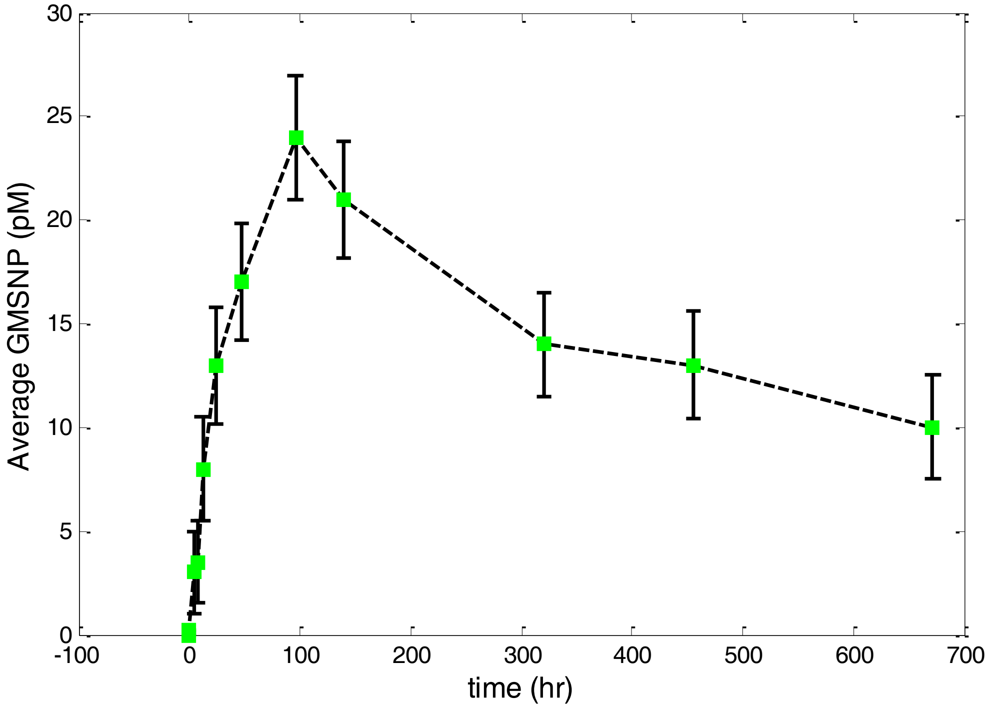

Figure 5.7 Average concentration of GMSNP throughout the whole SLN as a function of time

Time-dependent lymph node uptake of nanoparticles has been investigated by other researchers and typically focused on time points in the range of 6-120 h postinjection [179, 180]. To further evaluate the GMSNP uptake, PT-OCT images were acquired at 0, 0.25, 4, 8, 12, 24, 48, 96, 140, 320, 456, and 672 h after the 1 nM GMSNP injection. This enabled us to visualize the time-dependent GMSNP uptake within the SLN. Fig 5.6 shows projection images of the GMSNP uptake within SLN at the specified time points. Figure 5.7 shows the time dependent average concentration of GMSNP. It is observed that the concentration reaches a peak of ~24 pM at 96 h, and after that the concentration slowly declines. Compared to the initial GMSNP injection (1 nM), the maximal lymph node uptake of about 2% can be achieved with GMSNP at 96 h.

The use of GMSNP enables us to understand the functionality of the SLN in many ways using PT-OCT. First, the GMSNP are a source of high contrast that allows us to obtain high-resolution images of different SLN structures. Second, the use of PT-OCT may be useful in delineating the migration pattern of the GMSNP within different SLN structures as a function of time.

5.5 Conclusions

In this chapter, a multifunctional nanoparticles is fabricated as a contrast agent for enhance the imaging quality of PT-OCT, MRI and photoacoustic. This nanoprobe is adapted for study of PT-OCT's application of in situ SLN samples from a mouse model. Compared to conventional scattering OCT, the PT-OCT system can monitor the distribution of GMSNP within specific SLN structures through time. The uptake of GMSNP within a SLN is slow (reaching a peak at ~96 h) indicating that the GMSNP have long circulation times. The resulting SLN images show that GMSNP are suitable as a contrast agent. Although the imaging experiments were conducted in situ, we expect to be able to obtain these images in vivo and in real time with the aid of a catheter. For clinical applications, there are still significant challenges, such as laser safety issue; how to locate the interested area; imaging depth and scanning speed for real time monitoring. Needle OCT could be a potential solution to conquer limitation of imaging depth, as the development of optical sensor and computer science, the real-time monitoring during operation could be achieved in the future.

Chapter 6 Quantitative Optical Coherence Elastography (OCE)

6.1 Introduction

The alteration of mechanical properties with tissue deformation is commonly observed in tissue pathologies. The assessing of mechanical properties could significantly improve the understanding of tissue patho-physiology, which will aid medical diagnosis and treatment diseases. Consequently a number of elastography technologies have been developed recently for qualitative and quantitative assessment of tissue mechanical properties [1, 4, 181, 182].The main idea in elastography is to use a sensitive device to quantify the image of mechanical disturbance, which is induced directly or indirectly by a mechanical stimulation, such as compression, vibration, or acoustic radiation [181]. Ultrasound elastography [1, 4, 182] and magnetic resonance elastography (MRE) [16, 47] are the most common methods in medical diagnosis that involve either ultrasound or magnetic resonance imaging (MRI) to measure the passive tissue disturbances, from which the mechanical properties of tissue are obtained. Despite their success in cardiac applications, these methods are limited by low spatial resolution, which is not sufficient to detect early and small lesion in tissue.

The Optical Coherence Elastography (OCE) technology, which is based on optical coherence tomography, is an emerging non-invasive imaging modality, capable of producing both high resolution cross-section structure image and stress image through highly scattering media such as biological tissue. Kennedy et al. [183] applied OCE for in vivo characterization of normal and hydrated human skins, relying on the dynamic OCT system in combination with a designed ring actuator, which induces longitudinal vibration to samples. More recently, this technique was developed in providing the three-dimensional OCE images of human skin. However, they do not provide a quantitative measurement of elasticity in these studies.

This chapter provides a brief introduction of mechanical properties of tissue. The theory of quantitative OCE is presented in details along with the system setup and processing algorisms. Quantitative OCE method is developed to provide localized and quantitative mechanical properties of phantoms and tendons. In this chapter fundamental characterization technique of OCE forms the basis of chapter 7.

6.2 Mechanical properties of soft tissue

In soft tissues, important parameters of mechanical properties include elasticity (Young's modulus), Poisson ratio and density. The Poisson's ratio and density do not vary much, as it is usually in the range of 0.490 to 0.499 as biological soft tissues are usually uncompressible [184-186], and the corresponding values of density are 920 to 1060 kg/m^3 [184-186]. The elasticity varies with different kinds of soft tissues (as shown in Table 6.1). It is one of the most important parameters as it reveals the stiffness of the tissue, thus indicating the pathological conditions.

Table 6.1 Young's modulus of various types of human tissue from literature

Tissue	Type	E (kPa)	Tissue	Type	E (kPa)
Breast	Unspecified	29 [187]	Kidney	Unspecified	10 [188]
		21 – 23 [189]			6 [189]
	Adipose	19 [190]	Liver	Unspecified	13 [191]
	Glandular	33 [190]			10 – 17 [192]
	Fibrous	110 [190]			7 – 10 [189]
		1.8 [193]			1 – 3 [194]
Muscle	Unspecified	14 – 16 [189]			0.4 - 1.7 [195]
		10 – 40 [194]		Normal	10 [196]
		7 – 57 [197]			0.6 - 1.1 [191]
		1.2 – 1.8 [195]		Focal nodular	1.2 - 2.5 [191]
	Intercostal	100 [198]		Hyperplasia Chronic Hepatitis	35 [191]
	Cardiac (systole)	100 [197]			

Destructive testing is most traditional way to understand the mechanical properties and behaviours of a material. As a result, material stress-strain curve can be obtained. A typical stress-strain curve is shown in Figure 6.1. Here, Stress is the external force acting on the object per unit area. Strain is the result of a stress, defined as the change in length per unit length. At the beginning phase of tension test of soft tissue, it can be observed so called toe region. Typical strain value of toe region is ranging from 0-1.5% [196]. In this region, the relation between stress and strain is nonlinear and the slope is increasing with increased loading. The reason for the increasing slope is the straightening of the wave-like collagen fibrils.

After the collagen fibrils are completely straightened begins the elastic region. In this region, the stress and strain are linearly related and the slope of the curve is called the Young's modulus of tissue. Thus, the Young's modulus (E) is defined as:

$$E = \frac{\sigma}{\varepsilon} = \frac{F/A}{\Delta L/L_i} \tag{6-1}$$

where $\sigma = F/A$ is the stress, F is the external force applied to the cross-sectional area A, and $\varepsilon = \Delta L/L_i$ is the strain. The unit Young's modulus is Newton per square metre (Nm^{-2}) or Pascal (Pa). In the elastic range, all changes of a tissue are reversible, i.e. if the stress is removed tissue returns to the original strain. The linear region of stress-strain curve is usually used for an accurate estimation of the tissue elasticity, where strain (ε) is controlled lower than 5%. Thus, material would be kept safe without fail.

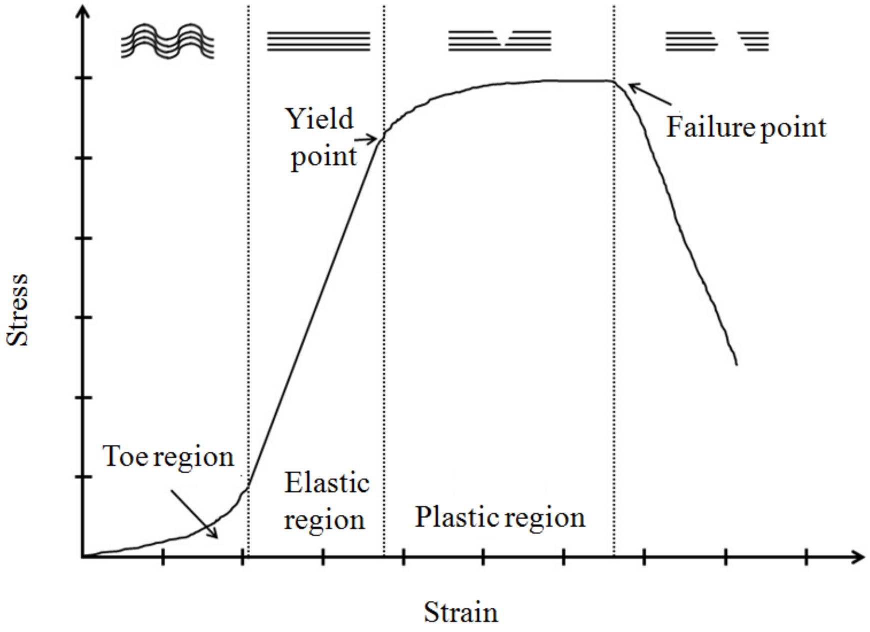

Fure 6.1 Typical stress-strain relation in soft biological tissues [196]

When the stress is further increased from the elastic region, the slope of the curve changes and the plastic region begins, with the yield point separates elastic region and plastic region of the graph. After the yield point tissue begins to experience destructive changes. In the plastic region irreversible changes have occurred in a tissue and it does not return to the original shape when the stress is completely removed. After the plastic region, failure of the tissue occurs. Strain and stress of tissue disappear. The location of the breakdown is called the failure point.

Soft tissue behaves as a non-homogeneous, anisotropic, non-linear viscous-elastic material subjected to pre-stress with the experimentally obtained Young's modulus of the layers varying considerably. The mechanical properties of soft tissue depend on the nature and organization of [199]:

- Dermal collagen and elastic fibres network;
- Water, proteins and macromolecule embedded in the extracellular matrix;
- Factors like individual's age, body site, gender, race and nutritional status.

6.3 Current mechanical properties characterization method

Currently in clinic, mechanical properties measurement for the diagnosis of diseases largely depends on visual assessment and palpation performed by a trained doctor; however, palpation results vary from person to person. There are often conditions where there is a clinical need for quantitative information on the skin mechanical properties. Elastography begin to attract medical application from last decade. The main idea of this technology is to combine imaging modalities with different mechanical stimulations to generate tissue responses in the form of displacement that can be subsequently measured, so that mechanical properties may be evaluated and mapped with anatomic information of the biological tissue.

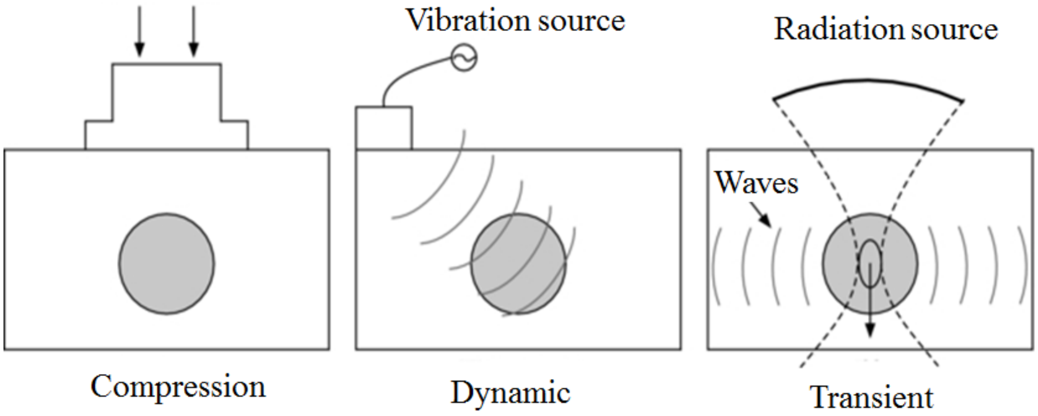

Figure 6.2 Schematic representation of current approaches to elastographic imaging: compression elastography (left), Dynamic elastography (middle) and transient elastography (right).

Elastography is a technique used to estimate and/or map the biomechanical (elastic) properties of tissue samples by use of imaging techniques. It can provide elastic as well as anatomic information of the biological tissue non-invasively. The main idea of elastography is to combine imaging modalities (e.g. ultrasonic, magnetic resonant and optical) with different mechanical stimulations (e.g. compression, vibration and transient stimulation) [200-202]. Mechanical stimulation generates tissue responses in the form of displacement, strain or vibration that can be subsequently measured by imaging systems so that the tissue mechanical properties can be evaluated and mapped. Currently, there are three kinds of elastography techniques: compression elastography, dynamic elastography and transient elastography (Figure 6.2).

A mechanical mode of compression elastography shows in Figure 6.3. When a spring is compressed (Figure 6.3(a)), displacement in each section of the spring depends on the stiffness of the spring (Figure 6.3(b)). Darker colour spring indicates spring with a higher stiffness a higher K (force constant) and lighter colour spring indicates tissue with a lower stiffness and a lower K. When a force is given to the spring, based on the Hooke's Law, a relationship between K, supplied force (F) and deformation distance (x) of the spring is: $F = -x \times K$, the deformation curve of springs can be obtained a soft spring compresses more than a hard spring. The strain distribution (Figure 6.3(c)) can be measured by spatially differentiating the displacement at each location. Then, different parts of soft and hard spring can be separated and mapped based on the different deformation value. Compression elastography techniques have limitations, as they can just provide the strain mapping of sample. With unknown stress, the true Young's modulus value cannot be estimated. In addition, the elastography is influenced by the force of the compression, thus the results varies between different persons in operation.

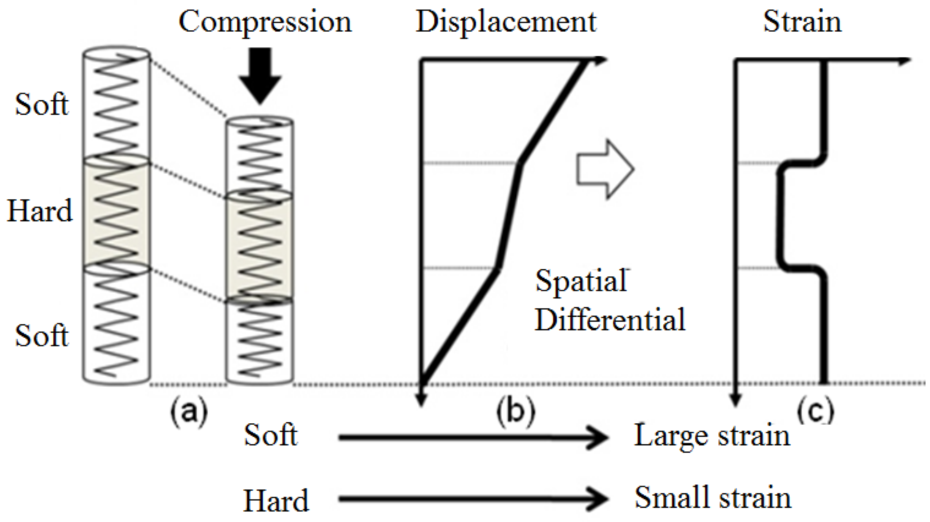

Figure 6.3 the principle of real time tissue elastography, illustrated here by a spring model [203].

In dynamic elastography, the material is submitted to low-frequency ((typically between 50 and 10,000 Hz) mechanical vibrations applied with an external vibrator. The vibration induce displacement of tissue, as mentioned before, based on Hooke's Law, the induced vibration amplitude and the corresponding strain of soft material is larger than that of hard material. By tracking the vibration amplitude by imaging systems, the strain distribution of material can be calculated and mapped. Similar with compression elastography, current dynamic elastography technique cannot provide quantitative elasticity information of tissue.

Transient elastography is able to provide the real stiffness of materials. In transient elastography, a transient (pulsed) load is applied to material. The transient load can be generated by a mechanical shaker, a short laser pulse or focused ultrasound. The load generates mechanical waves, including shear waves and surface acoustic waves. By tracking the waves using different imaging systems, wave speed can be measured. The wave speed is directly related to stiffness of material. Thus, the real stiffness of material can be estimated. However, low frequency of waves are usually induced to propagate inside of tissue to minimise attenuation. Low frequency of waves, which has higher wavelength, cannot differentiate subtle change of tissue mechanical properties.

The above mentioned elastography techniques have been developed to detect the mechanical properties of soft tissue based on ultrasound imaging and MRI. However, there are lacks of techniques in non-destructive, localised and quantitative mechanical properties measurements of tissue with ultra-high resolution which is able to difference elasticity change due to small lesions. This chapter thus explores the use of optical coherence tomography combine with dynamic elastography method to provide localized and quantitative mechanical properties of soft tissue. To achieve this goal, we applied a modulated vibration to chicken tendons ex vivo to induce phase change.

6.4. Material and method

6.4.1 System configuration

The system consists of both the generation of longitudinal waves (induced by an in-house designed and fabricated 30 kHz ultrasound transducer) and detection by PhS-OCT for soft tissue. In order to generate acoustic signals for the elasticity measurement, a transducer with resonant frequency of 30 kHz, which was driven by a square wave modulated RF signal (50% duty cycle amplifier modulation), was used. The modulation frequency was set to 30 kHz, and the maximum actuator displacement applied to the sample was ~50nm to ensure the generated strain was in the pure linear-elastic regime. In all experiments, samples were directly placed on the ultrasound transducer. The acoustic radiation force could then be transmitted from the transducer to compress the samples and trigger vibration in the axial direction.

For signal detection, the system was configured as M-mode acquisition, while the OCT probe beam stayed constantly in one location of the sample. The system provided a phase-sensitivity to the sample displacement of ~200 pm when working in M-scan mode. 2048 A-scans were acquired to obtain one frame of M-mode scan which takes about 22.3ms. The structural image of the samples generated by the PhS-OCT system is shown as a function of depth.

6.4.2 Sample preparation

To prove the accuracy of the acoustic radiation force method, 3 double layer phantoms with ~2% agar over ~1% agar, ~3% agar over ~2% agar and ~3% agar over ~1% agar and with ~1mm of upper layer thickness were created for testing.

Tendons are composed of uniaxial orientated collagen fibril bundles in hydrated elastin and proteoglycans matrix [204-208]. Its role is to reduce the impedance mismatch of the different tissues when transmitting contractile forces from the muscle to the skeleton [204, 205, 208] at the osseotendenous junction. Physical trauma in tendons due to high rate loading, laceration or degeneration due to ageing will rupture/damage collagen fibers, which will cause changes in tendon mechanical behaviour [209, 210]. Thus, the measurement of the mechanical properties of tendons is of great importance e.g. in predicting the severity of the injury to the tendons involved [211]; for diagnosis of tendon diseases [212]; in monitoring treatment procedures, e.g. tendon surgical repair [213, 214]; or for quantitative evaluation of tendon construction in tendon tissue engineering [215]. In this study, Tendon from chicken legs were used as the objects, for that they were fresh and easy to obtain in the everyday life. The chicken Achilles tendons were dissected from the fresh chicken leg and stored in PBS at 4 0C to keep them fresh, of which most were used for damage within 12 hours after dissection. The chickens Achilles tendon were approximately 1-2 mm in the diameter and 30-40 mm in the length. They were white, soft but tight before any treatment, which meant they were not possible to be extended or tore by hand.

To investigate the effectiveness of the OCE system in the detection of degenerative changes in tendinopathy, collagenase from Clostridium histolyticum (type Ⅰ collagen, Sigma) was used to degrade the collagen in the tendon to form a degenerated tendon model similar to pathological diseases. The collagenase powder was dissolved in deionised water to different concentrations. Tendons dissected from fresh non-frozen chicken (bought from supermarket) were treated with different collagenase concentrations (1 mg/mL, 3.3 mg/mL and 10 mg/mL) and with different incubation times (0, 30, 60 and 90 minutes) in the incubator at 37 ˚C and 5% CO_2. The collagenase was removed from the tendons in order to stop further digestion after the defined culture time.

After the treatments, tendons were imbedded in 2% agar-agar with ~0.5-1 mm thickness from the agar phantom surface. Agar is known to have very low scattering properties, thus, milk was added to each phantom at a concentration of 1% to produce a scattering background similar to what is found in biological tissues. Agar also keeps the tendon hydrated. For each concentration and incubation time span, 5 samples were prepared for experiment. Figure 6.4 shows examples of tendon samples in this study.

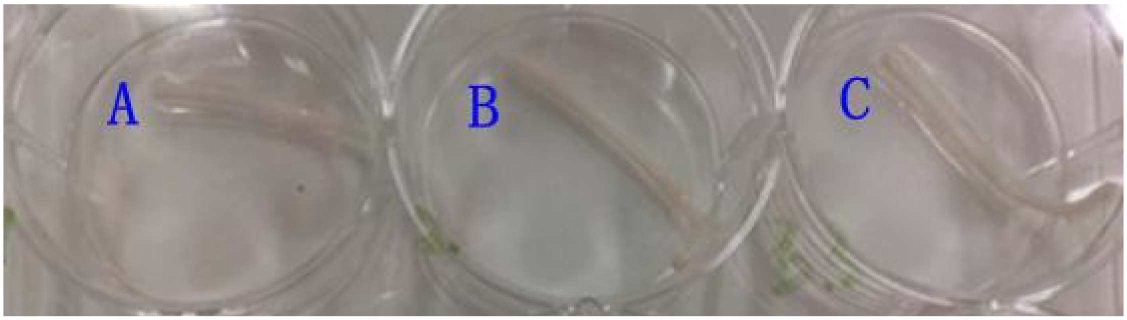

Figure 6.4 Chemical damage formed by the collagenase of various concentration of 1 mg/mL (A), 3.3 mg/mL (B), 10 mg/mL (C) by incubating the tendons for 60 minutes.

6.5 Data Acquisition and Processing

The application of vibration within the sample, which can be observed and detected as phase shift on PhS-OCT. We calculated the phase difference between the first and all the other A-lines (φ_i-φ_1), where i is a value between 1 and 2048 and φ is the phase angle of the A-line at a specific depth. It has been observed that the phase changed at each depth in Figure 6.5 (a) as dark and light bands through time. These bands represent a frequency response at 30 kHz, as shown in Fig 6.5 (c), which is the modulation of the ultrasound transducer.

Figure 6.5 (b) shows the phase differences, i.e. vibration through time at a depth of 700μm from the sample surface (the depth location was identified with an arrow in Figure 6.5 (a)). Vibration amplitude, which is directly related to the strain, was highly sensitive to the change of material elasticity. Under the same stress, softer material has higher strain and stiffer material has smaller strain. With respect to the Hooke's law of elasticity, Young's modulus is the ratio of stress to strain within the elastic region, which can be expressed as:

$$E = \frac{\sigma}{\varepsilon} \tag{6-2}$$

where E is the Young's modulus, σ is stress, and ε is strain. In the application of OCE to a 2-layered sample, constant stress fields can be assumed to apply to both layers. Thus, under the same stress ($\sigma_1 \approx \sigma_2$), in a heterogeneous material, the ratio of Young's modulus in different layer *1* and *2* is equal to the inverse ratio of the strain:

$$\frac{E_1}{E_2} = \frac{\frac{\sigma_1}{\varepsilon_1}}{\frac{\sigma_2}{\varepsilon_2}} = \frac{\sigma_1 \varepsilon_2}{\sigma_2 \varepsilon_1} \approx \frac{\varepsilon_2}{\varepsilon_1} \tag{6-3}$$

Here, the local strain is determined from the detected tissue displacement caused by the vibration amplitude [183]:

$$\varepsilon = \frac{\Delta L}{L} = \frac{d_2 - d_1}{\Delta z} \tag{6-4}$$

where d_1 is the displacement amplitude estimated at a depth of z from the top of the sample and d_2 is the displacement amplitude estimate at a depth of $z+\Delta z$.

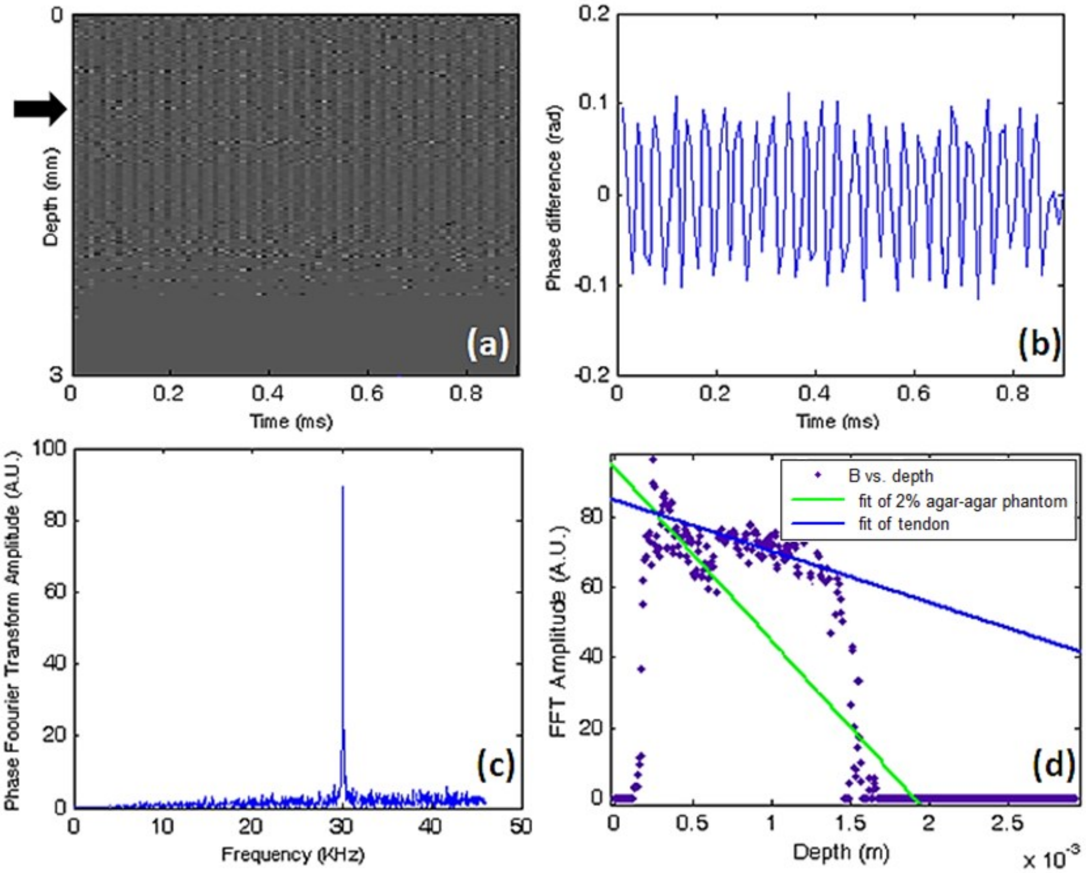

Figure 6.5 (a) M-scan of the phase difference obtained from the tendon-agar sample. (b) Phase difference as a function of time at a depth of ~700μm below the tissue surface {arrow in (a)}. (c) Absolute value of the Fourier transform of the phase difference (c). (d) FFT amplitude of the phase at different depths for sample (linear fit of agar layer-green line and tendon layer-blue line)

Figure 6.5 (c) presents the results of fast-Fourier transform of the phase difference FFT (*Δφ*) and therefore the amplitude from the data shown in Fig 6.5 (b). A peak at 30 kHz is clearly observed. The amplitude of this peak at each depth, after subtracting the background noise and averaging all the A-lines, is used to create the phase FFT amplitude signal as a function of depth (Figure 6.5 (d)). The phase difference caused by the vibration and the phase FFT amplitude are linearly related [42]. Combining Eq. 6-3 and Eq. 6-4, if we take the *Δz* to be long enough, the ratio between the slope of FFT amplitude from agar phantom and tendon gives the ratio of strain, i.e. the inverse ratio of Young's modulus.

A linear polynomial model has been chosen to fit the averaged phase FFT amplitude of both 2% agar layer and tendon layer in one sample (Figure 6.5 (d) green line and blue line) with 95% confidence bounds. The beginning and ending point of the fitting is decided by the surface of the agar and the interface of the two layers, however we need to sacrifice some fitting length due to the inaccuracy of data, which may be caused by some noise at the surface or sharp attenuation of backscattering light intensity at the deep part. Then, the slopes of the linear fit can be determined. Taking previous measurement values of the Young's modulus for 2% agar-agar phantom, 193kPa [20], and using the above mentioned inversion method, the quantitative Young's modulus of tendon can be evaluated.

6.6. Results and discussion

Figure 6.6 shows the amplitude of the FFT of the phase changes caused by the acoustic radiation force at different depths in both ~2% agar over ~1% agar and ~3% agar over ~2% agar phantoms. From Eq. 6-3 and Eq. 6-4, if we make the Δz long enough to cover the whole layer thickness, the ratio of slope of the FFT amplitude from different layers of the sample is equal to the ratio of shear wave strain. Thus, we apply a linear polynomial model fitted to the averaged phase FFT amplitude of different layers of phantoms (Figure 6.6 blue line and red dash line) with 95% confidence bounds. From Figure 6.6 (a and b) we find that at higher agar concentration the slope of FFT amplitude curve is smaller, as under the same stress the stiffer material will have a smaller strain.

From previous study, the average phase velocities calculated from SAW signals were ~12.33±1.03 m/s, ~7.55±1.09 m/s and ~4.87±0.94 m/s which yields a Young's modulus of ~515±3.59 kPa, ~193 kPa±4.01 and ~80±2.99 kPa for the 3%, 2% and 1% phantoms, respectively [20]. In Figure 6.6 (a), the estimated slopes of FFT amplitude curves for 1% agar layer and 2% agar layer are -67.51 and -25.57, respectively. The slope ratio of 2% and 1% is 2.64, which approximates the inverse ratio of Young's modulus of the two concentrations (2.41=193 kPa/80 kPa). Similar in Figure 6.6 (b), the estimated slope of FFT amplitude curves for 2% agar layer and 3% agar layer are -122.19 and -47.36. The ratio is 2.58, which approximates the inverse ratio of Young’s modulus of 3% and 2% agar (2.66 =515 kPa/193 kPa). We then try the phantom of ~3% agar over ~1% agar, which shows a more significant difference in Young’s modulus (results shown in Figure 6.7). As expected, the slope ratio of 1% agar and 3% agar vibration amplitude is 6.64 (-109.6/-16.5) which is similar to the inverse ration of Young’s modulus of 3% and 1% agar (6.43=515 kPa/80 kPa).

From the above phantom experiments, we have proven that the strain ratio, which is equal to the ratio of FFT vibration amplitude curve slopes, is approximate to the inverse ratio of its corresponded Young’s modulus. Knowing the ratio and Young’s modulus of any one material, the quantitative elasticity of connected other materials can be calculated easily.

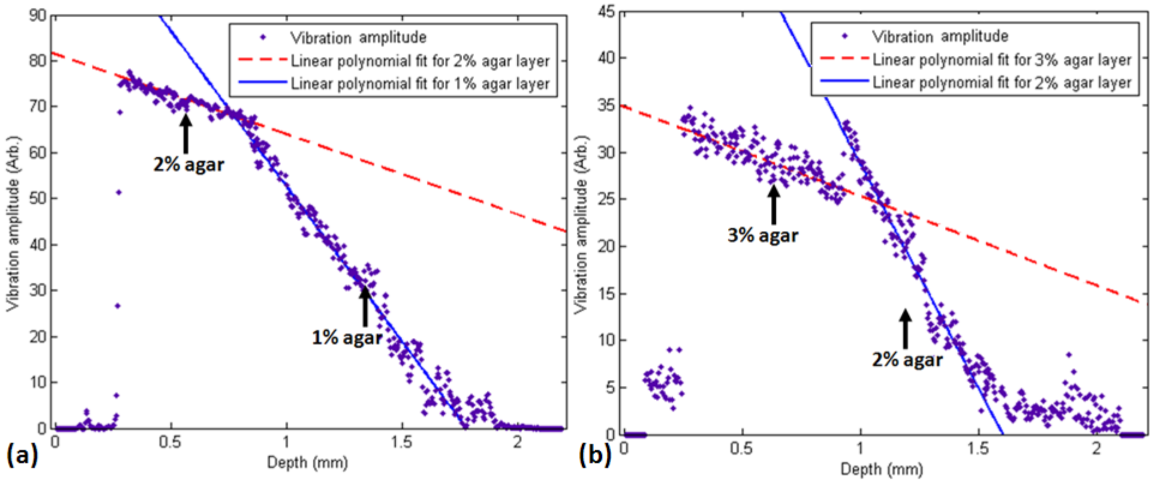

Figure 6.6 FFT amplitude of the phase changes caused by the shear wave amplitude at different depths and the linear model fit of (a) ~2% agar over ~1% agar and (b) ~3% agar over ~2% agar phantoms

There is an amplitude increase at the boundary between stiffer material and softer material, as seen in Figure 6.6 (b) and Figure 6.7. This is due to the fact that the shear wave travels from stiffer material to softer material, so the transmitted wave amplitude will be greater than the incident shear wave. The percentage is dependent on the materials’ acoustic impedances, which is the result of material density and acoustic wave velocity:

$$\frac{A_t}{A_i} = \frac{2z_1}{z_1 + z_2} = \frac{2\rho_1 c_1}{\rho_1 c_1 + \rho_2 c_2} \tag{6-5}$$

where A_t (A_i) is the transmitted (incident) wave amplitude, z, ρ, and c are the acoustics impedance, density and the acoustic wave velocity of the material. A stiffer material has higher density and shear wave velocity, thus, phenomena of amplitude increase can be observed.

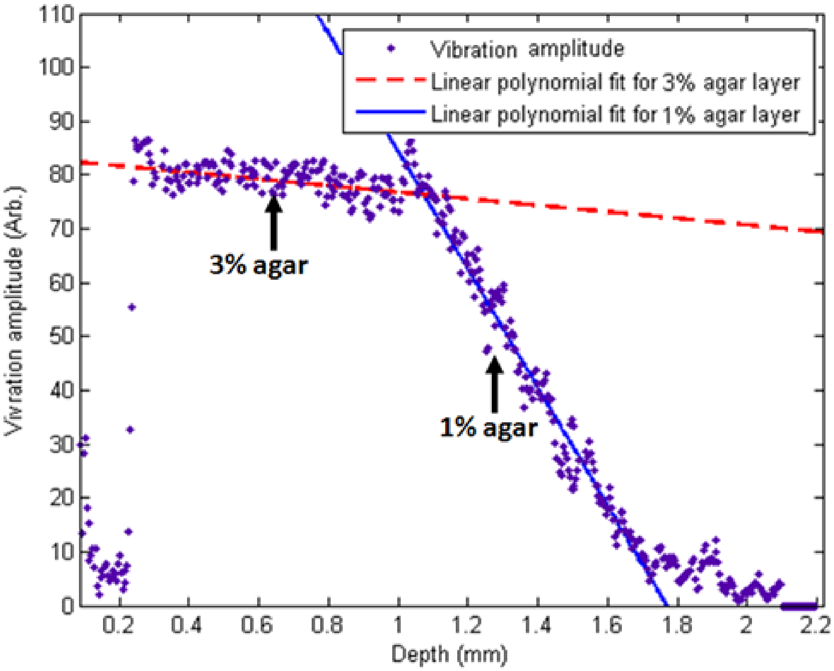

Figure 6.7 FFT amplitude of the phase changes caused by the shear wave amplitude at different depths and the linear model fit of ~3% agar over ~1% agar

Figure 6.8 (a) shows the real-time cross-sectional microstructures image (B-scan) of control tendon in a 2% agar phantom captured by the PhS-OCT system. The OCT image clearly demarcates the tendon tissue at ~0.8 mm depth below the phantom surface in this sample. It provides an indicator and cross-validation of the tendon boundary which can be used for the linear fit of the agar and the tendon layers. The vertical dash line indicates the depth range that can be detected by the OCT system. At the depth of 2mm, the system also stops the phase shift detection. Figure 6.8 (b) shows FFT amplitude of the phase changes caused by the vibration at different depths. Straight lines show linear model fits of the 2% agar area and control tendon without treatment. The estimated FFT amplitude curve slopes for the agar phantom layer and the control tendon are -9.367e+004 and -1377, respectively. This gives a phantom-tendon slope ratio of 68. We assume that both agar layer and tendon layer are homogeneous, and then this value can be treated as the ratio of strain for these two layers. According to Eq. 6-3 the Young's modulus of control tendon can be estimated as 13124KPa (~193 kPa*68).

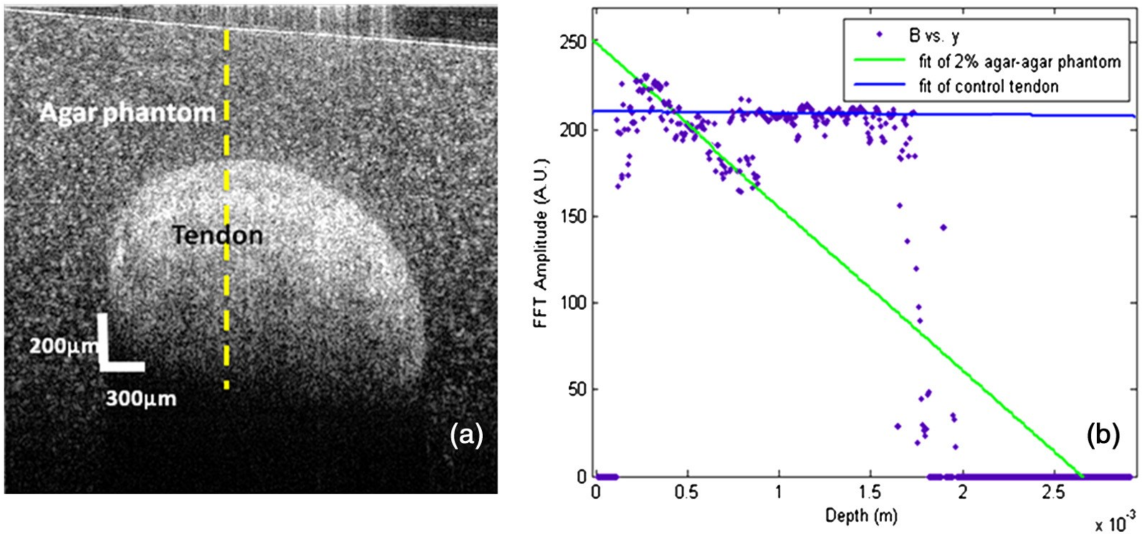

Figure 6.8 (a) Typical OCT image of 2% agar-tendon phantom, yellow dash line indicates the position of PhS-OCT detection beam for the phase change. (b) Averaged FFT amplitude of the phase changes caused by vibration at different depths and the linear model fit of (green) ~2% agar (blue) of control tendon.

Figure 6.9 shows typical averaged FFT amplitudes and the linear fits of the phase differences caused by vibration as the function of depth of tendon-agar samples that were treated with collagenase solution (concentration with 1 mg/ml, 3.3mg/ml and 10mg/ml collagenase solution and treatment time with 30 minutes, 60 minutes, and 90 minutes). As seen in Figure 6.9 (a, b and c), the slope difference between ~2% agar phantom and tendon sample was greatly reduced compared to the control group in

Figure 6.8 (b). This result indicates the Young's modulus of the tendon sample have been reduced, as was expected because collagen fibers have been damaged by collagenase. With the treatment time increased to 60 minutes and 90 minutes, the averaged FFT amplitude slopes of tendons increased. For example, the averaged FFT amplitude slopes became nearly equal to (Figure 6.9 (f)), and larger (Figure 6.9 (i)) than that of the agar phantom, which indicates that the Young's modulus was equal and smaller than that of agar phantom with 60 and 90 minutes treatment respectively.

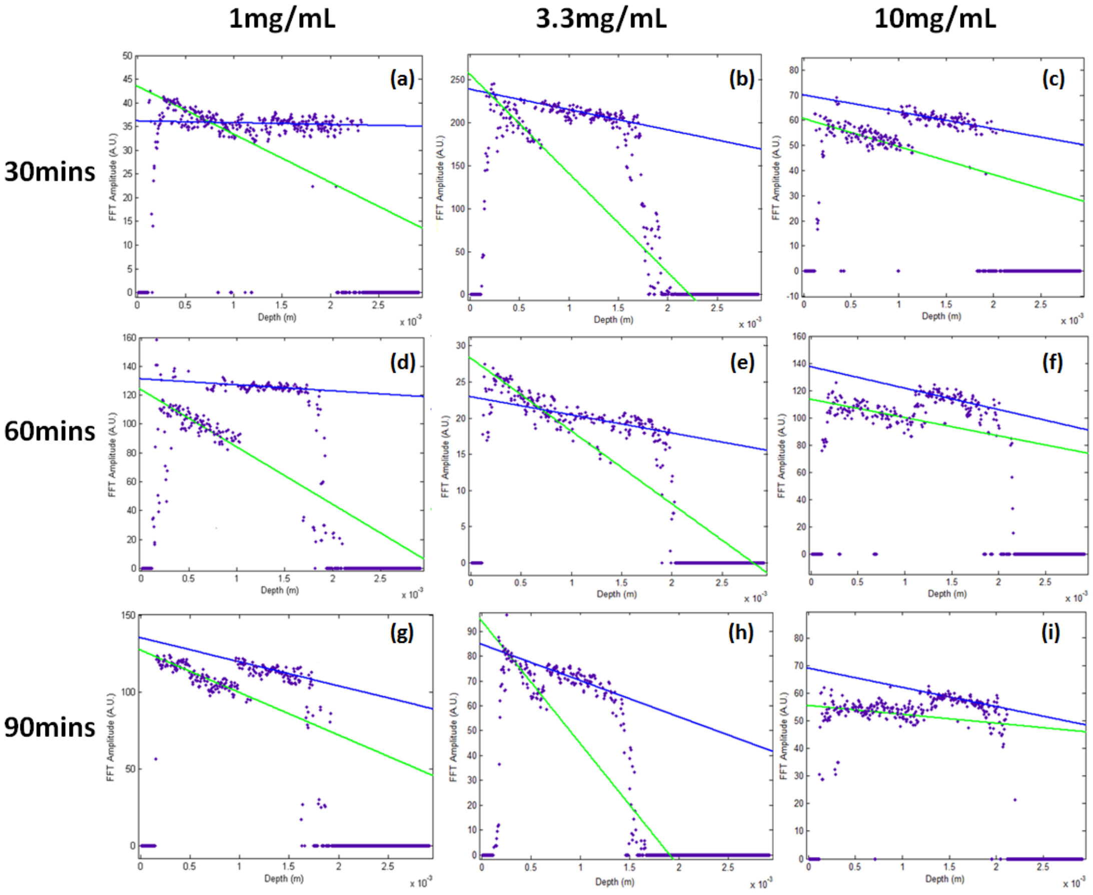

Figure 6.9 Averaged FFT amplitudes of the phase changes at different depths for the tendons treated with 1 mg/ml, 3.3mg/ml and 10mg/ml collagenase solution with 30 minutes, 60 minutes, and 90 minutes. The green and blue line are the linear model fits of ~2% agar-agar phantom and the tendon with 95% confidence bounds.

Figure 6.10 shows the overall Young's modulus changes of collagenase treated tendon samples with different incubation times and concentrations, and the quantitative Young's modulus is summarised in Table 6.2. As expected, the Young's modulus of tendon tissue is decreased as a function of collagenase digestion. Higher concentration of collagenase and longer treatment time led to a larger Young's modulus decrease.

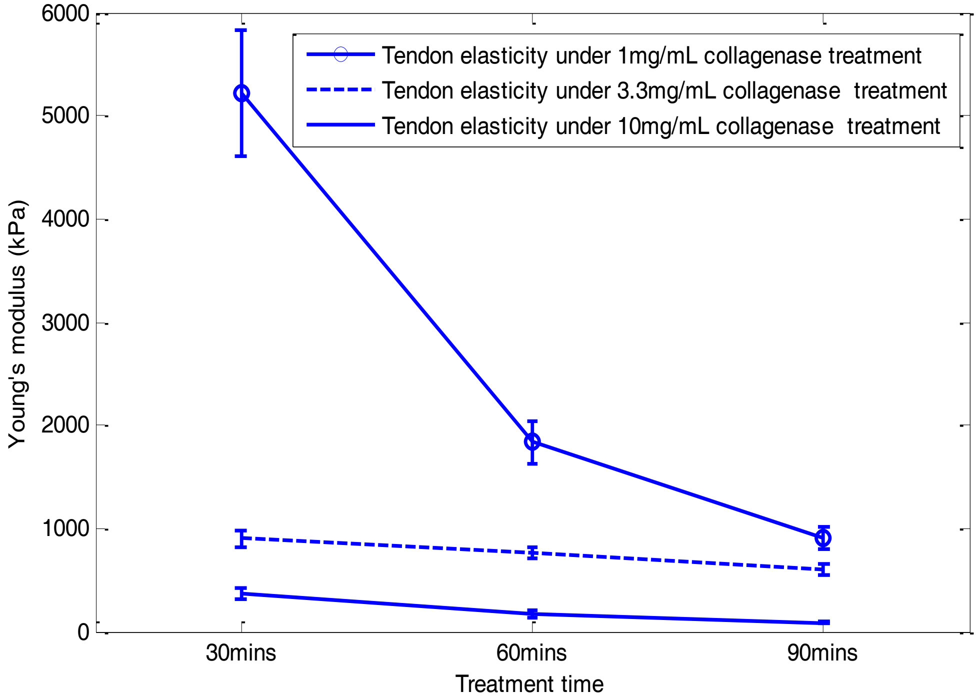

Figure 6.10 Overall Young's modulus changes of collagenase treated tendon samples with different time span and different concentrations

Table 6.2 Summary of collagenase treated tendon Young's modulus (kPa)

Control	16750.0±878.1		
Subjecting to collagenase treatment	**30 minutes**	**60 minutes**	**90 minutes**
1mg/mL	5211.9±610.3	1833.5±199.2	899.4±107.9
3.3mg/mL	895.2±84.8	724.3±52.1	602.2±55.3
10mg/mL	366.7±61.0	177.6±37.1	88.4±9.3

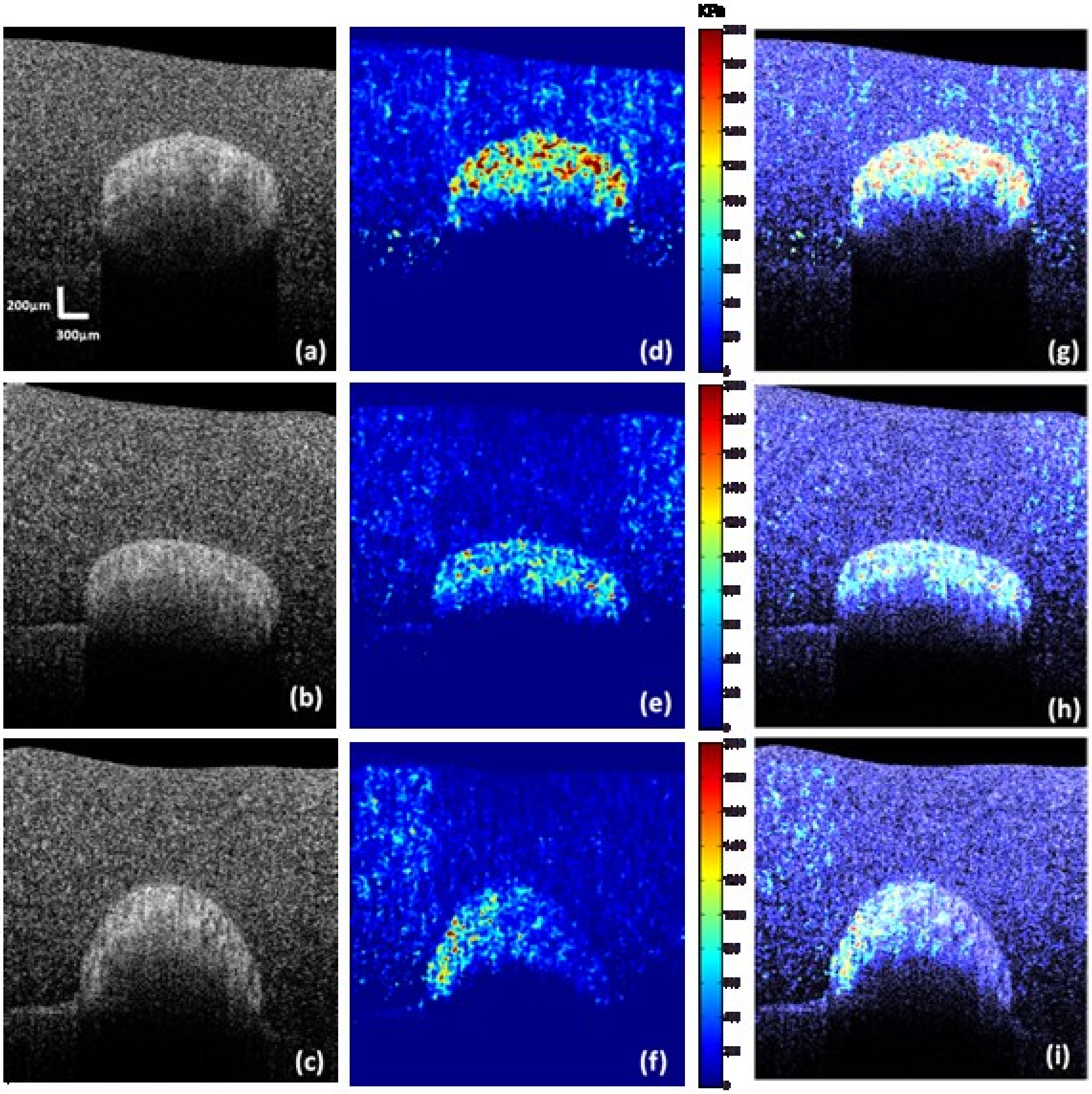

Figure 6.11 Figures (a),(b),(c) are the structure images of tendon samples treated with 1mg/mL, 3.3mg/mL and 10mg/mL collagenase for 60 minutes respectively; (d), (e), (f) are the calculated Young's modulus elastography for these three samples and the colour bars show the value in unit of KPa;(g),(h),(i) are overlaid images. (uneven parts of the tendon elastography in figure (f) could be caused by the treatment)

Figure 6.11 shows the OCT structure images, OCE images and the overlaid images of tendon samples treated with collagenase for 1mg/mL, 3.3mg/mL and 10m/mL for 60 minutes respectively. The 2D strain image was calculated based on the method developed from previous study [42]. Applying the Eq. 6-3 and using the Young's modulus value of 193kPa for the agar phantom, the strain image was converted to the OCT elastography image with absolute Young's modulus values, as shown in (d), (e), (f), instead of relative strain value as shown in Kennedy *et al.* [183] It shows that using the presented elasticity reconstruction approach based on quantitative OCE methods, quantitative elasticity images of an agar-tendon sample can be reconstructed with high resolution. A clear tendon-agar boundary can be found in the elasticity images, although the signal decreases at deeper locations. This is expected because the accuracy of the phase measurement relies on the intensity level from structure image [42].

6.7 Conclusions

A novel concept of combining dynamic elastography method and PhS-OCT to characterise and monitor the quantitative information of chicken tendons *ex vivo* is reported in this thesis. Experiments show that the method can efficiently monitor the elasticity change of the tendon due to different collagen fiber degradation. PhS-OCT is also an ideal tool to detect the vibration as it provides high SNR on tendon samples. It is able to provide the B-frame image of the sample, which may validate the thickness estimation in elastography, whilst providing the elastography of the tendon tissues. The Young's modulus measured from the presented method corresponded well with the predicted results.

A benefit of PhS-OCT based elastography, in addition to being non-invasive and non-contact, is real-time simultaneous tomographic imaging of the tendon samples. The concept reported in this paper can be developed further into a truly quantitative elastographic imaging system, which has great application value in tissue engineering to evaluate the growth of artificial tendon tissue in real-time as non-disruptive feedback for bioreactors [216]. With further development of the PhS-OCT system, this method may have great potential in real clinical diagnosis to assess the physiologic conditions of human tendons. In future work, this method can be combined with the needle probe

OCT. The insertion of an OCT probe into deep tissue will overcome the penetration limits of OCT light beam.

Chapter 7 Application of Quantitative OCE in urology

7.1 Introduction

Prostate cancer is the most common non-cutaneous malignancy in men. Digital rectal examination (DRE) and prostate specific antigen (PSA) levels in blood are the screening tests for the detection of prostate cancer. Men suspected with prostate cancer are then offered transrectal ultrasound (TRUS) guided prostate biopsies to confirm the diagnosis [217]. However, standard grey scale TRUS imaging, based on increased brightness with respect to the strength of the echo, intrinsically falls short of making a reliable differentiation between cancer and benign hyperplasia of the gland [218]. Accordingly, current TRUS imaging technology is essentially limited to measuring prostate volume and guiding needles into the alleged region of interest (ROI) as per the standard biopsy protocol, and not surprisingly has been reported to have poor diagnostic accuracy for correctly identifying cancer foci [219-221]. An ideal imaging technique should accurately locate cancer foci in the prostate. Clinically, this will reduce/preclude unnecessary biopsies, thereby reducing both cost and patient morbidity. Furthermore, accurate localization of cancerous areas within the prostate gland will have an enormous implication for focal therapy for PCa.

Prostate cancer is suspected on abnormal DRE which is a perceived differences in the stiffness of abnormal versus normal prostate tissue through rectum. In other words, suspected cancerous lesions tend to be stiffer (or harder to feel) than benign tissue. The stiffness caused by cancerous lesions could be imaged using elastography. This chapter is the clinical application of OCE technique developed in chapter 5, which overcomes the resolution limitation of MRI and ultrasound imaging. Mechanical properties of prostate tissue is estimated, while providing the ultra-high elastography with resolution of OCT images (axial resolution of ~8.9 μm and transverse resolution of ~15 μm). Building on this technological advance and experience it hypothesized that OCE can reliably differentiate benign and malignant prostate tissues with high diagnostic accuracy. Moreover, the technology could have potential in charactering different grades of prostate cancer based on the change of tissue morphology as well as mechanical properties. In doing so, this study perform 3D quantitative OCE imaging using PhS-OCT system combines with vibration induced by an electromagnetic actuator. Quantitative 3D elastography images of biopsy cores were then compared with pathology reports for cross-validation. This technique has the potential to greatly increase the utility and impact of OCE in a clinical setting, for real-time detection and characterisation of cancers.

7.2 Background knowledge of prostate

7.2.1 Structure and function

Prostate is a gonadal organ that is exclusively owned by male. It has a chestnut-like shape and is close with bladder, as shown in Figure 7.1. [222].The bottom apex of the prostate is against the urogenital diaphragm. Pubic symphysis is in front of the prostate, and behind the prostate is rectum. Therefore, the prostatic hypertrophy could be detected by touching the back of the prostate via rectum, which is called digital rectal examination. Urethral pass through the prostate, this makes urination bear the brunt when prostate got problems. Prostate is a very unique sex gland due to its both functioning endocrine and exocrine, double secretion. When prostate works as an exocrine gland, the 2 ml prostatic fluid it secreted every day is the main components of the semen. Then, the endocrine secrets the hormone called prostaglandins.

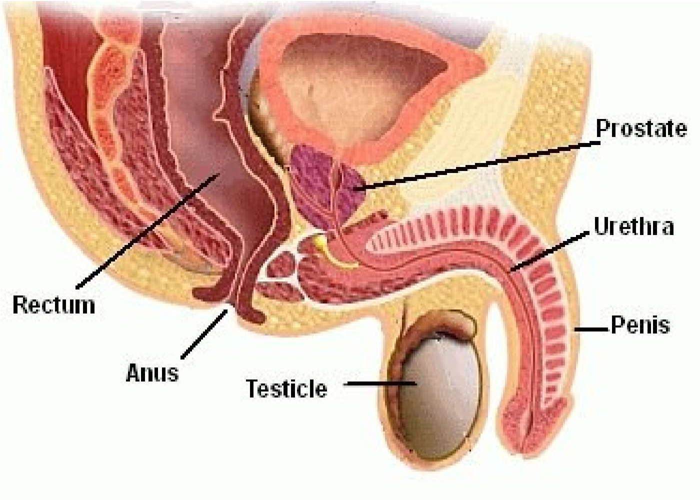

Figure 7.1 The diagram of prostate and the surrounding organs [222].

Prostate is made up by the tissue of gland, fibroblastic and smooth muscle. The upper width, vertical height and the length from front to back is about 4cm, 3cm and 2cm prospectively. Prostatic utricle is the fascia sheath that covers the surface of the prostate.

From the anatomy prospective, prostate is divided into five lobes; anterior, posterior, median and two lateral lobes. The median lobe is located between ejaculatory duct and urethra. After 40 years old, the male may has the dysuria induced by hypertrophy of prostate which pushes the bladder and compresses the urethra. One of the features of prostate is the irregular glandular cavity, and rich in elastic fibers, smooth muscle and connective tissue.

7.2.2 Prostate diseases diagnoses

7.2.2.1 Atypical small acinar proliferation (ASAP)

Atypical small acinar proliferation is a diagnosis term, more precisely than a disease [223]. It is defined as the lesion expected as malignant but the condition after microscopic examination does not meet the criteria of malignancy. The diagnostic uncertainty of the lesion comes from some confounding factors, like the size of the lesion or the numbers of the diseased acinar. The difficulty of diagnosis also brings the ASAP considerable attention. Generally, patients diagnosed with ASAP will be closely observed for a further conclusive determination. The monitoring includes periodic clinical detection, PSA testing and repeating collecting of needle biopsies in the suitable time interval. However, this accessing procedure has strong influence to either the patient or the medical personnel and the health insurance system. In view of this, pathologists have tried as clean as possible to determine the status of diseased prostate, rather than leaves blurred diagnosis of ASAP. The two approaches will be taken for the case of ASAP are more microscopic cuts for hematoxylin and eosin (H&E) staining and the immune-histochemical examination [224].

7.2.2.2 Prostatic intraepithelial neoplasia (PIN)

PIN is an abnormal cell proliferation phenomenon that is limited in the preexisted acinar and duct without indication of stromal invasion, which is also known as ‘early cancer’. PIN had been divided into three stages when it first proposed. But the reproducibility of this classification is too low to the pathologists; thereafter, it was combined and became low and high grade of PIN.

High grade concludes PIN2 and PIN3. It could be distinguished between low grade and high grade from morphology, and according to the nucleolus in nucleus to determine the high grade PIN (HGPIN). However, this definition is still inadequate in accuracy. There are varies reasons induce the uncertainty, including the reports from pathologists and technical factors, like the quality of tissue section and so on. The incidence of HGPIN is 0-25%. The current expectation of the HGPIN incidence with the absence of cancer is around from 4 to 8%. Yet, the clinical property of HGPIN is hard to define. HGPIN is regarded as a precursor of cancer in some cases, but not in all cases.

There are some presented evidences for claiming HGPIN as a precursor lesion of cancer: the appearance of HGPIN ten years prior of the cancer. The incidence of prostate cancer as well as HGPIN is both increasing with age. In prostate, HGPIN is more common and more multifocal. HGPIN and prostate cancer are usually likely to occur at the same position in prostate, and also, some cases even showed the cancer and HGPIN were emerge from the gland together.

Although the causes of PIN remain unknown, it is sure the incidence growing with age. Even though PIN is not prostate cancer, some men with prostate cancer also have PIN indeed. But not vice versa, men with PIN do not mean getting cancer.

7.2.2.3 Prostate Cancer (PCa)

Prostate cancer is the second high cancer modality in men. One in seven man affected by prostate cancer in their life, and one in thirty-six die. The overall annual incidence is 152 men in every one hundred thousand men [225]. Prostate cancer is usually occurs at the age ranges from 65-80, and the age of 67 is the average age of diagnosed. The survival rate is relative to the diagnosis stage. 100% of survival rate in the following 5 years is reported at the local/regional stage. Yet, the survival rate is dropped significantly in the distal stage, which means the cancer cell has been spread to other organs like lymph nodes and bones, only 28% in the following 5 years.

There are no symptoms at the early stage of prostate cancer. However, when the tumor grows, urethral and bladder neck may be blocked, and more severely, acute urinary retention, hematuria and incontinence are all possibly happen. Digital rectal examination (DRE) and prostate-specific antigen (PSA) have been acknowledged as the best two diagnose tools for prostate cancer detection. PSA testing appeared at 1980s and has been approved by FDA at the mid of 1990s. But the final confirm of diagnose is still needs the prostate tissue sections though pathology verified. It is still full of controversy of comprehensive annual screening of PCa. Some of the specialists claim the over diagnosed patients will adding the amount of the people that do not need treatment. Furthermore, there are many sequelas after treatment, like sexual dysfunction, incontinence, hematuria, discomfort of rectum and hemorrhage. Nevertheless, from another perspective, if the PSA testing could screens the patients in early stage, the mortality of prostate cancer will be greatly reduced after treatment.

The man with PSA level lower than 10 ng/ml and Gleason score lower than six is regarded as low incidence of prostate cancer. The ultimate aim of preventive screening is to detect and treat prostate cancer as early as possible and thus reduce the mortality. The previously mentioned DRE could only measure the tumor in a late stage. Then the controversial point of PSA testing comes from the lack of evidence that PSA screening brings lower PCa mortality. Moreover, in fact, the normal value of PSA does not stand for the inexistence of cancer cell. A research revealed that 15% of men with normal PSA test results but actually have PCa [226]. Additionally, there are 23-42% of the PSA detected PCa patients do not have any clinical problems expected in their life time [227]. Therefore, these made the dilemma and contradiction of a comprehensive annual PCa screening; undertreatment or overtreatment toward the early stage of PCa.

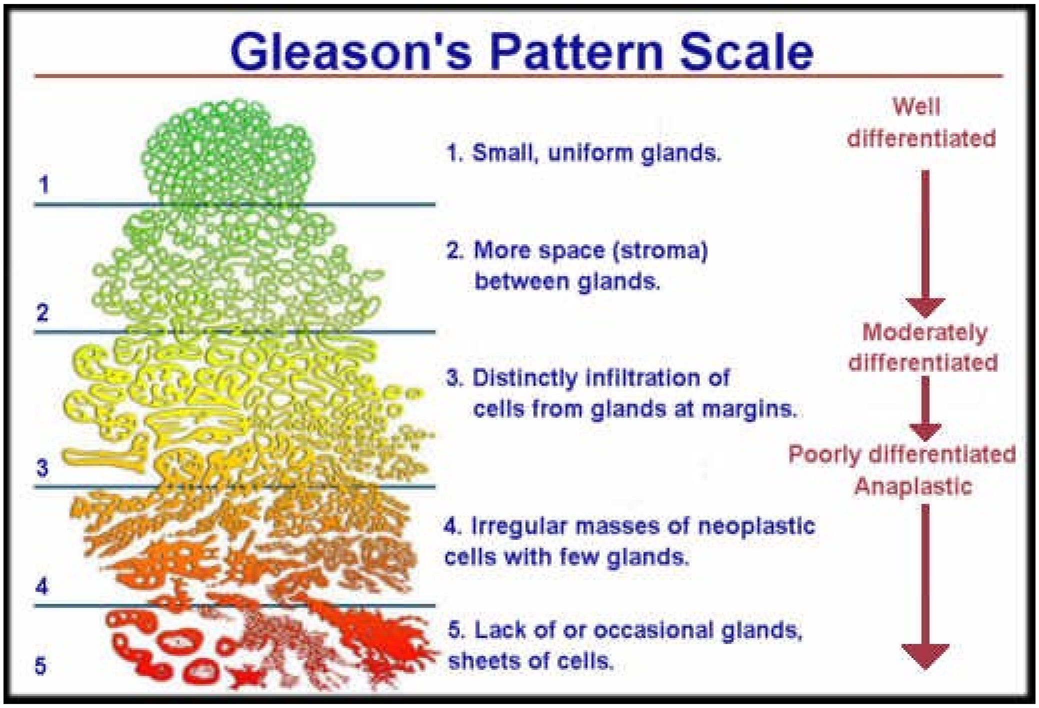
Gleason's Pattern Scale
1
2
3
4
5
1. Small, uniform glands.
2. More space (stroma) between glands.
3. Distinctly infiltration of cells from glands at margins.
4. Irregular masses of neoplastic cells with few glands.
5. Lack of or occasional glands, sheets of cells.
Well differentiated
Moderately differentiated
Poorly differentiated
Anaplastic

Figure 7.2 Gleason grading system diagram [228]

The Gleason grading system is designed for evaluate the growth speed of PCa, which is the most important value in the prostatic pathology report. When integrated with other parameters, the stage of PCa could be determined and also the strategy of treatment could be made. Gleason score based upon the result of microscopic examination, the loss of normal glandular tissue structure, for instance, the shape, size and the differentiation of the gland, as shown in Figure 7.2.

Gleason score classified PCa into 1-5, five scores. The higher the score, the more aggressive of the tumor will be, and the worse of the prognosis. There are two scores in the grading system; major and minor. The major Gleason grade represents the status expressed more than 50% in the needle core; in other words, the majority of the cancer pattern from the observation. Another pattern shown under microscopy, which less than 50% but more than 5%, then determines the minor Gleason grade. The multifocal feature of PCa highlights the importance of Gleason grading system.

Prostate cell, either normal or cancerous cell, produces the enzyme, PSA. This enzyme then secreted into semen aiming to maintain its liquid status. Additionally, there is a small amount of PSA is leaked into blood flow after secretion. PSA testing is then the measurement of PSA in blood.

7.2.3 Prostate biopsy

Prostate biopsy is a standard approach for diagnose prostate diseases, especially for PCa. It is a core needle biopsy procedure which takes only 10 to 15 mins. During the remove of the tissue, the patient will be given a local anesthesia. A transrectal ultrasound probe (TRUS) is applied in this procedure for guiding the needle to the specific position of the gland, as shown in Figure 7.3. A cylinder tissue is then be taken by urologist, which is usually in the size around 10mm in length and 1mm in diameter. 12 cores will be collected within whole prostate gland; 6 from each side. It is cleanly to see from the Figure 7.3 [229, 230], the gland is subdivided into three region; base, middle and apex. Therefore, 12 biopsies are gained and then provide the basis of Gleason score after H&E staining.

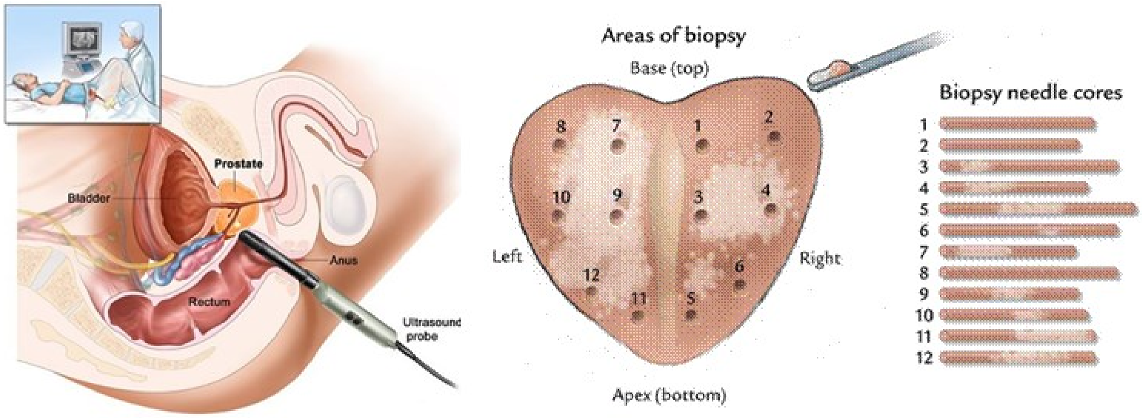
Prostate
Bladder
Anus
Rectum
Ultrasound probe
Areas of biopsy
Base (top)
8
7
1
2
10
9
3
4
Left
Right
12
6
11
5
Apex (bottom)
Biopsy needle cores
1
2
3
4
5
6
7
8
9
10
11
12

Figure 7.3 The pictures of prostate biopsy procedure and the areas of biopsy.

7.3 Material and methods

7.3.1 Patient population and sample preparation

The prospective protocol driven study was approved by local ethical committee (14/ES/0049). Informed consent for the reported experiments was obtained from all the patients before their biopsy procedures. Ten patients (age range 56-76) with suspected

PCa were recruited. In 8 men prostate cancer was suspected based on abnormal PSA value alone (T1c) while in 2 men biopsies were offered for both abnormal (T2a) DRE and high PSA. The median preoperative PSA level was 11 ng/mL (range 6.4 to 76).

All patients had standard 12 core protocol based biopsies guided by transrectal ultrasound (TRUS) from different regions of prostate gland. Overall, a total of 120 cores tissue specimens were imaged from 10 patients in this study. Specimen sizes of biopsies measured approximately 5 to 20 mm in length, and ranged from 0.8-1.2 mm in maximum diameter, mainly determined by the geometry of the 18-gauge biopsy needle.

The biopsies specimens were placed into Formalin solution immediately after the procedure and sent to the OCT laboratory. Imaging experiments were performed within 2 hours of the biopsy procedure. During the OCE scanning, the biopsy core was placed on 2% agar with a thickness of ~10 mm which acted as an elasticity reference. The OCE scanning took approximately 20 minutes for each of the biopsy specimen, which was dependant on the biopsy length. Following OCE imaging, biopsies were sent to the pathology department and processed through routine procedure for reporting by an experienced uropathologist SL) blinded to the OCE data. The statistics analysis (mean stiffness etc.) were compared with the histological characterisation by third party blinded to OCE and histology data.

The histopathology assessment characterised biopsy specimens into: benign prostate hyperplasia, acinar atypical hyperplasia (ASAP), prostatic intraepithelial neoplasia (PIN) and malignant prostate cancer. The histopathology reports were discussed in multidisciplinary meeting as a part of routine care of the participants into this study.

7.3.2 Imaging protocol

The OCE system is the same with that introduced in chapter 5. However, there are difference in imaging protocol. For the acquisition of a cross-sectional two dimensional (2D) structural and elastography image, the OCT probe beam stayed for 512 repeat during A-line scan at every spatial location sequentially within the B-scan (total 512 locations) mode while the actuator repeatedly fired the stimulus. Thus, a complete B–scan consists of 512 × 512 A-scans. The specimens were then scanned using cross-sectional imaging from one end to the other, at an intervals of 30 μm. After each imaging interval, a cross sectional elastography as well as structural image was obtained for the generation of 3D structural and elastography of biopsy sample. This minimized acquisition time and ensured that each pair of structural and elastography images were recorded from the same region of tissue.

OCE B-scans at each y position of biopsy core were generated using the technique described above with 30 μm intervals. The total acquisition time for a 3D OCE data set was 3 min for images with dimensions (xyz) of 3.5 mm × 2 mm × 2 mm. After the data acquisition of one data set, the transitional stage was moved 2mm in y direction for another acquisition, until the whole biopsy core was scanned. The raw structural and elasticity data sets were processed and imported into Amira and reconstructed into 3D data sets at full resolution. A threshold of 300 kPa was set to visualise the 3D elastography of prostate biopsy, in order to minimise the background noise.

7.3.3 Static analysis

The primary outcomes were reliability of quantitative OCE in differentiating benign and malignant prostate tissues and determining sensitivity and specificity of this technology. Young's modulus (kPa) estimated from 120 biopsy cores by OCE system was compared between malignant and benign tissues. Sensitivity, specificity, positive and negative predictive values, and AUC from ROC curve were calculated using SPSS (Chicago, IL, USA). Differences between the gropus were assessed using the Mann-Whitney test. P values<0.05 were condidered to be statistically significant.

7.4 Results

7.4.1 2D and 3D elastography of prostate biopsies

Figure 7.4 (1a, 1b and 1c) presents the structural image, elastogram and the overlaid images of benign prostate tissue. A clear biopsy-agar-air boundary can be seen in the elasticity images although intensity of the signals decreases at deeper locations. This is expected because the accuracy of the phase measurement relies on the intensity level of structure image. Figure 7.4 (2a, 2b and 2c) presents the structural, elastogram and the histology photos of prostate atypical small acinar proliferation (ASAP). There are subtle differences of structural images between benign and ASAP tissue, which were confirmed by histologic phenotype. The difference between the two is more obvious in elastograms. Evidently, prostate atypical hyperplasia has lower stiffness than normal prostate tissue biopsies. The Young's moduli of atypical small acinar proliferation are surmised in Table 7.1. Although lower in stiffness, there are still significant overlap with the benign prostate tissues.

Figure 7.4 (3-6) compares prostatic intraepithelial neoplasia (PIN), malignant prostate cancer with Gleason score of 4+3, 4+4 and 4+5. There are significant differences of elastograms as seen in Figures (Figure 7.1 (3b-6b)). There is a trend that shows Young's modulus of biopsy is increasing with the increasing Gleason grade, which is further summarised in Table 7.1.

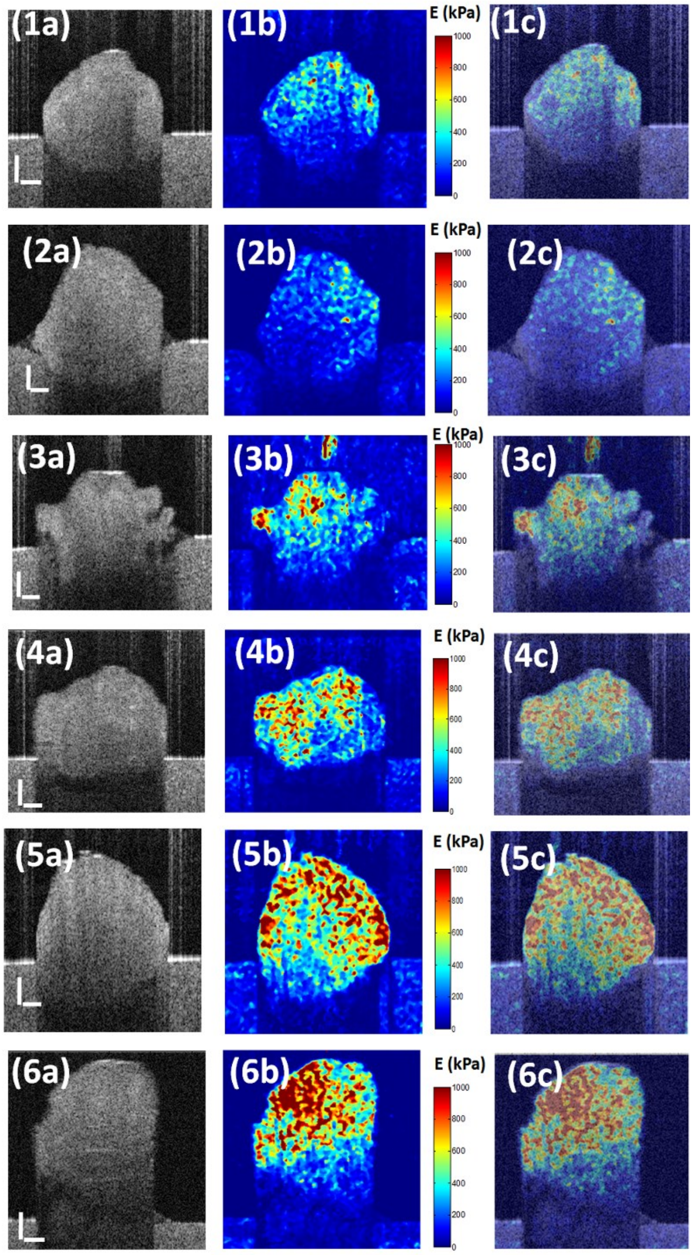
(1a)
(1b)
E (kPa)
1000
800
600
400
200
0
(1c)
(2a)
(2b)
(2c)
(3a)
(3b)
(3c)
(4a)
(4b)
(4c)
(5a)
(5b)
(5c)
(6a)
(6b)
(6c)

Figure 7.4 (a) Cross sectional structural image (b) the corresponding calculated Young's modulus elastography and (c) overlaid images of structural and elastograms of 1: benign prostate tissue, 2: atypical small acinar proliferation, 3: prostatic intraepithelial neoplasia (PIN), 4: malignant prostate cancer with Gleason score of 4+3, 5: prostate cancer with Gleason score of 4+4 and 6: prostate cancer with Gleason score of 4+5. The color bars show the Young's modulus value in unit of kPa, the scale is 250µm

Table 7.1 Summarised Young’s modulus of different category of prostate biopsies

Biopsy category		**Number of cores**	**Young’s modulus (kPa)**		
			Range (lowest to highest)	Average	Standard deviation
Normal		58	336.9-759.3	491.3	78.5
ASAP		13	224.1-672.6	383.4	80.9
PIN		3	411.2-865.7	612.6	93.4
Gleason score	3+3	6	613.3-854.1	687.3	85.5
	3+4	2	651.4-902.3	692.2	95.6
	3+5	2	684.6-848.6	703.1	72.3
	4+3	9	677.6-1058.4	769.9	108.4
	4+4	5	667.9-1157.1	799.9	110.62
	4+5	22	705.4-1779.4	968.1	171.3

3D structural and elastography images from benign and malignant PCa prostate biopsies are presented in Figure 7.5. In Figure 7.5 (a-d) and (e-h) shows the en face view of the structural, elastography, overlaid data and histological photo representing two prostate cores of benign and malignant PCa (Gleason score 3+4), respectively. Clearly as can be observed from Figure 7.5 (b) and (f), the high Young’s modulus signal is visible in the region of malignant PCa. In addition, by comparison of the elastograms to the histology photo, the percentage of cancerous area can be predicted. The bright area in Figure 7.5 (f) matches with the histological photo in Figure 7.5 (h) which indicated that about 40% of the biopsy core has the cancer involvement.

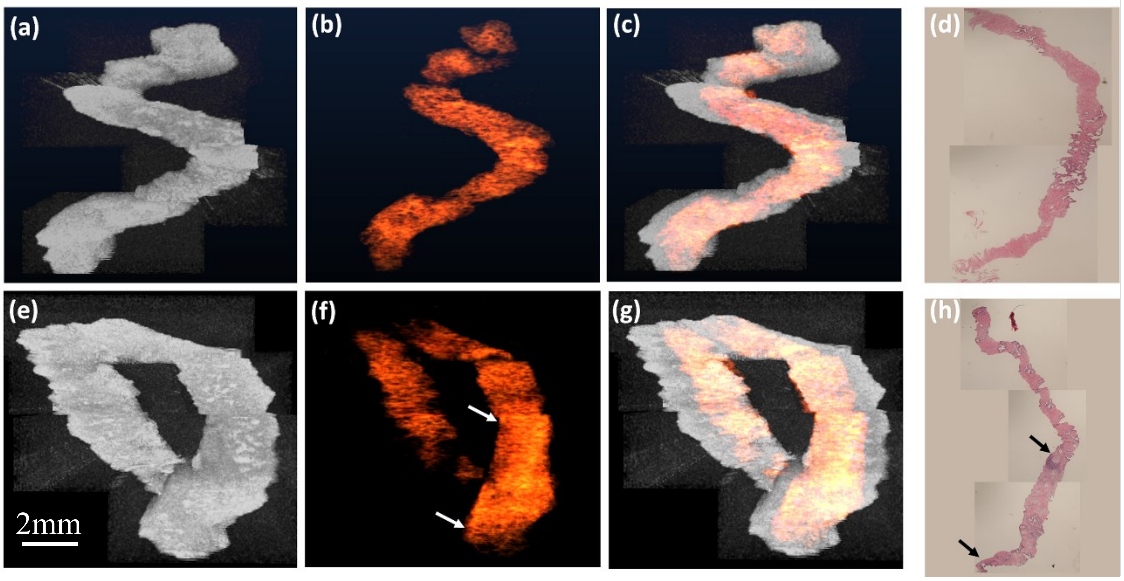

Figure 7.5 3D visualization of benign and PCa (Gleason score 3+4 with cancer involvement 40%) prostate biopsies. (a, e) OCT structural image, (b, f) OCE, (c, g) overlay from en face view and (d, h) corresponding histology photo. The arrows in (f and h) indicate the beginning and end of malignancy.

7.4.2 Diagnostic accuracy of OCE

The Young's modulus of prostate biopsy specimens is summarised in Table 7.1. This value for benign tissues serves as a reference to determine the abnormal/diseased tissue. A separate comparison of the mean Young's modulus values of PCa with individual categories of the patients in the benign group (i.e., with normal parenchyma, chronic inflammation and brisk active chronic prostatitis) was not statistically significant. The Young's modulus obtained from this study is higher than literature [231, 232], it is because the prostate is prepared in 10% Formalin solution instead of saline solution. Formalin is well known in fixing tissues and thereby significantly increases the stiffness of tissues. However, the relative stiffness difference between benign and malignant tissues should remain unaltered.

The statistical analysis utilised three different methods for the statistical analysis: 1) compare the maximum Young's modulus of each biopsy core; 2) compare the average Young's modulus of each biopsy core and 3) compare the data points with Young's modulus higher than 600 kPa (by the comparison of elasticity data and the corresponding histological report, it is found that the suspected PCa has the Young's modulus higher than 600 kPa). Results from statistical analysis PCa, benign prostate tissue and PIN are illustrated and compared in a whisker plot in Figure 7.6. Clearly from these figures, significant increasing of stiffness can be observed (*p* < 0.001) between benign prostate tissue and PCa. The Young's modulus of PIN shows higher than benign and smaller than PCa. However, there are limited samples which diagnosis as PIN. Thus more data are necessary for a convictive results against the analysis of PIN.

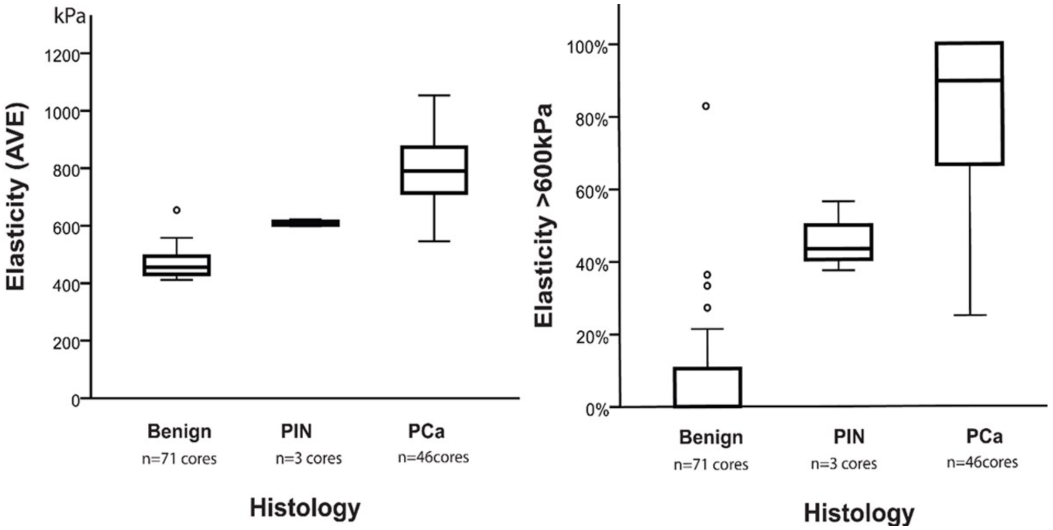

Figure 7.6 Whisker plot showing relationship of Young's modulus (kPa) with pathological outcomes using (left) threshold method and (right) average method.

The ROC analysis plot, Figure 7.7, evaluated the ability of quantitative OCE to diagnose PCa using above mentioned two statistical analysis methods. The area under the ROC curve was calculated to be >99%. Among the curves the analysis of maximum Young's modulus has the highest AUC (100%) which shows promising high ability of OCE for the diagnosis of PCa. The threshold method (comparison of all data points that higher than 600 kPa) has the lowest AUC but still high (99.2%). Data analysed showed that the sensitivity and specificity of OCE for PCa detection were 0.98 and 0.91, respectively. In addition, the positive and negative predictive values calculated for this technique are 0.85 and 1.

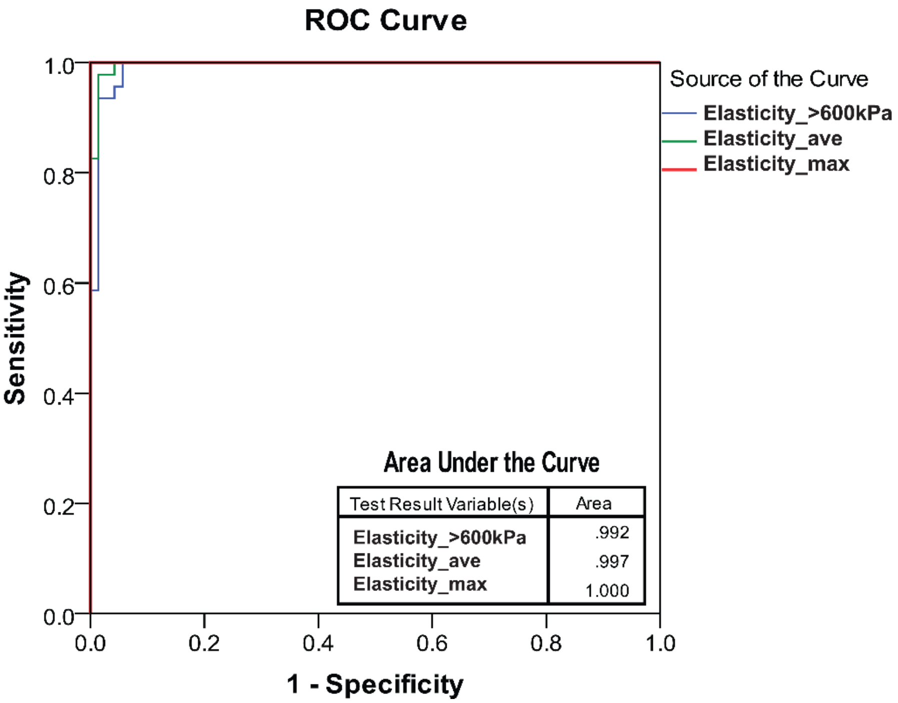

Figure 7.7 ROC curve of PCa vs. benign using three different statistical analysis methods.

Using 3D elastography the OCE system can predict the percentage of cancer involvement of prostate biopsy cores. Figure 7.8 compare the percentage of PCa predicted from quantitative OCE and histology report. Here the percentage of all data points which has Young’s modulus that higher than 600 kPa were calculated. The results show that OCE is able to provide the accurate cancer involvement since all the data points are close to the red line in Figure 7.5 which indicates the 100% match between OCE and histology results.

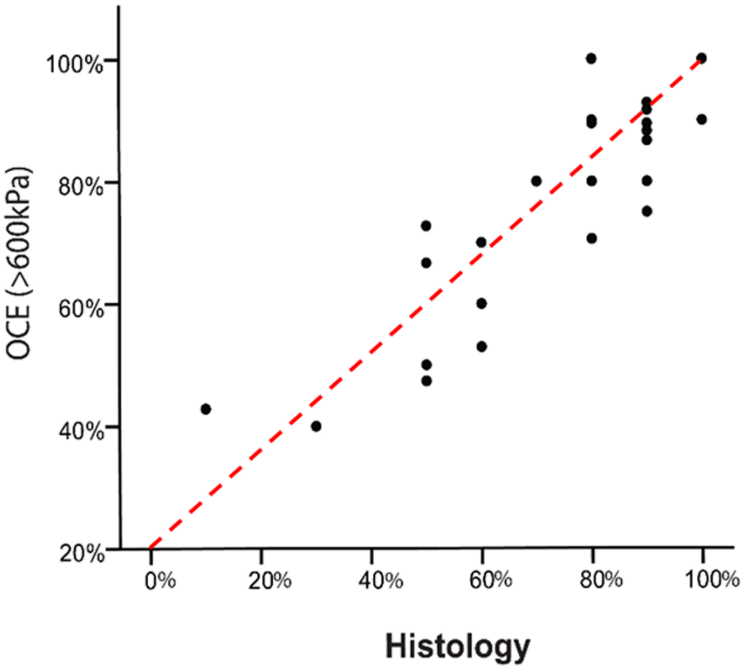

Figure 7.8 Comparison of cancer involvement predicted by OCE and histology.

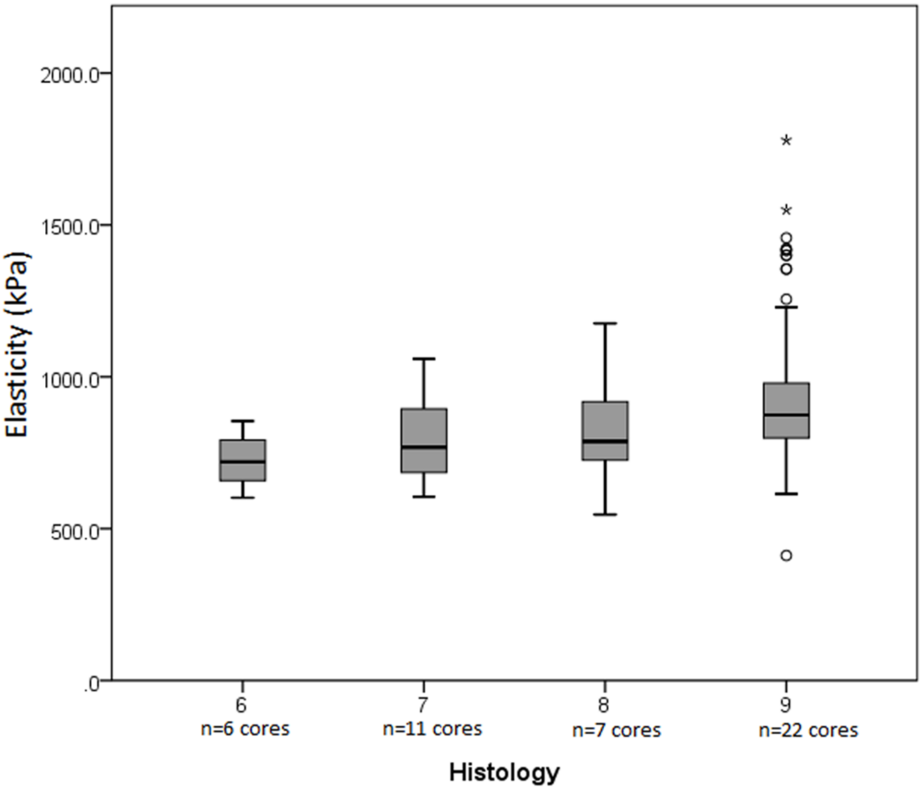

Figure 7.9 Whisker plot showing relationship of Gleason score with Young's modulus (kPa) value.

The relationship between Gleason score and the estimated Young's modulus are compared in Figure 7.9. The presence of higher Gleason scores in the histopathology results is a clinical significance and influences the decision making of the individual patient. Except for Gleason score 7 and 8 (p value = 0.365), there were significant differences between Young's modulus estimated by OCE between different Gleason scores (p Value < 0.001).

7.5 Discussion

This study represents the first attempt to estimate mechanical properties of tissues using an ultra-high resolution OCE system. In contrast to relative strain value reported by Kennedy et al. [183, 233], it shows that using the presented elasticity reconstruction approach based on OCE methods, quantitative elasticity images of a prostate biopsy sample can be reconstructed with a high resolution. Freshly obtained prostate specimens were imaged in a blinded manner to the histological reports and tissue stiffness was used to categorise specimen into different histological classification. Compared with the other techniques which can achieve elasticity measurement of prostate gland (summarised in Table 6.2), OCE shows a high diagnostic accuracy (with AUC > 0.99) of classification of normal and cancerous tissues in *ex-vivo* setting. Bases on these findings, the observation merits further research into methods of obtaining this information in an *in vivo* clinical setting.

Table 7.2 Comparison of AUC between prostate elasticity measurement methods

Reference	**Method**	**AUC (ROC)**
Correas *et al.* [222]	Ultrasound shear wave elastography	0.93
Zheng *et al.* [223]	Virtual touch tissue quantification	0.86
Zhang *et al.* [224]	TRTE (transrectal real-time tissue elastography)	0.85
	TRTE + TRUS (conventional transrectal ultrasonography)	0.84
Aboumarzouk *et al.* [223]	Transrectal elastosonography	0.86
Palmeri *et al.* [234]	Acoustic radiation force-based elasticity imaging	0.90
Teng *et al.* [229]	Transrectal sonoelastography	0.77
Tang *et al.* [230]	Transrectal real-time tissue elastography	0.90
Halpern *et al.* [231]	Shear wave elastography	0.64

The technological novelty and advancements of science in this work includes the use of a functional high resolution optical imaging modality, OCE based on combining conventional OCT with the detection of vibration amplitude (surrogate markers of mechanical properties) of the tissues. Elastograms obtained using OCE were compared with the standard histopathology processing as a reference standard for the estimation of diagnostic accuracy of the technique. The results suggest that current OCE system has a potential to distinguish a range of prostate malignancy. The stiffness of cancer foci was approximately 39.9 % higher than benign tissues with corresponding stiffness values of 687.2 ± 85.5 kPa vs. 491.3 ± 78.5 kPa, respectively. Thus, it indicates OCE can be a very promising tool for prostate cancer detection since it shows relatively high sensitivity and specificity in malignant prostate diseases.

The structural images of prostate biopsies did not show significant difference between different pathologies, which is limited by the objective lens of current system. It is 30 mm focal length that makes the system low in lateral resolution. The employment of microscope objective lens is likely to improve the imaging resolution to 1-2 μm for detailed structural image of samples.

Several conclusions regarding the relative capabilities of OCE for structural and functional imaging of prostate tissues can be drawn from these experiments. In application of photonic techniques in tissue characterisation, light scatters due to heterogeneity in the refraction index of different cells. This scattering alone, however cannot replace histology as a modality of confirming diagnosis despite a significant improvement in resolution. Addition of functional information such as measurement of tissue stiffness could enhance the ability of high resolution techniques in providing an answer. This may take us closer to obtaining an *in situ* pathology of the suspected area in patients. Delineation of tissue types based on these OCE images and features points that this may be possible. The overall information obtained using OCE is not only of high resolution images but also quantitative information which can discriminate between a ranges of pathological lesions.

The major technical limitation at this point, however, is the penetration depth of OCE system. The nature of OCT limits itself to a maximum imaging depth of 3mm. In this circumstance the utility of OCT/OCE in vivo remains a challenge. Despite this, however, the potential clinical utilities of this device remain significant. With current improvement of OCT techniques, the development of OCT needle probe makes imaging of deep tissue possible. Although OCE in needle probe is still unavailable for the 2D or 3D elastogram, it will be promising to develop such system for real clinical use in the future.

This study has shown an increasing trend of Young's modulus of prostate tissues with increasing Gleason grade of prostate cancer. However, whether OCE can reliably predict the grade of cancer especially in characterisation of "significant disease" or "indolent" requires further evaluation. Further studies with a larger number of cases are therefore required to determine the exact relationship between the Young's modulus values and tumour grade.

7.6 Conclusions

This chapter is successively verified the OCE system is a highly reliable modality for detecting the abnormal prostate tissue. The conclusions which have been made are as follows.

First of all, it could be cleanly identified varies types of diseased prostate tissue (PIN, ASAP, PCa) though the merged images of elastogram and structural images. The different degreases of disease tissues demonstrate different stiffness under elastogram. Also, the cancerous regions determined by 3D elastogram and histology matched well. After screening the whole prostate biopsy, the distribution of Young's modulus within the tissue could be mapped. And then, in contrast to the histology results, it has a good matching with the lesions.

Furthermore, the capability of OCE to measures the percentages of PCa in biopsy cores has approved by comparison with histology results. There is little disparity between the OCE and histological results in detecting cancerous areas. The ultra-high resolution of OCT makes it possible that the modality designed in this study as an alternative way to diseased extent in prostate biopsy. Moreover, the differences between Gleason scores also bring the significant differences of Young's modulus measured from OCE. Although not every interval between Gleason scores have a significant difference, the capability of OCE as a grading system of prostate cancer is still undoubtedly.

Chapter 8 Conclusions and Further Work

8.1 Summary

This project aims to develop a high sensitive PhS-OCT system to detect micro-motions and vibrations introduced by external stimuli. Presented here are two applications of PhS-OCT combining micro-motions including: 1) Photo-thermal OCT (PT-OCT) system is developed to detect the photo-thermal phenomenon. A mathematics model is proposed to analyse and reconstruct the distribution of dye in phantoms. Animal experiments were performed to study the application of PT-OCT on nano-particles detection in biological tissues. 2) A quantitative 3D optical coherence elastography (OCE) system and algorism are developed to analysis the mechanical property of tissue. Based on this technology, PhS-OCT combining micro-motion/vibration is used for the diagnosis and detection prostate cancer (PCa). The ultra-high resolution of tissue structure image can also be obtained beside the function images.

In chapter 3, the development of Doppler function OCT was reviewed as the theory base of micro motion detection by PhS-OCT. Traditional one camera spectral domain OCT was introduced and a dual camera PhS-OCT system was developed to enhance the scanning speed and phase sensitivity.

Chapter 4 provides an overview of PT-OCT, include background, detailed system set-up, data acquisition and processing algorisms. A unique mathematic model is first demonstrated to reconstruct optically absorbing compound concentrations as a function of depth and verified by experiment on single and double layers agar phantoms.

In chapter 5, the application of PT-OCT on nanoparticles concentration and distribution detection is studied. Firstly a gold based multifunctional nanoprobe was manufactured. Then the distribution in agar phantom was measured and compared with other control samples. Then animal experiment was performed to imaging nanorods uptake in sentinel lymph node of mice in situ.

Chapter 6 presents an overview and currently measurement methods of mechanical properties. A quantitative two dimensional optical coherence tomography (OCE) method is developed as a second application of PhS-OCT combine micro-motion. The theory of quantitative OCE is introduced in detail along with the system set-up and data processing algorithm. Double layers agar phantom and chicken tendon measurements is carried as fundamental characterization technique of OCE.

An application of quantitative OCE on clinic is carried in chapter 7. Three dimensional canning protocol is performed to achieve the 3D elastography image of biopsies of men with suspected prostate cancer which could provide direct visualization of the tissue stiffness for ease of biomedical diagnosis. The results were compared with pathology reports for cross-validation and statistical analysis.

8.2 Conclusions

This project demonstrates the study to prove the feasibility of using PhS-OCT to detect micro-motions and vibrations. Two functional OCT (PT-OCT and OCE) based on it is studied in detail. The following conclusions can be summarised:

- Among different imaging modalities such as ultrasound and MRI imaging, optical imaging has great potential in detection of micro-motions and vibrations in bio-tissues. PhS-OCT is a non-invasive imaging technique which has ultra-high resolution (1-10μm) and phase sensitivity (~0.01 rad) is a promising tool for detection of micro-motions in bio-tissues;
- Dual camera OCT system can double the scanning speed, which is important for the in vivo applications where the subject movement is inevitable, and enhance the capability of measure smaller phase change, consequently smaller motions can be detected. And this concept can be extended to triple or even more spectrometers OCT system;
- PT-OCT can be developed by combining the PhS-OCT and a pumping laser. A model that describes the photothermal signal as a function of depth has been developed which could be used to reconstruction the PT image to achieve depth resolved compounds concentration mapping;
- PT-OCT can be applied for medical applications such as monitoring nanoprobe uptake in sentinel lymph nodes;
- Quantitative OCE method is developed by compare the strain of known Young's modulus median and target sample. It characterise and monitor the quantitative information of chicken tendons *ex vivo*.

- 3D quantitative OCE can provide the 3D elastography of bio-tissues, which could be helpful for the diagnosis and treatment of mechanical property change related diseases. The clinic trial on biopsies of men with suspected prostate cancer shows this technic could be cleanly identified varies types of diseased prostate tissue (PIN, ASAP, PCa). It is capable to measures the percentages of PCa in biopsy cores as well.

8.3 Future work

The work presented here shows the capability of PhS-OCT for the detection of micro-motions and vibrations; Dual camera PhS-OCT development and two functional OCT (PT-OCT and OCE) which are based on it. There are several straightforward studies and developments which would be logical next steps.

PhS-OCT System development

Extend the concept of dual-spectrometer system to multi-spectrometers system for specific experiment where scanning speed is essential i.e. rapid survey of large tissue volumes as well as increasing the imaging throughput; Multi-frame averaging or acquisition of high-pixel-density images to improve image quality or reduce speckle; In-vivo measurement to reduce the bulk motion effect of patient or animal.

For PT-OCT

The model describes the photothermal signal as function of depth has been developed and the parameters of it have empirically derived using homogeneous single layer phantoms. However the parameters are dependent on the laser power, the photothermal compounds concentration and also the distance between the surface of sample and the zero-delay line for distances smaller than ~1mm. A more detailed model is demanded for a better understanding of this procedure and better reconstruction results. Better system set up is requested, such as monitoring the pumping laser power during the experiment, to minimize the noise in the results.

More applications based on PT-OCT need to be studied in biological area, such as using hemoglobin as the endogenous contrast agents to monitor oxyhemoglobin saturation in vivo; real-time monitoring nanoparticles' concentration and distribution in human lymph node or other disease related organs could be achieved in the future to assist disease diagnosis and treatment. This technology could also be used as a promising photo-therapy tool by using specific photothermal compounds and pumping laser.

For quantitative OCE

Further efforts are needed to improve the quantitative OCE method to be a truly quantitative elastographic imaging system without using the known material as the reference. This could be achieved by combine OCE with surface acoustic wave optical coherence elastography or shear wave optical coherence tomography. With the development of computer and optical sensor, this method may have great potential in real clinical diagnosis to assess the physiologic conditions of tissues in real time.

The well-recognized limited penetration depth of OCE remains a major challenge and hence technique alone cannot replace current imaging techniques for in situ detection of diseases. However, if combined with ultrasound needle probe as multiscale and multimodality diagnostic approach, this technique is promising to apply to clinic. The foreseeable future design of multimodality needle in combination with ultrasound should provide a multiscale imaging and potential possibility of in situ imaging of tissues. Although OCE in needle probe is still unavailable for the 2D or 3D elastogram, some preliminary reports [235] raise real possibility of such a system for real clinical use in the future.

Other applications

Other functional OCT based on the micro-motion detection could be developed, such as measuring the blood flow velocity in vivo and mapping the micro vasculature; Magneto motive optical molecular imaging could be achieved by combining the PhS-OCT, magnetic nanoparticles and excitation magnetic field.

References:

1. T. Rago et al., "Elastography: New developments in ultrasound for predicting malignancy in thyroid nodules," *J Clin Endocr Metab* **92**(8), 2917-2922 (2007).
2. D. L. Cochlin, R. H. Ganatra, and D. F. R. Griffiths, "Elastography in the detection of prostatic cancer," *Clin Radiol* **57**(11), 1014-1020 (2002).
3. A. P. Sarvazyan et al., "Shear wave elasticity imaging: A new ultrasonic technology of medical diagnostics," *Ultrasound Med Biol* **24**(9), 1419-1435 (1998).
4. A. Evans et al., "Quantitative shear wave ultrasound elastography: initial experience in solid breast masses," *Breast Cancer Res* **12**(6), (2010).
5. L. H. V. Wang, and S. Hu, "Photoacoustic Tomography: In Vivo Imaging from Organelles to Organs," *Science* **335**(6075), 1458-1462 (2012).
6. J. J. Yao et al., "Noninvasive Photoacoustic Computed Tomography of Mouse Brain Metabolism In Vivo," *Proc Spie* **8581**((2013).
7. Y. Wang, C. H. Li, and R. K. Wang, "Noncontact photoacoustic imaging achieved by using a low-coherence interferometer as the acoustic detector," *Opt Lett* **36**(20), 3975-3977 (2011).
8. C. H. Yang et al., "Gold nanoparticle superstructures with enhanced photothermal effect," *Crystengcomm* **15**(17), 3490-3497 (2013).
9. X. H. Huang et al., "Plasmonic photothermal therapy (PPTT) using gold nanoparticles," *Laser Med Sci* **23**(3), 217-228 (2008).
10. S. T. Wang et al., "Photothermal Effects of Supramolecularly Assembled Gold Nanoparticles for the Targeted Treatment of Cancer Cells," *Angew Chem Int Edit* **49**(22), 3777-3781 (2010).
11. E. Veuillet, L. Collet, and R. Duclaux, "Effect of Contralateral Acoustic Stimulation on Active Cochlear Micromechanical Properties in Human-Subjects - Dependence on Stimulus Variables," *J Neurophysiol* **65**(3), 724-735 (1991).
12. H. M. Subhash et al., "Volumetric in vivo imaging of intracochlear microstructures in mice by high-speed spectral domain optical coherence tomography," *J Biomed Opt* **15**(3), (2010).
13. H. M. Subhash et al., "Volumetric in-vivo imaging of intra-cochlear microstructures and microvascular perfusion in mice using high-speed spectral domain optical coherence tomography and ultra-high sensitive optical microangiography," *Optical Coherence Tomography and Coherence Domain Optical Methods in Biomedicine Xv* **7889**((2011).
14. H. M. Subhash et al., "Volumetric In Vivo Imaging of Microvascular Perfusion Within the Intact Cochlea in Mice Using Ultra-High Sensitive Optical Microangiography," *Ieee T Med Imaging* **30**(2), 224-230 (2011).
15. S. M. Dudea et al., "Value of ultrasound elastography in the diagnosis and management of prostate carcinoma," *Medical ultrasonography* **13**(1), 45-53 (2011).
16. S. K. Venkatesh et al., "MR elastography of liver tumors: Preliminary results," *Am J Roentgenol* **190**(6), 1534-1540 (2008).
17. D. Huang et al., "Optical coherence tomography," *Science* **254**(5035), 1178-1181 (1991).

18. K. Grieve et al., "Ocular tissue imaging using ultrahigh-resolution, full-field optical coherence tomography," *Investigative ophthalmology & visual science* **45**(11), 4126-4131 (2004).
19. K. Grieve et al., "In vivo anterior segment imaging in the rat eye with high speed white light full-field optical coherence tomography," *Optics express* **13**(16), 6286-6295 (2005).
20. C. H. Li et al., "Determining elastic properties of skin by measuring surface waves from an impulse mechanical stimulus using phase-sensitive optical coherence tomography," *J R Soc Interface* **9**(70), 831-841 (2012).
21. A. T. Yeh et al., "Imaging wound healing using optical coherence tomography and multiphoton microscopy in an in vitro skin-equivalent tissue model," *J Biomed Opt* **9**(2), 248-253 (2004).
22. W. Tan et al., "Structural and functional optical imaging of three-dimensional engineered tissue development," *Tissue engineering* **10**(11-12), 1747-1756 (2004).
23. Y. Yang et al., "A naturally occurring contrast agent for OCT imaging of smokers' lung," *J Phys D Appl Phys* **38**(15), 2590-2596 (2005).
24. P. O. Bagnaninchi et al., "Monitoring tissue formation and organization of engineered tendon by optical coherence tomography - art. no. 608419," *Optical Interactions with Tissue and Cells XVII* **6084**(8419-8419 (2006).
25. H.-W. Wang, and Y. Chen, "Clinical applications of optical coherence tomography in urology," *IntraVital* **3**(1), e28770 (2014).
26. D. J. Margolis et al., "Prevalence of Diabetes, Diabetic Foot Ulcer, and Lower Extremity Amputation Among Medicare Beneficiaries, 2006 to 2008: Data Points #1," in *Data Points Publication Series*, Rockville (MD) (2011).
27. I.-K. Jang et al., "Visualization of coronary atherosclerotic plaques in patients using optical coherence tomography: comparison with intravascular ultrasound," *J Am Coll Cardiol* **39**(4), 604-609 (2002).
28. Y. Zhao et al., "Phase-resolved optical coherence tomography and optical Doppler tomography for imaging blood flow in human skin with fast scanning speed and high velocity sensitivity," *Optics letters* **25**(2), 114-116 (2000).
29. R. K. Wang, and L. An, "Doppler optical micro-angiography for volumetric imaging of vascular perfusion in vivo," *Optics express* **17**(11), 8926-8940 (2009).
30. J. F. de Boer et al., "Two-dimensional birefringence imaging in biological tissue by polarization-sensitive optical coherence tomography," *Optics letters* **22**(12), 934-936 (1997).
31. U. Morgner et al., "Spectroscopic optical coherence tomography," *Opt Lett* **25**(2), 111-113 (2000).
32. F. E. Robles et al., "Molecular imaging true-colour spectroscopic optical coherence tomography," *Nature photonics* **5**(12), 744-747 (2011).
33. R. K. Wang, and A. L. Nuttall, "Phase-sensitive optical coherence tomography imaging of the tissue motion within the organ of Corti at a subnanometer scale: a preliminary study," *J Biomed Opt* **15**(5), (2010).
34. M. A. Choma et al., "Spectral-domain phase microscopy," *Opt Lett* **30**(10), 1162-1164 (2005).

35. C. Joo et al., "Spectral-domain optical coherence phase microscopy for quantitative phase-contrast imaging," *Opt Lett* **30**(16), 2131-2133 (2005).
36. M. V. Sarunic, S. Weinberg, and J. A. Izatt, "Full-field swept-source phase microscopy," *Opt Lett* **31**(10), 1462-1464 (2006).
37. D. C. Adler, R. Huber, and J. G. Fujimoto, "Phase-sensitive optical coherence tomography at up to 370,000 lines per second using buffered Fourier domain mode-locked lasers," *Opt Lett* **32**(6), 626-628 (2007).
38. D. C. Adler et al., "Photothermal detection of gold nanoparticles using phase-sensitive optical coherence tomography," *Opt Express* **16**(7), 4376-4393 (2008).
39. R. K. K. Wang, S. Kirkpatrick, and M. Hinds, "Phase-sensitive optical coherence elastography for mapping tissue microstrains in real time," *Appl Phys Lett* **90**(16), (2007).
40. K. M. Hiltawsky et al., "Freehand ultrasound elastography of breast lesions: clinical results," *Ultrasound in medicine & biology* **27**(11), 1461-1469 (2001).
41. C. L. De Korte et al., "Characterization of plaque components with intravascular ultrasound elastography in human femoral and coronary arteries in vitro," *Circulation* **102**(6), 617-623 (2000).
42. G. Y. Guan et al., "Depth profiling of photothermal compound concentrations using phase sensitive optical coherence tomography," *J Biomed Opt* **16**(12), (2011).
43. C. B. Scruby, and L. E. Drain, *Laser ultrasonics techniques and applications*, CRC Press (1990).
44. S. E. Nissen, and P. Yock, "Intravascular ultrasound - Novel pathophysiological insights and current clinical applications," *Circulation* **103**(4), 604-616 (2001).
45. P. G. Yock, and P. J. Fitzgerald, "Intravascular ultrasound: State of the art and future directions," *Am J Cardiol* **81**(7A), 27e-32e (1998).
46. A. Evans et al., "Quantitative shear wave ultrasound elastography: initial experience in solid breast masses," *Breast Cancer Res* **12**(6), R104 (2010).
47. A. L. McKnight et al., "MR elastography of breast cancer: Preliminary results.," *Am J Roentgenol* **178**(6), (2002).
48. W. Drexler, and J. G. Fujimoto, "Optical Coherence Tomography Technology and Applications Preface," *Biol Med Phys Biomed* V-Vii (2008).
49. A. F. Fercher et al., "Measurement of Intraocular Distances by Backscattering Spectral Interferometry," *Opt Commun* **117**(1-2), 43-48 (1995).
50. R. Leitgeb, C. K. Hitzenberger, and A. F. Fercher, "Performance of fourier domain vs. time domain optical coherence tomography," *Opt Express* **11**(8), 889-894 (2003).
51. M. A. Choma et al., "Sensitivity advantage of swept source and Fourier domain optical coherence tomography," *Opt Express* **11**(18), 2183-2189 (2003).
52. M. R. Hee et al., "Optical Coherence Tomography of the Human Retina," *Arch Ophthalmol-Chic* **113**(3), 325-332 (1995).
53. C. K. Hitzenberger et al., "Measurement of the Axial Length of Cataract Eyes by Laser-Doppler Interferometry," *Invest Ophth Vis Sci* **34**(6), 1886-1893 (1993).
54. M. R. Hee et al., "Topography of diabetic macular edema with optical coherence tomography," *Ophthalmology* **105**(2), 360-370 (1998).

55. M. R. Hee et al., "Optical Coherence Tomography of Macular Holes," *Ophthalmology* **102**(5), 748-756 (1995).
56. M. R. Hee et al., "Optical coherence tomography of age-related macular degeneration and choroidal neovascularization," *Ophthalmology* **103**(8), 1260-1270 (1996).
57. J. Welzel et al., "Optical coherence tomography of the human skin," *J Am Acad Dermatol* **37**(6), 958-963 (1997).
58. T. Gambichler et al., "Applications of optical coherence tomography in dermatology," *J Dermatol Sci* **40**(2), 85-94 (2005).
59. S. M. Srinivas et al., "Determination of burn depth by polarization-sensitive optical coherence tomography," *J Biomed Opt* **9**(1), 207-212 (2004).
60. V. X. D. Yang et al., "Optical coherence and Doppler tomography for monitoring tissue changes induced by laser thermal therapy - An in vivo feasibility study," *Rev Sci Instrum* **74**(1), 437-440 (2003).
61. G. J. Tearney et al., "In vivo endoscopic optical biopsy with optical coherence tomography," *Science* **276**(5321), 2037-2039 (1997).
62. M. E. Brezinski et al., "Optical biopsy with optical coherence tomography: Feasibility for surgical diagnostics," *J Surg Res* **71**(1), 32-40 (1997).
63. S. A. Boppart et al., "Intraoperative assessment of microsurgery with three-dimensional optical coherence tomography," *Radiology* **208**(1), 81-86 (1998).
64. F. I. Feldchtein et al., "Endoscopic applications of optical coherence tomography," *Opt Express* **3**(6), 257-270 (1998).
65. H. Shemesh et al., "Endodontic Applications of Endoscopic Optical Coherence Tomography," *Laser Surg Med* 19-19 (2009).
66. A. M. Rollins et al., "Real-time in vivo imaging of human gastrointestinal ultrastructure by use of endoscopic optical coherence tomography with a novel efficient interferometer design," *Opt Lett* **24**(19), 1358-1360 (1999).
67. W. Drexler, "Ultrahigh-resolution optical coherence tomography," *J Biomed Opt* **9**(1), 47-74 (2004).
68. T. M. Yelbuz et al., "Images in cardiovascular medicine. Approaching cardiac development in three dimensions by magnetic resonance microscopy," *Circulation* **108**(22), e154-155 (2003).
69. D. Huang, and M. Shure, "Handbook of optical coherence tomography," *Ophthalmic surgery, lasers & imaging : the official journal of the International Society for Imaging in the Eye* **34**(1), 78-79 (2003).
70. M. R. Hee et al., "Polarization-Sensitive Low-Coherence Reflectometer for Birefringence Characterization and Ranging," *J Opt Soc Am B* **9**(6), 903-908 (1992).
71. J. F. deBoer et al., "Two-dimensional birefringence imaging in biological tissue by polarization-sensitive optical coherence tomography," *Opt Lett* **22**(12), 934-936 (1997).
72. W. Drexler et al., "Correlation of collagen organization with polarization sensitive imaging of in vitro cartilage: Implications for osteoarthritis," *J Rheumatol* **28**(6), 1311-1318 (2001).

73. M. Pircher, C. K. Hitzenberger, and U. Schmidt-Erfurth, "Polarization sensitive optical coherence tomography in the human eye," *Prog Retin Eye Res* **30**(6), 431-451 (2011).
74. B. Cense et al., "Thickness and birefringence of healthy retinal nerve fiber layer tissue measured with polarization-sensitive optical coherence tomography," *Invest Ophth Vis Sci* **45**(8), 2606-2612 (2004).
75. E. Gotzinger et al., "Retinal nerve fiber layer birefringence evaluated with polarization sensitive spectral domain OCT and scanning laser polarimetry: A comparison," *J Biophotonics* **1**(2), 129-139 (2008).
76. M. Pircher et al., "Transversal phase resolved polarization sensitive optical coherence tomography," *Phys Med Biol* **49**(7), 1257-1263 (2004).
77. E. Gotzinger et al., "Imaging of birefringent properties of keratoconus corneas by polarization-sensitive optical coherence tomography," *Invest Ophth Vis Sci* **48**(8), 3551-3558 (2007).
78. C. Ahlers et al., "Imaging of the Retinal Pigment Epithelium in Age-Related Macular Degeneration Using Polarization-Sensitive Optical Coherence Tomography," *Invest Ophth Vis Sci* **51**(4), 2149-2157 (2010).
79. B. Baumann et al., "Segmentation and quantification of retinal lesions in age-related macular degeneration using polarization-sensitive optical coherence tomography," *J Biomed Opt* **15**(6), (2010).
80. J. T. Oh et al., "Quantification of the wound healing using polarization-sensitive optical coherence tomography," *J Biomed Opt* **11**(4), (2006).
81. M. Mogensen et al., "OCT imaging of skin cancer and other dermatological diseases," *J Biophotonics* **2**(6-7), 442-451 (2009).
82. N. A. Patel et al., "Monitoring osteoarthritis in the rat model using optical coherence tomography," *Ieee T Med Imaging* **24**(2), 155-159 (2005).
83. D. Fried et al., "Imaging caries lesions and lesion progression with polarization sensitive optical coherence tomography," *J Biomed Opt* **7**(4), 618-627 (2002).
84. P. Ngaotheppitak et al., "PS-OCT of Occlusal and Interproximal Caries Lesions viewed from Occlusal Surfaces - art. no. 61370L," *Lasers in Dentistry XII* **6137**(L1370-L1370 (2006).
85. J. B. Eom et al., "Ball lens based lensed patch cord probes for optical coherence tomography in the field of dentistry," *Opt Commun* **285**(21-22), 4333-4337 (2012).
86. D. C. Adler et al., "Optical coherence tomography contrast enhancement using spectroscopic analysis with spectral autocorrelation," *Opt Express* **12**(22), 5487-5501 (2004).
87. D. J. Faber et al., "Toward assessment of blood oxygen saturation by spectroscopic optical coherence tomography," *Opt Lett* **30**(9), 1015-1017 (2005).
88. D. J. Faber et al., "Oxygen saturation-dependent absorption and scattering of blood," *Physical review letters* **93**(2), (2004).
89. Z. P. Chen et al., "Optical Doppler tomographic imaging of fluid flow velocity in highly scattering media," *Opt Lett* **22**(1), 64-66 (1997).
90. V. Gusmeroli, and M. Martinelli, "Distributed Laser Doppler-Velocimeter," *Opt Lett* **16**(17), 1358-1360 (1991).

91. J. A. Izatt et al., "In vivo bidirectional color Doppler flow imaging of picoliter blood volumes using optical coherence tomograghy," *Opt Lett* **22**(18), 1439-1441 (1997).

92. R. A. Leitgeb et al., "Real-time assessment of retinal blood flow with ultrafast acquisition by color Doppler Fourier domain optical coherence tomography," *Opt Express* **11**(23), 3116-3121 (2003).

93. B. R. White et al., "In vivo dynamic human retinal blood flow imaging using ultra-high-speed spectral domain optical Doppler tomography," *Opt Express* **11**(25), 3490-3497 (2003).

94. S. Yazdanfar, A. M. Rollins, and J. A. Izatt, "Imaging and velocimetry of the human retinal circulation with color Doppler optical coherence tomography," *Opt Lett* **25**(19), 1448-1450 (2000).

95. Z. P. Chen et al., "Noninvasive imaging of in vivo blood flow velocity using optical Doppler tomography," *Opt Lett* **22**(14), 1119-1121 (1997).

96. J. A. Izatt et al., "In vivo bidirectional color Doppler flow imaging of picoliter blood volumes using optical coherence tomography," *Opt Lett* **22**(18), 1439-1441 (1997).

97. Y. H. Zhao et al., "Doppler standard deviation imaging for clinical monitoring of in vivo human skin blood flow," *Opt Lett* **25**(18), 1358-1360 (2000).

98. Y. H. Zhao et al., "Phase-resolved optical coherence tomography and optical Doppler tomography for imaging blood flow in human skin with fast scanning speed and high velocity sensitivity," *Opt Lett* **25**(2), 114-116 (2000).

99. Y. H. Zhao et al., "Three-dimensional reconstruction of in vivo blood vessels in human skin using phase-resolved optical Doppler tomography," *Ieee J Sel Top Quant* **7**(6), 931-935 (2001).

100. J. F. de Boer et al., "Improved signal-to-noise ratio in spectral-domain compared with time-domain optical coherence tomography," *Opt Lett* **28**(21), 2067-2069 (2003).

101. J. Zhang, and Z. P. Chen, "In vivo blood flow imaging by a swept laser source based Fourier domain optical Doppler tomography," *Opt Express* **13**(19), 7449-7457 (2005).

102. B. J. Vakoc et al., "Phase-resolved optical frequency domain imaging," *Opt Express* **13**(14), 5483-5493 (2005).

103. Y. H. Zhao et al., "Real-time phase-resolved functional optical coherence tomography by use of optical Hilbert transformation," *Opt Lett* **27**(2), 98-100 (2002).

104. J. S. Nelson et al., "Imaging blood flow in human port-wine stain in situ and in real time using optical Doppler tomography," *Arch Dermatol* **137**(6), 741-744 (2001).

105. H. W. Ren et al., "Imaging and quantifying transverse flow velocity with the Doppler bandwidth in a phase-resolved functional optical coherence tomography," *Opt Lett* **27**(6), 409-411 (2002).

106. S. K. Debnath, M. P. Kothiyal, and S. W. Kim, "Evaluation of spectral phase in spectrally resolved white-light interferometry: Comparative study of single-frame techniques," *Opt Laser Eng* **47**(11), 1125-1130 (2009).

107. Y. Q. Deng et al., "Wavelet-transform analysis of spectral shearing interferometry for phase reconstruction of femtosecond optical pulses," *Opt Express* **13**(6), 2120-2126 (2005).
108. M. Takeda, H. Ina, and S. Kobayashi, "Fourier-Transform Method of Fringe-Pattern Analysis for Computer-Based Topography and Interferometry," *J Opt Soc Am* **72**(1), 156-160 (1982).
109. Q. Kemao, "Windowed Fourier transform for fringe pattern analysis," *Applied optics* **43**(13), 2695-2702 (2004).
110. D. A. Zweig, and R. E. Hufnagel, "A Hilbert Transform Algorithm for Fringe-Pattern Analysis," *Advanced Optical Manufacturing and Testing* **1333**(295-302 (1990).
111. P. Sandoz, G. Tribillon, and H. Perrin, "High-resolution profilometry by using phase calculation algorithms for spectroscopic analysis of white-light interferograms," *J Mod Optic* **43**(4), 701-708 (1996).
112. B. Potsaid et al., "Ultrahigh speed 1050nm swept source/Fourier domain OCT retinal and anterior segment imaging at 100,000 to 400,000 axial scans per second," *Opt Express* **18**(19), 20029-20048 (2010).
113. T. Klein et al., "Megahertz OCT for ultrawide-field retinal imaging with a 1050nm Fourier domain mode-locked laser," *Opt Express* **19**(4), 3044-3062 (2011).
114. "Diffraction grating," http://en.wikipedia.org/wiki/Diffraction_grating
115. "1145 l/mm @ 1310nm Dickson®," http://wasatchphotonics.com/wp-content/uploads/2014/08/1145-lpmm-@-1310-nm.pdf
116. S. Yun et al., "High-speed spectral-domain optical coherence tomography at 1.3 µm wavelength," *Opt Express* **11**(26), 3598-3604 (2003).
117. "SU1024-LDH2 92 KHz InGaAs Linescan Camera," http://www.sensorsinc.com/images/uploads/documents/SU1024-LDH2.pdf
118. B. Potsaid et al., "Ultrahigh speed Spectral/Fourier domain OCT ophthalmic imaging at 70,000 to 312,500 axial scans per second," *Opt Express* **16**(19), 15149-15169 (2008).
119. H. C. Hendargo et al., "Synthetic wavelength based phase unwrapping in spectral domain optical coherence tomography," *Opt Express* **17**(7), 5039-5051 (2009).
120. J. Sell, *Photothermal investigations of solids and fluids*, Elsevier (2012).
121. D. P. Almond, and P. Patel, *Photothermal science and techniques*, Springer (1996).
122. T. Akkin et al., "Imaging tissue response to electrical and photothermal stimulation with nanometer sensitivity," *Laser Surg Med* **33**(4), 219-225 (2003).
123. K. V. Larin et al., "Phase-sensitive optical low-coherence reflectometry for the detection of analyte concentrations," *Applied optics* **43**(17), 3408-3414 (2004).
124. T. Y. Fan, and J. L. Daneu, "Thermal coefficients of the optical path length and refractive index in YAG," *Applied optics* **37**(9), 1635-1637 (1998).
125. A. H. Harvey, J. S. Gallagher, and J. M. H. L. Sengers, "Revised formulation for the refractive index of water and steam as a function of wavelength, temperature and density," *J Phys Chem Ref Data* **27**(4), 761-774 (1998).

126. B. Richerzhagen, "Interferometer for measuring the absolute refractive index of liquid water as a function of temperature at 1.064 mu m," *Applied optics* **35**(10), 1650-1653 (1996).
127. P. Schiebener et al., "Refractive-Index of Water and Steam as Function of Wavelength, Temperature and Density," *J Phys Chem Ref Data* **19**(3), 677-717 (1990).
128. I. Thormahlen, J. Straub, and U. Grigull, "Refractive-Index of Water and Its Dependence on Wavelength, Temperature, and Density," *J Phys Chem Ref Data* **14**(4), 933-946 (1985).
129. M. Takenaka, and R. Masui, "Measurement of the Thermal-Expansion of Pure Water in the Temperature-Range 0-Degrees-C-85-Degrees-C," *Metrologia* **27**(4), 165-171 (1990).
130. J. F. de Boer et al., "Imaging thermally damaged tissue by polarization sensitive optical coherence tomography," *Opt Express* **3**(6), 212-218 (1998).
131. J. M. Schmitt, "Optical coherence tomography (OCT): A review," *Ieee J Sel Top Quant* **5**(4), 1205-1215 (1999).
132. S. A. Telenkov et al., "Differential phase optical coherence probe for depth-resolved detection of photothermal response in tissue," *Phys Med Biol* **49**(1), 111-119 (2004).
133. K. Sokolov et al., "Plasmon resonance coupling of metal nanoparticles for molecular imaging of carcinogenesis in vivo," *Journal of Biomedical Optics* **12**(3), (2007).
134. S. Krishnan et al., "Modulation of in vivo tumor radiation response via gold nanoshell-mediated vascular-focused hyperthermia: Characterizing an integrated antihypoxic and localized vascular disrupting targeting strategy," *Nano Lett* **8**(5), 1492-1500 (2008).
135. K. R. Diamond, M. S. Patterson, and T. J. Farrell, "Quantification of Fluorophore Concentration in Tissue-Simulating Media by Fluorescence Measurements with a Single Optical Fiber," *Appl. Opt.* **42**(13), 2436-2442 (2003).
136. B. W. Pogue, and G. Burke, "Fiber-Optic Bundle Design for Quantitative Fluorescence Measurement From Tissue," *Appl. Opt.* **37**(31), 7429-7436 (1998).
137. M. Canpolat, and J. R. Mourant, "Monitoring Photosensitizer Concentration by use of a Fiber-Optic Probe with a Small Source-Detector Separation," *Appl. Opt.* **39**(34), 6508-6514 (2000).
138. A. Amelink et al., "In vivo quantification of chromophore concentration using fluorescence differential path length spectroscopy," *Journal of Biomedical Optics* **14**(3), (2009).
139. R. Reif et al., "Optical method for real-time monitoring of drug concentrations facilitates the development of novel methods for drug delivery to brain tissue," *J Biomed Opt* **12**(3), (2007).
140. T. C. Zhu, J. C. Finlay, and S. M. Hahn, "Determination of the distribution of light, optical properties, drug concentration, and tissue oxygenation in-vivo in human prostate during motexafin lutetium-mediated photodynamic therapy," *Journal of Photochemistry and Photobiology B: Biology* **79**(3), 231-241 (2005).

141. M. G. Ghosn, V. V. Tuchin, and K. V. Larin, "Nondestructive quantification of analyte diffusion in cornea and sclera using optical coherence tomography," *Invest Ophth Vis Sci* **48**(6), 2726-2733 (2007).

142. A. Agrawal et al., "Quantitative evaluation of optical coherence tomography signal enhancement with gold nanoshells," *J Biomed Opt* **11**(4), (2006).

143. J. G. Fujimoto et al., "Photothermal detection of gold nanoparticles using phase-sensitive optical coherence tomography," *Optics Express* **16**(7), 4376-4393 (2008).

144. R. V. Kuranov et al., "Depth-resolved blood oxygen saturation measurement by dual-wavelength photothermal (DWP) optical coherence tomography," *Biomed Opt Express* **2**(3), 491-504 (2011).

145. A. S. Paranjape et al., "Depth resolved photothermal OCT detection of macrophages in tissue using nanorose," *Biomed Opt Express* **1**(1), 2-16 (2010).

146. T. E. Milner, J. Kim, and J. Oh, "Measurement of optical path length change following pulsed laser irradiation using differential phase optical coherence tomography," *Journal of Biomedical Optics* **11**(4), (2006).

147. H. H. Richardson et al., "Experimental and Theoretical Studies of Light-to-Heat Conversion and Collective Heating Effects in Metal Nanoparticle Solutions," *Nano Lett* **9**(3), 1139-1146 (2009).

148. J. G. Fujimoto et al., "Photothermal optical coherence tomography in ex vivo human breast tissues using gold nanoshells," *Optics Letters* **35**(5), 700-702 (2010).

149. M. C. Skala et al., "Photothermal Optical Coherence Tomography of Epidermal Growth Factor Receptor in Live Cells Using Immunotargeted Gold Nanospheres," *Nano Lett* **8**(10), 3461-3467 (2008).

150. Y. Jung et al., "Three-Dimensional High-Resolution Imaging of Gold Nanorods Uptake in Sentinel Lymph Nodes," *Nano Lett* **11**(7), 2938-2943 (2011).

151. B. W. Pogue, and M. S. Patterson, "Review of tissue simulating phantoms for optical spectroscopy, imaging and dosimetry," *Journal of Biomedical Optics* **11**(4), (2006).

152. B. C. Wilson, and S. L. Jacques, "Optical Reflectance and Transmittance of Tissues - Principles and Applications," *Ieee J Quantum Elect* **26**(12), 2186-2199 (1990).

153. P. Di Ninni, F. Martelli, and G. Zaccanti, "The use of India ink in tissue-simulating phantoms," *Optics Express* **18**(26), 26854-26865 (2010).

154. S. J. Madsen, M. S. Patterson, and B. C. Wilson, "The Use of India Ink as an Optical Absorber in Tissue-Simulating Phantoms," *Physics in Medicine and Biology* **37**(4), 985-993 (1992).

155. D. K. Roper, W. Ahn, and M. Hoepfner, "Microscale heat transfer transduced by surface plasmon resonant gold nanoparticles," *J Phys Chem C* **111**(9), 3636-3641 (2007).

156. B. B. Goldberg, J. B. Liu, and F. Forsberg, "Ultrasound Contrast Agents - a Review," *Ultrasound Med Biol* **20**(4), 319-333 (1994).

157. V. M. Runge et al., "Paramagnetic Agents for Contrast-Enhanced Nmr Imaging - a Review," *Am J Roentgenol* **141**(6), 1209-1215 (1983).

158. I. Brigger, C. Dubernet, and P. Couvreur, "Nanoparticles in cancer therapy and diagnosis," *Adv Drug Deliver Rev* **54**(5), 631-651 (2002).
159. X. Michalet et al., "Quantum dots for live cells, in vivo imaging, and diagnostics," *Science* **307**(5709), 538-544 (2005).
160. E. V. Zagaynova et al., "Contrasting properties of gold nanoparticles for optical coherence tomography: phantom, in vivo studies and Monte Carlo simulation," *Phys Med Biol* **53**(18), 4995-5009 (2008).
161. J. Chen et al., "Gold nanocages: Bioconjugation and their potential use as optical imaging contrast agents," *Nano Lett* **5**(3), 473-477 (2005).
162. I. Hilger, R. Hergt, and W. Kaiser, "Use of magnetic nanoparticle heating in the treatment of breast cancer," *IEE Proceedings-Nanobiotechnology* 33-39 (2005).
163. A. H. Lu, E. L. Salabas, and F. Schuth, "Magnetic nanoparticles: Synthesis, protection, functionalization, and application," *Angew Chem Int Edit* **46**(8), 1222-1244 (2007).
164. Y. D. Jin et al., "Multifunctional nanoparticles as coupled contrast agents," *Nat Commun* **1**((2010).
165. M. G. Harisinghani et al., "Noninvasive detection of clinically occult lymph-node metastases in prostate cancer," *New Engl J Med* **348**(25), 2491-U2495 (2003).
166. E. R. Wisner et al., "Indirect computed tomography lymphography using iodinated nanoparticles to detect cancerous lymph nodes in a cutaneous melanoma model," *Acad Radiol* **3**(1), 40-48 (1996).
167. M. Hamoudeh et al., "Radionuclides delivery systems for nuclear imaging and radiotherapy of cancer," *Adv Drug Deliver Rev* **60**(12), 1329-1346 (2008).
168. T. Wendler et al., "First demonstration of 3-D lymphatic mapping in breast cancer using freehand SPECT," *Eur J Nucl Med Mol I* **37**(8), 1452-1461 (2010).
169. S. Kim et al., "Near-infrared fluorescent type II quantum dots for sentinel lymph node mapping," *Nat Biotechnol* **22**(1), 93-97 (2004).
170. J. C. Alex, and D. N. Krag, "Gamma-Probe Guided Localization of Lymph-Nodes," *Surg Oncol* **2**(3), 137-143 (1993).
171. K. H. Song et al., "Near-infrared gold nanocages as a new class of tracers for photoacoustic sentinel lymph node mapping on a rat model," *Nano Lett* **9**(1), 183-188 (2008).
172. K. H. Song et al., "Noninvasive< i> in vivo</i> spectroscopic nanorod-contrast photoacoustic mapping of sentinel lymph nodes," *European journal of radiology* **70**(2), 227-231 (2009).
173. W. Luo et al., "Optical biopsy of lymph node morphology using optical coherence tomography," *Technology in cancer research & treatment* **4**(5), 539-548 (2005).
174. M. C. Skala et al., "Photothermal optical coherence tomography of epidermal growth factor receptor in live cells using immunotargeted gold nanospheres," *Nano Lett* **8**(10), 3461-3467 (2008).
175. J. Park et al., "Ultra-large-scale syntheses of monodisperse nanocrystals," *Nat Mater* **3**(12), 891-895 (2004).

176. L. M. Liz-Marzan, M. Giersig, and P. Mulvaney, "Synthesis of nanosized gold-silica core-shell particles," *Langmuir : the ACS journal of surfaces and colloids* **12**(18), 4329-4335 (1996).

177. S. J. Oldenburg et al., "Nanoengineering of optical resonances," *Chem Phys Lett* **288**(2-4), 243-247 (1998).

178. Y. Jung et al., "Three-Dimensional High-Resolution Imaging of Gold Nanorods Uptake in Sentinel Lymph Nodes," *Nano Lett* **11**(7), 2938-2943 (2011).

179. S. T. Reddy et al., "In vivo targeting of dendritic cells in lymph nodes with poly (propylene sulfide) nanoparticles," *Journal of Controlled Release* **112**(1), 26-34 (2006).

180. A. E. Hawley, L. Illum, and S. S. Davis, "Preparation of biodegradable, surface engineered PLGA nanospheres with enhanced lymphatic drainage and lymph node uptake," *Pharmaceutical research* **14**(5), 657-661 (1997).

181. C. R. Sun, B. Standish, and V. X. D. Yang, "Optical coherence elastography: current status and future applications," *J Biomed Opt* **16**(4), (2011).

182. H. Rivaz et al., "Real-Time Regularized Ultrasound Elastography," *Ieee T Med Imaging* **30**(4), 928-945 (2011).

183. B. F. Kennedy et al., "In vivo dynamic optical coherence elastography using a ring actuator," *Opt Express* **17**(24), 21762-21772 (2009).

184. R. Weller et al., *Clinical Dermatology*, Wiley (2009).

185. J. Serup, G. B. E. Jemec, and G. L. Grove, *Handbook of Non-Invasive Methods and the Skin, Second Edition*, Taylor & Francis (2006).

186. B. Alberts et al., *Essential Cell Biology, Fourth Edition*, Taylor & Francis Group (2013).

187. J. Beuthan et al., "The spatial variation of the refractive index in biological cells," *Phys Med Biol* **41**(3), 369-382 (1996).

188. F. Bevilacqua, and C. Depeursinge, "Monte Carlo study of diffuse reflectance at source–detector separations close to one transport mean free path," *JOSA A* **16**(12), 2935-2945 (1999).

189. L. Boissieux et al., "Simulation of skin aging and wrinkles with cosmetics insight," *Spring Comp Sci* 15-+ (2000).

190. W. A. G. Bruls, and J. C. Vanderleun, "Forward Scattering Properties of Human Epidermal Layers," *Photochem Photobiol* **40**(2), 231-242 (1984).

191. Brunstin.A, and P. F. Mullaney, "Light-Scattering from Coated Spheres - Model for Biological Cells," *Applied optics* **11**(3), 675-& (1972).

192. E. K. Chan et al., "Effects of compression on soft tissue optical properties," *Ieee J Sel Top Quant* **2**(4), 943-950 (1996).

193. B. Q. Chen, K. Stamnes, and J. J. Stamnes, "Validity of the diffusion approximation in bio-optical imaging," *Applied optics* **40**(34), 6356-6366 (2001).

194. J. H. Chung, "Photoaging in Asians," *Photodermatol Photo* **19**(3), 109-121 (2003).

195. E. Claridge et al., "From colour to tissue histology: Physics based interpretation of images of pigmented skin lesions," *Lect Notes Comput Sc* **2488**(730-738 (2002).

196. K. Arda et al., "Quantitative assessment of the elasticity values of liver with shear wave ultrasonographic elastography," *Indian J Med Res* **137**(911-915 (2013).

197. P. Corcuff et al., "The impact of aging on the microrelief of peri-orbital and leg skin," *J Soc Cosmet Chem* **82**(145-152 (1987).

198. R. L. Cook, and K. E. Torrance, "A reflectance model for computer graphics," *ACM Transactions on Graphics (TOG)* **1**(1), 7-24 (1982).

199. S. Diridollou et al., "In vivo model of the mechanical properties of the human skin under suction," *Skin Res Technol* **6**(4), 214-221 (2000).

200. C. Sun, B. Standish, and V. X. Yang, "Optical coherence elastography: current status and future applications," *J Biomed Opt* **16**(4), 043001 (2011).

201. T. Elgeti et al., "Cardiac MR elastography: comparison with left ventricular pressure measurement," *Journal of cardiovascular magnetic resonance : official journal of the Society for Cardiovascular Magnetic Resonance* **11**(44 (2009).

202. T. Rago et al., "Elastography: new developments in ultrasound for predicting malignancy in thyroid nodules," *The Journal of clinical endocrinology and metabolism* **92**(8), 2917-2922 (2007).

203. J. Lindop et al., "3D elastography using freehand ultrasound," *Medical Image Computing and Computer-Assisted Intervention - Miccai 2004, Pt 2, Proceedings* **3217**(1103-1104 (2004).

204. R. F. Ker, "The implications of the adaptable fatigue quality of tendons for their construction, repair and function," *Comp Biochem Phys A* **133**(4), 987-1000 (2002).

205. K. G. Vogel, "Breakout session 5: Tendon and ligament," *Clin Orthop Relat R* 367), S371-S374 (1999).

206. S. L. Y. Woo et al., "Tissue engineering of ligament and tendon healing," *Clin Orthop Relat R* 367), S312-S323 (1999).

207. W. E. Brant, "Ultrasonography of Muscles and Tendons. Examination Technique and Atlas of Normal Anatomy of the Extremities," *The Journal of Bone & Joint Surgery* **71**(7), 1118-a-1118 (1989).

208. R. M. Alexander, "Mechanics of skeleton and tendons," *Comprehensive Physiology*.

209. C. T. M. Davies et al., "Adaptation of Mechanical-Properties of Muscle to High Force Training in Man," *J Physiol-London* **365**(Aug), 277-284 (1985).

210. A. J. Banes et al., "Gap junctions regulate responses of tendon cells ex vivo to mechanical loading," *Clin Orthop Relat R* 367), S356-S370 (1999).

211. D. L. Butler, and H. A. Awad, "Perspectives on cell and collagen composites for tendon repair," *Clin Orthop Relat R* 367), S324-S332 (1999).

212. K. Yasuda, and K. Hayashi, "Changes in biomechanical properties of tendons and ligaments from joint disuse," *Osteoarthr Cartilage* **7**(1), 122-129 (1999).

213. G. T. Kuwada, "An update on repair of Achilles tendon rupture - Acute and delayed," *J Am Podiat Med Assn* **89**(6), 302-306 (1999).

214. H. Kubota et al., "Effect of motion and tension on injured flexor tendons in chickens," *J Hand Surg-Am* **21A**(3), 456-463 (1996).

215. L. J. Sandell et al., *Tissue Engineering In Musculoskeletal Clinical Practice*, American Academy of Orthopaedic Surgeons (2004).

216. D. E. Orr, and K. J. L. Burg, "Design of a modular bioreactor to incorporate both perfusion flow and hydrostatic compression for tissue engineering applications," *Ann Biomed Eng* **36**(7), 1228-1241 (2008).
217. F. Frauscher, J. Gradl, and L. Pallwein, "Prostate ultrasound--for urologists only?," *Cancer imaging : the official publication of the International Cancer Imaging Society* **5 Spec No A**(S76-82 (2005).
218. F. Aigner et al., "Comparison of real-time sonoelastography with T2-weighted endorectal magnetic resonance imaging for prostate cancer detection," *Journal of ultrasound in medicine : official journal of the American Institute of Ultrasound in Medicine* **30**(5), 643-649 (2011).
219. D. T. Ginat et al., "US elastography of breast and prostate lesions," *Radiographics : a review publication of the Radiological Society of North America, Inc* **29**(7), 2007-2016 (2009).
220. Z. Sparchez, "Real-time ultrasound prostate elastography. An increasing role in prostate cancer detection?," *Medical ultrasonography* **13**(1), 3-4 (2011).
221. P. Oehr, and K. Bouchelouche, "Imaging of prostate cancer," *Curr Opin Oncol* **19**(3), 259-264 (2007).
222. P. Kamalakanthan, "Rediology review," http://radiologyreview.tumblr.com/post/18446506375/prostate.
223. A. Banihashemi et al., "Electronic expert consultation using digital still images for evaluation of atypical small acinar proliferations of the prostate A comparison with immunohistochemistry," *Ann Diagn Pathol* **18**(3), 163-170 (2014).
224. J. Arista-Nasr et al., "Atypical small acinar proliferation: utility of additional sections and immunohistochemical analysis of prostatic needle biopsies," *Nephro-urology monthly* **4**(2), 443-447 (2012).
225. D. M. Saman et al., "A review of the current epidemiology and treatment options for prostate cancer," *Dm-Dis Mon* **60**(4), 150-154 (2014).
226. M. Kwiatkowski et al., "Comment on the US Preventive Services Task Force's draft recommendation on screening for prostate cancer," *European urology* **61**(4), 851-854 (2012).
227. F. H. Schroder, "Prostate-Cancer Mortality at 11 Years of Follow-up (vol 366, pg 981, 2012)," *New Engl J Med* **366**(22), 2137-2137 (2012).
228. P. Menon, "Interpreting your Gleason Grading Score for Prostate," http://trialx.com/curetalk/2011/07/interpret-your-gleason-grading-score/
229. W. M. Hospital, "Prostate Biopsy," http://www.weisshospital.com/medical-services/clinical-programs/robotic-prostate-surgery/prostate-biopsy.aspx
230. V. O. Company, "EVALUATING YOUR CANCER."
231. S. Ahmad et al., "Transrectal quantitative shear wave elastography in the detection and characterisation of prostate cancer," *Surg Endosc* **27**(9), 3280-3287 (2013).
232. R. G. Barr, R. Memo, and C. R. Schaub, "Shear Wave Ultrasound Elastography of the Prostate Initial Results," *Ultrasound Q* **28**(1), 13-20 (2012).
233. B. F. Kennedy et al., "In vivo three-dimensional optical coherence elastography," *Opt Express* **19**(7), 6623-6634 (2011).

234. D. F. Gleason, and Mellinge.Gt, "Prediction of Prognosis for Prostatic Adenocarcinoma by Combined Histological Grading and Clinical Staging," *J Urology* **111**(1), 58-64 (1974).
235. K. M. Kennedy et al., "Needle optical coherence elastography for tissue boundary detection," *Opt Lett* **37**(12), 2310-2312 (2012).